Title
Exotic Dark Matter Candidates Generated from Scalar Field Condensation in the Early Universe

Author
Cotner, Eric Welch

Publication Date
2018

Peer reviewed|Thesis/dissertation

UNIVERSITY OF CALIFORNIA
Los Angeles

Exotic Dark Matter Candidates Generated from Scalar Field Condensation in the Early Universe

A dissertation submitted in partial satisfaction
of the requirements for the degree
Doctor of Philosophy in Physics

by

Eric Welch Cotner

2018

ABSTRACT OF THE DISSERTATION

Exotic Dark Matter Candidates Generated from
Scalar Field Condensation in the Early Universe

by

Eric Welch Cotner
Doctor of Philosophy in Physics
University of California, Los Angeles, 2018
Professor Alexander Kusenko, Chair

Scalar fields, though simple conceptually and mathematically, can be responsible for a wide array of emergent phenomena, such as spontaneous symmetry breaking, superconductivity, and the production of solitons. These fields may be responsible for the creation of, or even the identity of, dark matter. This manuscript details the production of dark matter from scalar fields in the form of Q-balls, boson stars, and primordial black holes, and explores the consequences of the existence of such objects and their interactions.

The dissertation of Eric Welch Cotner is approved.

E T Tomboulis

Roberto Peccei

Graciela B Gelmini

Alexander Kusenko, Committee Chair

University of California, Los Angeles

2018

To my mother, who I hope would have been very proud.

To my father, who somehow managed to bring me up right.

To my cats, for their unwavering support and insightful discussions.

TABLE OF CONTENTS

LIST OF FIGURES

LIST OF TABLES

VITA

2010-2011 Engineering intern with Kyocera America's Research and Development division. Developed etching procedures for SEM microscopy of solder grain boundaries.

2011-2013 Engineering intern with General Atomcs' Inertial Fusion Technology division. Developed fuel injection method for NIF indirect-drive fusion utilizing inductive acceleration and steering of laser targets.

2013 B.S. in Physics, with a minor in Mathematics, UCSD.

2013-2018 Teaching Assistant, Physics and Astronomy Department, UCLA. Taught a variety of discussion and lab sections. Subjects included classical mechanics, electrodynamics, quantum mechanics, hydrodynamics, special relativity, particle physics, cosmology.

2014 M.S. in Physics, UCLA.

2014-2018 Research Assistant, Physics and Astronomy Department, UCLA. Studied dark matter, particle astrophysics and cosmology under the supervision of thesis advisor Alexander Kusenko.

PUBLICATIONS

Primordial Black Holes from Inflaton Fragmentation into Oscillons, E. Cotner, A. Kusenko and V. Takhistov, arXiv:1801.03321 (2018)

Primordial black holes from scalar field evolution in the early universe, E. Cotner and A. Kusenko, Phys. Rev. D **96**, no. 10, 103002 (2017)

Primordial black holes from supersymmetry in the early universe, Phys. Rev. Lett. **119**, no. 3, 031103 (2017)

Astrophysical constraints on dark-matter Q-balls in the presence of baryon-violating operators, E. Cotner and A. Kusenko, Phys. Rev. D **94**, no. 12, 123006 (2016)

Collisional interactions between self-interacting nonrelativistic boson stars: Effective potential analysis and numerical simulations, E. Cotner, Phys. Rev. D **94**, no. 6, 063503 (2016)

CHAPTER 1

Background

1.1 History

One of the most intriguing scientific questions of our time is the identity of "dark matter", a mysterious substance that pervades the universe. We cannot see it, yet we know that it is there. First hypothesized by Fritz Zwicky [1] and subsequently confirmed by the work of Vera Rubin and Kent Ford [2], our understanding of dark matter has developed rapidly in recent decades. This introductory section is not meant to provide a complete historical review, but just a glimpse to motivate the interested reader; a more complete review can be found elsewhere [3, 4].

The existence of dark matter is unambiguous. The evidence in favor includes the observed flatness of galactic rotation curves [5, 6, 7, 8], the temperature power spectrum of the Cosmic Microwave Background (CMB) [9, 10, 11], baryon acoustic oscillations (BAO) [12, 13], and gravitational lensing of galaxy clusters [14, 15, 16]. However, though its existence has been verified experimentally beyond a doubt, its identity remains unclear. Evidence suggests that it is not baryonic in nature, and that it must therefore be some exotic or unknown form of matter. Unfortunately (or perhaps fortunately if you're a theorist), the fact that we have only observed the effect of its gravitational interactions allows for a dazzling array of candidates (see Figure 1.1 courtesy of Tim Tait [17]), including simple TeV-scale particles such as weakly interacting massive particles (WIMP) [18, 19, 20], superheavy WIMPzillas [21], supersymmetry(SUSY)-motivated candidates such as the neutralino and gravitino [22, 23], light scalar particles such as axions [24, 25, 26, 19] and galactic-scale ψ-DM or fuzzy DM [27, 28], scalar solitons such as Q-balls [29, 30, 31], boson stars [32, 33, 34], and axion

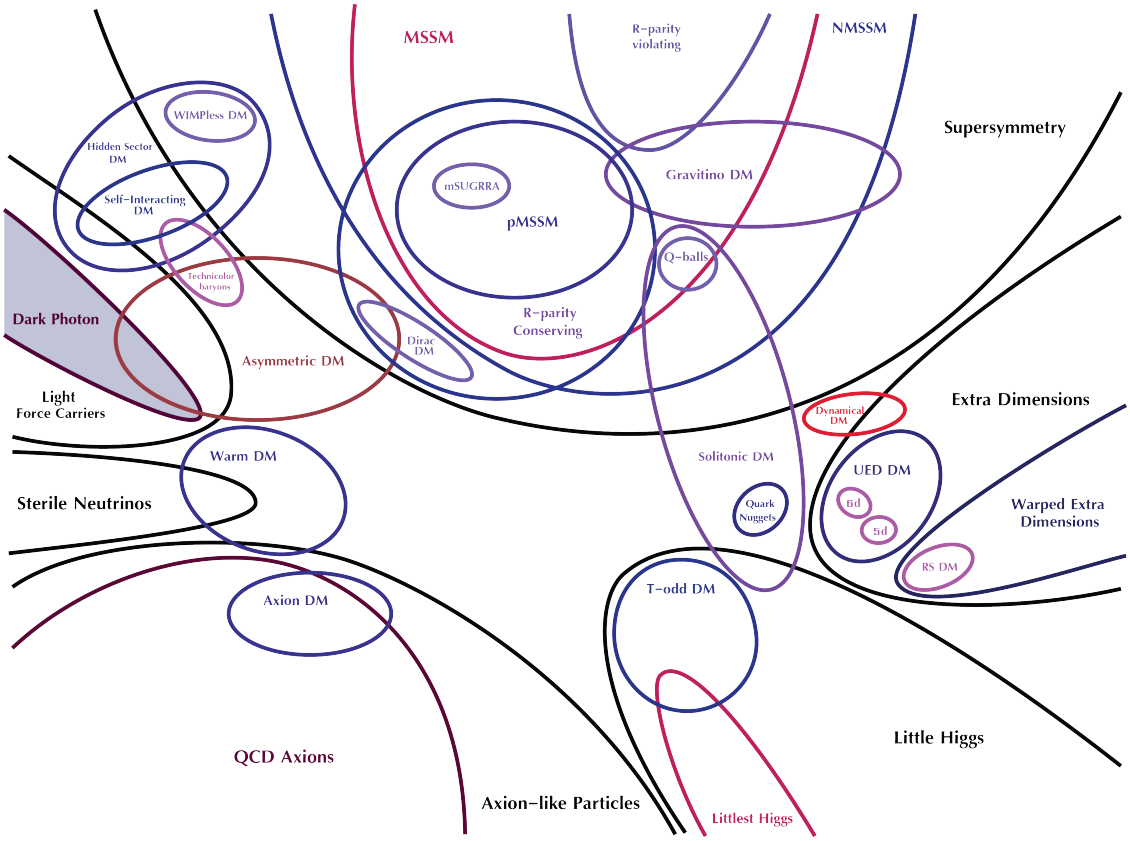

Figure 1.1: Schematic diagram of the theory space of dark matter. Image courtesy of Tim Tait [17].

miniclusters [35, 36, 37], primordial black holes (PBH) [38, 39, 40, 41], Planck-mass black hole remnants [42, 43], sterile neutrinos [44, 45], dark photons [46], dark mesons [47], dark glueballs [48, 49, 50], asymmetric DM [51, 52], etc.

With this plethora of possible dark matter candidates, it is imperative that we explore all possibilities, including the more exotic candidates. Among the more interesting candidates are those which are composed of or generated by scalar field dynamics in the early universe. Scalar fields are perhaps the simplest form of matter, but this simplicity can be deceiving. They are known to be responsible for a wide range of complex phenomena, such as electroweak symmetry breaking (displacement of the Higgs field) [53, 54, 55, 56, 57, 58] and superconductivity (Bose-Einstein condensation of Cooper pairs) [59, 60, 61], and could potentially be responsible for other phenomena as well, such as baryogenesis [62, 63], GUT symmetry breaking, inflation, strong CP invariance, dark energy, and dark matter.

This thesis will focus on three specific dark matter candidates either made of or produced by scalar fields: Q-balls, boson stars, and primordial black holes. The following sections will provide an exposition on each, including the history of previous work, general properties and formation mechanisms. In the following chapters, I will detail my specific work on these subjects, including several published works in their entirety.

1.2 Exotic Dark Matter Candidates

1.2.1 Q-balls

Q-balls were originally formulated and named by by Sidney Coleman [64]. The "Q" signifies the presence of a conserved global charge, which leads to its stability. We can construct such a state through a variational method. Given a complex scalar field ϕ,

$$S = \int d^4x \, \mathcal{L} = \int d^4x \, \left[\partial_\mu \phi^* \partial^\mu \phi - V(\phi)\right] \tag{1.1}$$

we assume that the potential is invariant under the $U(1)$ transformation $\phi \to e^{i\alpha}\phi$, such that this results in a conserved current

$$J_\mu = i\left((\partial_\mu \phi^*)\phi - \phi^*(\partial_\mu \phi)\right). \tag{1.2}$$

Making the appropriate Legendre transformation $\mathcal{H} = \dot{\phi}\pi + \dot{\phi}^*\pi^* - \mathcal{L}$, with $\pi = \partial\mathcal{L}/\partial\dot{\phi} = \dot{\phi}^*$, the Hamiltonian density of the theory is

$$\mathcal{H} = |\dot{\phi}|^2 + |\nabla\phi|^2 + V(\phi) \tag{1.3}$$

We can create a modified energy functional by integrating over $\mathcal{H}$, while explicitly enforcing the charge conservation with a Lagrange multiplier ω:

$$\tilde{E} = \int d^3x \left[|\dot{\phi}|^2 + |\nabla\phi|^2 + V(\phi)\right] + \omega\left[Q - i\int d^3x \left(\dot{\phi}^*\phi - \phi^*\dot{\phi}\right)\right] \tag{1.4}$$

$$= \int d^3 \left[|\dot{\phi} + i\omega\phi|^2 + |\nabla\phi|^2 + \left(V(\phi) - \omega^2|\phi|^2\right)\right] + \omega Q \tag{1.5}$$

When $\tilde{E}$ is minimized, this gives the equations of motion of the Q-ball. Immediately, we see that in order for this to be a minimum, $\dot{\phi} + i\omega\phi = 0$, the solution to which is $\phi(\boldsymbol{x}, t) = \phi(\boldsymbol{x})e^{-i\omega t}$. The equation of motion for the spatial distribution of ϕ can be derived via $\delta\tilde{E}/\delta\phi = 0$:

$$\nabla^2\phi - \left(\frac{\partial V}{\partial\phi^*} - \omega^2\phi\right) = 0 \tag{1.6}$$

We can see that this equation describes a stationary state in an effective potential of $\tilde{V}(\phi) = V(\phi) - \omega^2|\phi|^2$. Expanding $\tilde{V}$ to lowest order we have $\tilde{V} \approx (m^2 - \omega^2)|\phi|^2 + \cdots$. We now see that if $\omega > m$, there are no stable solutions. The stability condition is therefore that there exists some region of the scalar potential φ such that $V(\varphi) < m^2|\varphi|^2$. Conceptually, this can be understood as requiring that the potential has attractive nonlinear interactions.

We can get a variational estimate for the mass, radius and central field value of a Q-ball with fixed charge Q by assuming a variational ansatz $\phi(r) = \phi_0 \exp(-\frac{1}{2}(r/R)^2)$. Normalization fixes $\phi_0 = \sqrt{Q/2\pi^{3/2}\omega R^3}$ (we take $Q > 0$ without loss of generality from now on). For a scalar potential with a "flat direction", common in supersymmetry, we can approximate $V(\phi) \approx \Lambda^4$ inside the soliton and zero outside. Then, minimizing the energy functional $\tilde{E}[\phi]$ with respect to R and ω gives us

$$R = 0.56Q^{1/4}/\Lambda, \quad \omega = 2.2\Lambda Q^{-1/4}, \quad E = \omega Q = 2.2\Lambda Q^{3/4}, \quad \phi_0 = 0.5\Lambda Q^{1/4} \tag{1.7}$$

We can see that for large Q, the energy/mass of the soliton grows as $Q^{3/4}$, whereas a collection of free particles with the same charge would grow linearly in Q. Therefore, the solitonic

configuration is more energetically favorable for large values of Q, as expected. In order to satisfy the condition $\omega < m$, the Q-ball has a minimum charge of $Q_{\min} = 23(\Lambda/m)^4$.

There are even more exotic types of Q-balls than the globally-conserved type discussed above, such as those with a local gauge invariance [65, 66], as well as nonzero angular momentum [67, 68], but discussion of these types of Q-balls is beyond the scope of this work.

1.2.2 Boson Stars

Similar to Q-balls, boson stars (or Bose stars) are bound configurations of scalar condensates, but with their dynamics dominated by gravitational forces (first considered by Ruffini and Bonazzola [69] and then further by many others [70, 71]). Because gravity is such a weak long-range attractive force (as opposed to the surface-tension-like interaction holding together Q-balls), boson stars can be extremely diffuse, spanning entire galaxies or galactic clusters. On the other hand, as a boson star's mass increases, so does the gravitational binding, causing it to become more compact. Eventually, the density may exceed that of a neutron star, or even become comparable to a black hole [72].

Unlike Q-balls, boson stars may be composed of both complex and real scalar fields. If the field is real, it is called an *oscillaton* (in analogy with oscillons) [73, 74, 75, 76]. If the field is complex and has no self-interactions in the scalar potential, then is is called a *mini boson star*, which are generally extremely compact since there is no nonlinear repulsion to prevent the star from contracting.

Recently, boson stars have received much attention as potential dark matter candidates, where the scalar field from which they are composed is the hypothesized axion [77, 36, 35, 78]. These *axion stars* or *axion miniclusters* would form in the early universe due to gravitational instability, and could be responsible for the mysterious fast radio bursts due the axion's $\phi F \tilde{F}$ interaction [79, 80, 81].

1.2.3 Primordial Black Holes

Primordial black holes (PBH) go back to Hawking and Carr [82, 83]. If a region of space in the early universe could develop a modest overdensity $\delta = (\rho - \bar{\rho})/\bar{\rho}$ with respect to the background energy density, then gravitational instabilities could drive these regions to collapse and form black holes. The possible spectrum of primordial black hole masses is very broad, constrained by Hawking radiation from below ($\sim 10^{15}$ g), and the mass of the Hubble horizon in the early stages of the universe from above ($\sim 10^5$ $M_\odot$). They could be responsible for a variety of different unexplained phenomena, such as positron excess [84], gamma ray bursts [85, 84], baryogenesis [86], heavy nuclei [87], and many others.

However, there exist numerous constraints (from a variety of sources) on the abundance and mass of primordial black holes. If PBH were to make up 100% of the dark matter, these constraints restrict their masses to a relatively narrow window around 10^{20} grams. There has been much discussion of this recently, as the validity of the existing constraints in this regime has been called into question [88, 89, 90].

In the standard lore, the primary mechanism for producing PBH is due to density fluctuations seeded during inflation. If the inflaton potential has a relatively flat region and the field trajectory passes over this area, large fluctuations will be generated. These fluctuations will then be blown up to superhorizon sizes during inflation. Once the inflationary period has passed, however, these fluctuations may pass back within the horizon during a later epoch, at which point they will collapse and form PBH. This method makes some strong assumptions as to the shape of the inflaton potential, and requires relatively fine tuning of the potential's parameters. In Chapters 4 and 5, an alternate mechanism is detailed which does not make such strong assumptions regarding the shape of the inflaton potential.

CHAPTER 2

Boson Star Collisions

The content of this chapter has been published in Physical Review D as *Collisional interactions between self-interacting nonrelativistic boson stars: Effective potential analysis and numerical simulations*, E. Cotner, Phys. Rev. D **94**, no. 6, 063503 (2016) [91].

Scalar particles are a common prediction of many beyond the Standard Model theories. If they are light and cold enough, there is a possibility they may form Bose-Einstein condensates, which will then become gravitationally bound. These boson stars are solitonic solutions to the Einstein-Klein-Gordon equations, but may be approximated in the non-relativistic regime with a coupled Schrödinger-Poisson system. General properties of single soliton states are derived, including the possibility of quartic self-interactions. Binary collisions between two solitons are then studied, and the effects of different mass ratios, relative phases, self-couplings, and separation distances are characterized, leading to an easy conceptual understanding of how these parameters affect the collision outcome in terms of conservation of energy. Applications to dark matter are discussed.

2.1 Introduction

One of the outstanding problems facing modern astrophysics and particle physics is the composition of the dark matter which makes up a large fraction of the energy density of the Universe. In the quest to identify the characteristics which define this type of matter, many authors have considered numerous models. One of the main candidates in this quest is the WIMP, a class of particle with GeV- or TeV-scale mass which (as the name suggests), interacts weakly with itself and/or normal baryonic matter. Though WIMP models in the

ΛCDM paradigm can reproduce the observed large-scale structure of the Universe, there is some tension between ΛCDM simulations and observation on galaxy-sized scales. Specifically, there are issues concerning how sharply peaked the density profiles of DM-dominated galaxies are [92], and the abundance and luminosity of satellite galaxies [93]. Simulations predict singular behavior near the center of a typical galaxy, while observations of dwarf spheroidal galaxies prefer a smoother, core-like profile. Propositions to explain this discrepancy have invoked processes such as baryonic feedback [94], in which supernovae or other baryonic astrophysical phenomena near the galactic nucleus push dark matter outward, and self-interacting dark matter (SIDM) [95], in which infalling particles can transfer momentum to those in the core, smoothing the density profile. However, baryonic interaction with dark matter and the SIDM cross-section are highly constrained by measurements from the Bullet Cluster [96], direct-detection experiments [97], and black hole growth [98].

Indeed, a DM candidate exists which can naturally explain the cusp-core problem while simultaneously reproducing the same cosmological-scale structure of the Universe in the same fashion as ΛCDM [28], and may even be able to resolve the mysteries surrounding the collisions of the Bullet Cluster and Abell 520 [99]. A boson star, or soliton composed of a self-gravitating Bose-Einstein condensate, has a series of interesting properties which make it a good candidate to resolve some of the outstanding issues inherent with ΛCDM on small scales. The component particles making up a boson star can, to good approximation, share a macroscopic wave function due to their Bose-Einstein statistics. Just as a localized particle's wave function naturally spreads with time, a boson star will expand until the attractive force of gravity balances the outward "quantum pressure", leading to a stable solitonic state. The shape of the resulting density profile is devoid of a singularity, and is smooth and continuous at the origin. In addition, collisions between two boson stars may cause the two to either stick together, scatter inelastically, or pass right through each other (depending on a number of factors), leading to momentum transfer, agglomeration/fracturing of compact objects, or spreading of the central density cusps predicted in ΛCDM simulations. This effect exists regardless of whether or not the scalar field has significant self-interactions in its potential. There are many theoretically-motivated candidates to make up the scalar field in question.

The axion, for example, is expected to be an extremely light ($m \lesssim 1\,\mu$eV) scalar, and readily forms a condensate at relatively high temperatures [100]. The existence of the Peccei-Quinn axion solves the strong CP problem, and axion-like fields are a general prediction of string theories [101]. Scalar superpartners of the fermionic fields of the Standard Model, though expected to be relatively heavy, may be good candidates, and have been studied extensively under the name SUSY Q-balls [102][103] (where the Q refers to a conserved Noether charge) in the absence of gravitational interaction. Couplings to the Standard Model Higgs or some other scalar with a Higgs mechanism, if they exist, might also provide a means for creating stable Q-balls from condensed scalar fields. In addition, microlensing experiments from the MACHO [104], EROS [105] and OGLE [106] collaborations have detected a significant excess of events over those expected simply from stellar populations, and puts the expected mass of these objects between $0.15 - 0.9\,M_{\odot}$ at a 95% confidence interval. Could the detected compact objects be made up of boson stars?

In this paper, I will outline the existence and classification of stable, non-relativistic boson stars, and will derive approximate analytical profiles and properties of these stars in section 2.2. I then focus on the binary interactions between two such stars, and the different head-on scattering outcomes based on initial velocity, distance, relative phase and mass, and the degree of self-coupling in section 2.3. These findings are then verified through numerical scattering simulations in section 2.4. Finally I end with a discussion of the possible application of these results to dark matter phenomenology and future research in section 2.5.

2.2 Existence and stability of boson stars in the non-relativistic limit

We begin with the action for a scalar field minimally coupled with gravity:

$$S = \int d^4x \sqrt{-g} \left[\frac{1}{2\kappa} R + \nabla_\mu \varphi^\dagger \nabla^\mu \varphi - V(\varphi) \right] \tag{2.1}$$

In the non-relativistic approximation, we can write φ in terms of a complex wave function:

$$\begin{cases} \varphi = \frac{1}{\sqrt{2m}} \left(e^{-imt}\psi + e^{imt}\psi^*\right) & \varphi^* = \varphi \\ \varphi = \frac{1}{\sqrt{2m}} e^{-imt}\psi & \varphi^* \neq \varphi \end{cases} \tag{2.2}$$

We may neglect terms containing an exponential factor since they will average out to zero due to rapid oscillation of the mass frequency, and use the weak-field gravity ansatz $g^{00} = 1+2\phi$, $g^{ij} = -(1+2\phi)$, $g^{i0} = g^{0j} = 0$. Variation of the action then leads to the Schrödinger-Poisson system for a self-interacting scalar field:

$$i\dot{\psi} = -\frac{1}{2m}\nabla^2\psi + \frac{\lambda}{8m^2}|\psi|^2\psi + m\phi\psi \tag{2.3}$$

$$\nabla^2\phi = 4\pi G m|\psi|^2 \tag{2.4}$$

where ψ is the bosonic wave function, ϕ is the gravitational potential, and λ is the coupling constant due to a quartic self-interaction: $V(\varphi) = \frac{\lambda}{4}|\varphi|^4$. Higher-order effective self-couplings may exist in principle, but we shall neglect them here. Higher-order self-couplings can lead to the formation of solitonic states even in the absence of gravity (a good review of this may be found in Lee and Pang [107]), but a quartic interaction by itself is not enough. These types of field configurations are referred to as mini-boson stars.

In the Hartree-Fock approximation, we may assume that the entire collection of particles share a single wave function, as they have formed a Bose-Einstein condensate. The critical temperature for a non-relativistic condensate is given by [108]:

$$\begin{aligned} kT_c &= \frac{2\pi}{m}\left(\frac{n}{\zeta(3/2)}\right)^{2/3} \\ &= 1.59 \text{ MeV} \left(\frac{m}{10^{-9} \text{ eV}}\right)^{-5/3} \left(\frac{\Omega}{.25}\right)^{2/3} \end{aligned} \tag{2.5}$$

where we have substituted values for a typical uniformly-distributed axion-mass dark matter particle under the assumption it makes up 100% of the DM. The temperature of such a particle today is surely below this limit, and in regions of higher density (such as in galaxies

and solitons), this critical temperature will be even higher.

We may find approximate stable ground states through the use of the variational method. First, using the Green's solution for the gravitational potential ϕ, we may calculate the expectation value of the Hamiltonian in an arbitrary state $|\psi\rangle$ in the following manner [100]:

$$\langle H\rangle = \frac{1}{2m}\int d^3x\,|\nabla\psi|^2 + \frac{\lambda}{16m^2}\int d^3x\,|\psi|^4 - \frac{Gm^2}{2}\int d^3x\int d^3x'\,\frac{|\psi(\vec{x})|^2|\psi(\vec{x}')|^2}{|\vec{x}-\vec{x}'|} \tag{2.6}$$

A good first guess for a solitonic ground state may be a Gaussian profile:

$$\psi(\vec{x}) = \left(\frac{2N^{2/3}k^2}{\pi}\right)^{3/4} e^{-k^2r^2} \tag{2.7}$$

where k is an inverse length-scale variational parameter or wave vector, and $|\psi\rangle$ is properly normalized such that $\langle\psi|\psi\rangle = N$. Substitution of this state into the expectation value for the Hamiltonian leads to the equation $\langle H\rangle = \frac{3N}{2m}k^2 + \frac{\lambda N^2}{16\pi^{3/2}m^2}k^3 - \frac{Gm^2N^2}{\pi^{1/2}}k$, and variation with respect to $1/k$ returns

$$1/k = \frac{3\pi^{1/2}}{2}\frac{1}{Gm^3N}\left(1+\sqrt{1+\frac{1}{12\pi^2}\lambda Gm^2N^2}\right) \tag{2.8}$$

This is the same result derived by Chavanis [109], and the single-soliton analysis that follows is nearly identical. He also uses a similar "effective potential" formalism for the radius of the boson star, though he does not extend it to interactions of solitons as is done in this paper. Since dark matter is expected to be weakly self-interacting, it is useful to look at the weak interaction limit where $\xi \equiv \lambda Gm^2N^2/12\pi^2 \ll 1$ (more precisely, $|\xi| \ll 1$, since there is no restriction on the sign of λ if we invoke higher-order couplings to prevent the Hamiltonian from being unbounded from below).

$$1/k \approx 3\pi^{1/2}\frac{1}{Gm^3N}\left(1+\frac{1}{48\pi^2}\lambda Gm^2N^2\right) \tag{2.9}$$

In the case of no interactions whatsoever, we have

$$1/k \approx \frac{3\pi^{1/2}}{Gm^3N} \approx \frac{3\pi^{1/2}}{Gm^2M} \\ = 0.88 \left(\frac{m}{10^{-9}\text{ eV}}\right)^{-2} \left(\frac{M}{1\text{ M}_\odot}\right)^{-1} \text{km} \tag{2.10}$$

Since the radius scales as M^{-1}, this means that more massive condensates are more tightly gravitationally bound and have a smaller spatial scale. For the parameters given above, this condensate is incredibly tiny given its mass; so tiny that it's actually within its Schwarzschild radius, meaning it would have collapsed to a black hole at this mass (see maximum mass in eqn. 2.12). However, even a tiny repulsive self-coupling λ can get around this. It is important to note that the $|\xi| \ll 1$ limit does not necessarily imply $|\lambda| \ll 1$; the particle number of the condensate must also be small enough to satisfy this inequality. Likewise, $\xi \gg 1$ does not imply $\lambda \gg 1$. This means the self-interaction parameter may be very large for large particle number, even if the self-coupling λ itself is quite modest. When $\xi \gg 1$, the soliton becomes more diffuse and a Gaussian wave function is no longer a good approximation to its shape. However, the length scale parameter should be within a factor of order unity of the real thing, so we can still glean some information from the Gaussian variational wave function in this regime. In this limit, the length scale parameter is

$$1/k \approx \frac{3\pi^{1/2}}{2}\frac{1}{Gm^3N}\left(\xi^{1/2} + 1 + 2\xi^{-1/2}\right) \\ \approx 2.4 \times 10^{17} \left(\frac{m}{10^{-9}\text{eV}}\right)^{-2} \left(\frac{\lambda}{10^{-6}}\right)^{1/2} \text{kpc} \tag{2.11}$$

where the final expression is in the limit $N \to \infty$. For this set of parameters (corresponding to $\xi \sim 10^{23}$), the condensate is *enormous*, stretching beyond the observable universe! Of course this is an extreme example, but I just wanted to show the enormous effect even a tiny coupling can have. We can see that the leading order term in this approximation is independent of the particle number, suggesting that in the limit $N \to \infty$, the spatial extent of such a soliton will approach a finite size. This may have interesting consequences for black hole formation, since even a tiny self-coupling may prevent black hole collapse. We

may approximate the critical mass and rough lower bound at which general relativistic effects take hold and black hole collapse may occur by comparing the Schwarzschild radius to the soliton radius $R_s = 2GM \sim 1/k$ which implies:

$$M_{\max} \sim \sqrt{\frac{3\pi^{1/2}}{2G^2m^2}} \approx 10^{-1} \left(\frac{m}{10^{-9}\text{ eV}}\right)^{-1} M_\odot \tag{2.12}$$

in the $|\xi| \ll 1$ regime, and

$$\begin{aligned} M_{\max} &\sim \frac{1}{8m^2}\sqrt{\frac{3\lambda}{\pi G^3}} \\ &\approx 10^{32} \left(\frac{\lambda}{10^{-6}}\right)^{1/2} \left(\frac{m}{10^{-9}\text{ eV}}\right)^{-2} M_\odot \end{aligned} \tag{2.13}$$

in the $\xi \gg 1$ regime. This agrees with the Kaup limit [110][69] in the non-interacting case, and with the analysis of Colpi, Shapiro and Wasserman [111] in the strongly-interacting case. As is evident from this comparison, solitons without self-interaction could potentially readily form many small black holes (especially at higher particle mass), whereas those with self-interaction are stable against gravitational collapse for all practical purposes, unless the self-coupling is extremely small. The binding energy is given by

$$E_0 = -\frac{8G^2m^5N^3\left(3 + 2\xi + 3\sqrt{1+\xi}\right)}{36\pi(1+\sqrt{1+\xi})^3} \tag{2.14}$$

Which in the two extreme limits are

$$E_0 \approx \begin{cases} -\frac{G^2m^5N^3}{6\pi} + \frac{\lambda G^3m^7N^5}{432\pi^3} + O(\lambda^2) & |\xi| \ll 1 \\ -\frac{8G^{3/2}m^4N^2}{3\sqrt{3\lambda}} + \frac{8\pi Gm^3N}{\lambda} + O(\lambda^{-3/2}) & \xi \gg 1 \end{cases} \tag{2.15}$$

which are in good agreement with several numerical analyses [69][112][70]. The total mass of the star in this state is given by $M = mN + E_0$, which since the binding energy is negative due to the gravitational interaction, is energetically favorable to the state in which the component particles making up the condensate are unbound, ensuring stability against dissolution of the soliton. The soliton is also classically stable against radiation of single

particles since $E_0(N-1) - E_0(N) > 0$, meaning that the bound state with $N-1$ particles has a higher energy than the bound state with N particles. Unfortunately, it becomes clear that the non-relativistic approximation breaks down very quickly once the binding energy per particle approaches its rest mass, and therefore is only valid in the regime

$$1 \gg \frac{|E_0|}{mN} \approx \begin{cases} \frac{G^2 m^4 N^2}{6\pi} & \xi \ll 1 \\ \frac{8G^{3/2} m^3 N}{3\sqrt{3\lambda}} & \xi \gg 1 \end{cases} \tag{2.16}$$

This analysis therefore only holds for galaxy-mass solitons when the particle mass is very light, $m \lesssim 10^{-21}$ eV when there is no self-interaction [?], and 30 eV when $\lambda = 10^{-6}$. This upper limit might be relaxed if the dark matter content of the galaxy is instead composed of many smaller solitons. If we assume boson star masses comparable to a solar mass, the particle mass can be much larger before the non-relativistic analysis breaks down, as high as $m \lesssim 10^{-9}\,\text{eV}$ for $\lambda = 0$ and 30 MeV if $\lambda = 10^{-6}$. It bears repeating that these upper limits are by no means actual physical limits, just the limits of applicability of this analysis, and a fully relativistic model must be used for masses beyond this.

As should be obvious, the binding energy becomes complex when $\lambda < -12\pi^2/2Gm^2N^2$. From the form of the Schrödinger equation, we can see that the self-interaction term contributes energy positively when the density rises; therefore it represents a short-range self-repulsion when λ is positive. When it is negative, this is now a short range attraction. The parameter range where the energy becomes complex thereby signifies an instability where the combined attractive force of gravity and self-interaction causes the soliton to either collapse, or split into multiple smaller solitons until the binding energy of each is no longer complex. This critical mass occurs at

$$M_{\max} \approx \frac{3\pi}{\sqrt{2G|\lambda|}} = 6.7 \times 10^3 \left(\frac{|\lambda|}{10^{-6}}\right)^{-1/2} \mathrm{M}_P \tag{2.17}$$

which is in general agreement with the work of Eby, Kouvaris, Nielsen, and Wijewardhana [32]. It is unclear from this variational analysis which of these situations would occur, but the results of numerical simulations suggest a combination of both.

2.3 Binary interactions

Once the stable states have been found, the next question is how do two or more of these solitons interact with each other. Do they stick, recoil, or pass right through each other during a collision? If we compute the energy of a certain binary configuration, we can use this to answer that question by comparing the energies of different configurations, using this energy as an effective potential for the separation distance. A common method used in undergraduate quantum classes to find the binding energy of the H_2^+ molecule will be applicable here. Once again, we use the variational method to find the expectation value of the Hamiltonian, only this time our variational states will be a superposition of two solitons, separated in space, and potentially differing in their relative phase. The separation d will be the variational parameter, and we shall hold the soliton wave numbers k_i constant. In this work, for computational ease, I will suppose that there is no relative motion, so that the two solitons are suspended in their separation. Our superposition state, $|\psi\rangle$, is normalized such that $\langle\psi|\psi\rangle = N = N_1 + N_2$, so that the total particle number is conserved throughout. This state has the form

$$|\Psi(\vec{r})\rangle = A\left[|\psi(\vec{r} - \vec{d}/2)\rangle + e^{i\alpha}\,|\psi(\vec{r} + \vec{d}/2)\rangle\right] \tag{2.18}$$

where $|\psi_i(\vec{r})\rangle$ are the 1-soliton wave functions solved for in the previous section, α is the relative phase between the two solitons and A is the overall normalization, which is given by

$$A = \sqrt{\frac{N}{N + 2\cos\alpha\,\langle\psi_1|\psi_2\rangle}}, \tag{2.19}$$

$$\langle\psi_1|\psi_2\rangle = 2\sqrt{2N_1N_2}\left(\frac{k_1k_2}{k_1^2 + k_2^2}\right)^{3/2}\exp\left(-\frac{(dk_1k_2)^2}{k_1^2 + k_2^2}\right) \tag{2.20}$$

Substituting this state into the expectation value of the Hamiltonian, we arrive at a very complicated expression which is better tackled in pieces. There are three terms: the kinetic,

self-interaction, and gravitational. The contribution to the kinetic term is of the form

$$E_{\rm kin} = \frac{\pi^{3/2}A^2}{8mk_1k_2}\left[3\sqrt{2}(A_2^2k_1 + A_1^2k_2)\right.$$
$$\left. -\frac{16A_1A_2k_1^3k_2^3}{(k_1^2+k_2^2)^{7/2}}\left(2(dk_1k_2)^2 - 3(k_1^2+k_2^2)\right)\exp\left(-\frac{(dk_1k_2)^2}{k_1^2+k_2^2}\right)\cos\alpha\right] \quad (2.21)$$

where A_1 and A_2 are simply the normalization factors of the single-soliton wave function (e.g. $A_1 = (2N_1^{2/3}k_1^2/\pi)^{3/4}$). We may observe that there is a length scale $\ell = \sqrt{k_1^2+k_2^2}/k_1k_2$ which determines a critical separation distance between the two solitons. If we recognize that $R_i \equiv 1/k_i$ is roughly the characteristic radius of the soliton, then we can also understand that $\ell = \sqrt{R_1^2+R_2^2}$ is the geometric mean of the two radii. Rescaling d so that it is in units of ℓ ($x \equiv d/\ell$), we can rewrite the energy as

$$E_{\rm kin} = \frac{A^2}{2\sqrt{2}m}\left[3\sqrt{2}(N_1k_1^2 + N_2k_2^2) - \frac{32\sqrt{N_1N_2}}{(k_1k_2)^{3/2}\ell^5}(x^2-3/2)e^{-x^2}\cos\alpha\right] \quad (2.22)$$

After substituting in the variational estimate for the k_i found for the stationary solitons, we find that the kinetic energy is of the form $E_{\rm kin} = G^2m^5f(N_1, N_2, \alpha, x)$. Thus, the mass of the constituent particles only serves to scale the energy and length factors, and cannot change the features of these curves for fixed particle number.

The phase-dependent bump or well found in the region $x \ll 1$ in the $N_1 \sim N_2$ case is reminiscent of either the nuclear potential found in nuclear scattering and fusion, or the binding energy curve found in atomic physics. When the solitons overlap considerably, this suggests that the two either repel or merge depending on phase. However, the superposition of states we have used to calculate this energy is not likely to hold when $x \ll 1$. This is due to the fact that the nonlinearity introduced by the gravitational interaction violates the superposition principle, so that the superposition of solitons we have started with is technically not allowed. Far from each other, this violation is negligible and assuming superposition is a good approximation. But in the $x \ll 1$ regime, superposition is no longer valid and our trial wave function for individual solitons suffers in accuracy. The solitons should merge, but this description does not account for that. Therefore, treat the results of this analysis in this

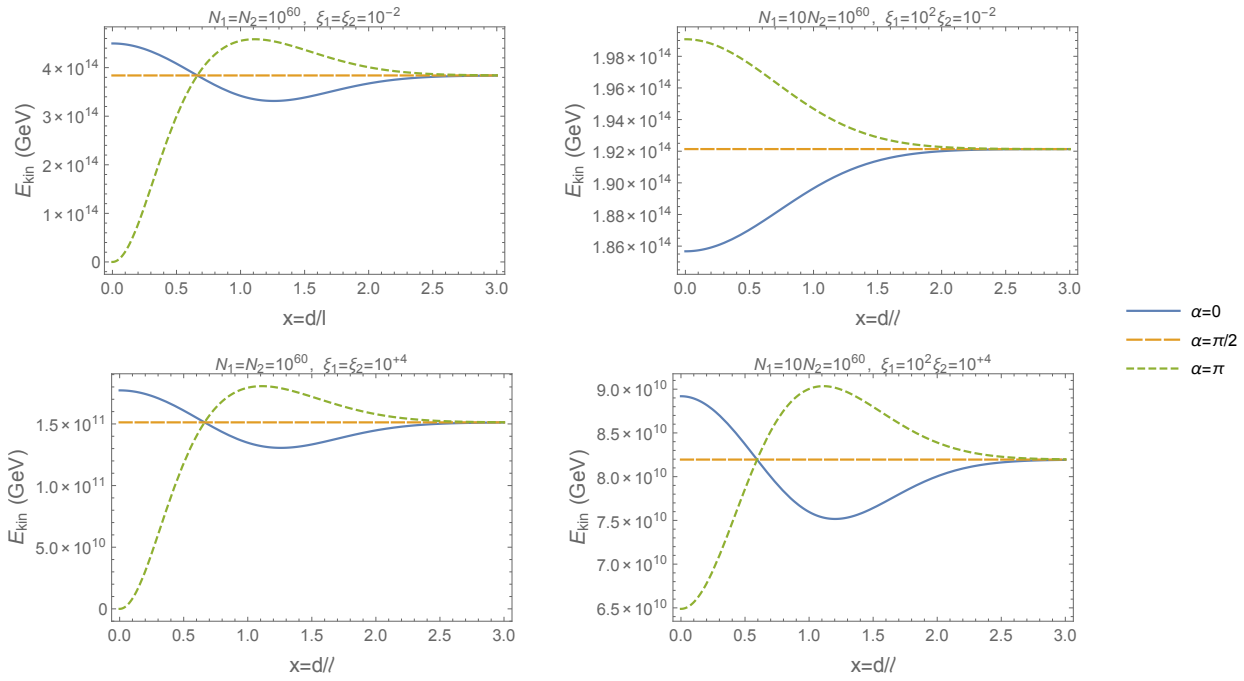

Figure 2.1: Total kinetic energy as a function of scaled separation distance $x = d/\ell$. Solitons of comparable size (left column) have a phase-dependent bump or trough. Binaries where one soliton has much more mass than the other (right column) no longer exhibit this property, unless the self-interaction is very strongly repulsive. Solitons with weak repulsive interactions (top row) have different behaviors in these two regimes, while those with strong repulsive interactions (bottom row) look very similar.

region with a bit of skepticism.

When moving along these energy curves slowly enough, the solitons should track the state of lowest energy. If the kinetic contribution to the total energy were the only relevant part, this lowest energy state should be the bottom of the potential well around $x = 1.3$ when $\alpha = 0$, meaning a bound state will form. However, there are still the self- and gravitational interactions to consider, which will change the shape of this curve.

Performing the same procedure as above, we may compute the self-interaction contribution to the energy:

$$E_{\rm int} = \frac{\pi^{3/2}\lambda A^4}{64m^2}\left[N_1k_1^3 + N_2k_2^3 + \frac{32\sqrt{N_1N_2}}{(k_1k_2)^{3/2}}\left(N_1\left(\frac{k_1}{\ell_1}\right)^3 e^{-3(d/\ell_1)^2} + N_2\left(\frac{k_2}{\ell_2}\right)^3 e^{-3(d/\ell_2)^2}\right)\cos\alpha \right.$$
$$\left. + \frac{4\sqrt{2}N_1N_2}{\ell^3}e^{-2(d/\ell)^2}(2+\cos(2\alpha))\right] \tag{2.23}$$

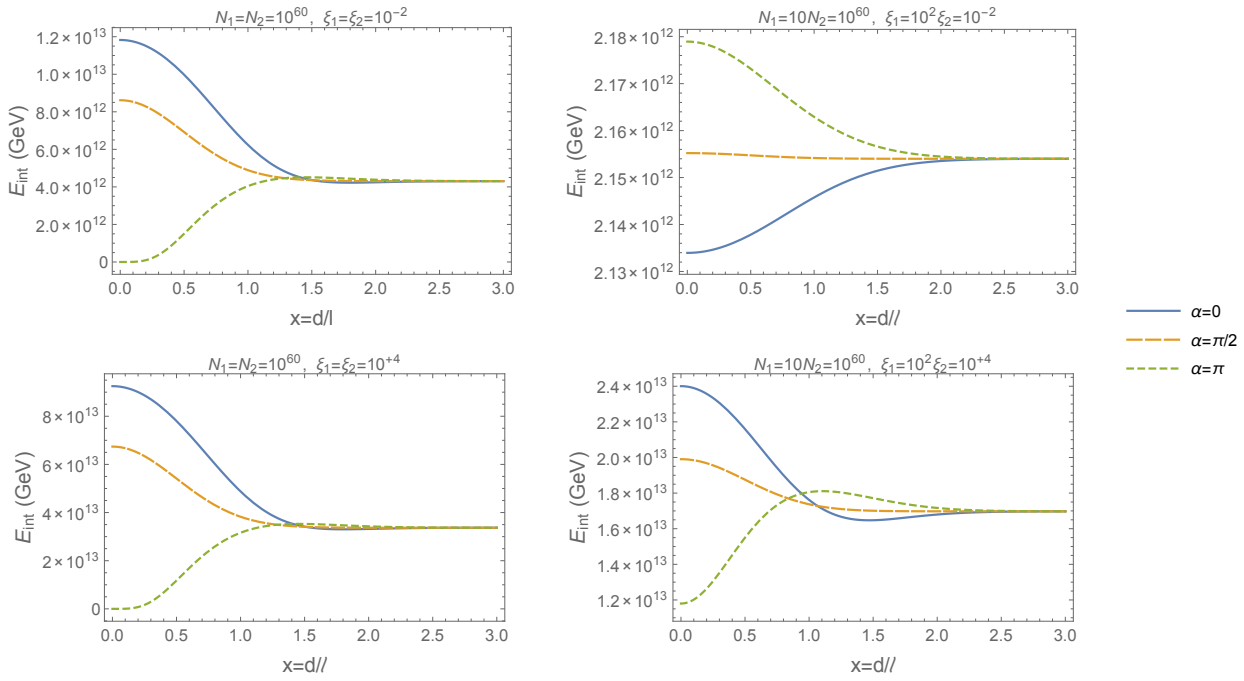

Figure 2.2: Self-interaction energy as a function of scaled separation distance $x = d/\ell$. Solitons of comparable size (left column) exhibit either a repulsive or attractive mutual force depending on phase difference, the shape of which is independent of self-interaction strength. Solitons of asymmetric masses (right column) have a more curious behavior.

There are two more length scales in addition to ℓ, $\ell_i = \ell\sqrt{1 + 2k_i^2/(k_1^2 + k_2^2)}$. It is clear that if $k_i/k_j \ll 1$, then $\ell_i \to \ell$, and if $k_i/k_j \gg 1$, then $\ell_i \to \sqrt{3}\ell$, with intermediate cases falling somewhere in between.

This self-interaction energy is plotted as a function of separation distance in fig. 2.2. We may see that in the case of $\lambda > 0$, the mutual force between the two solitons is not necessarily repulsive, and depends on both the relative phase and size of the objects. Specifically, for stars of comparable mass, the interaction is repulsive for wave functions in phase, and attractive for wave functions out of phase. For stars of asymmetric masses, the interaction is attractive for in phase wave functions, and repulsive for out of phase wave functions in the weak self-interaction regime. This behavior is switched in the strong self-interaction regime, where an additional bump/trough forms just as in the kinetic term. In the $\lambda < 0$ case, there is no such thing as the strongly-interacting regime, as the individual solitons would be unstable, and behavior is similar to the weak-interaction regime for $\lambda > 0$, but with the sign of the energy switched.

The third and final term in the Hamiltonian is the gravitational interaction term. It is composed of four sub-terms which we may break up in the following manner (recalling $\psi = A(\psi_1 + e^{i\alpha}\psi_2)$ and that the integral is invariant under relabeling $\vec{x} \leftrightarrow \vec{x}'$ since the integration regions are the same):

$$\begin{aligned} E_{\text{grav}} &= -\frac{Gm^2}{2}\int d^3x\, d^3x'\, \frac{|\psi(\vec{x})|^2|\psi(\vec{x}')|^2}{|\vec{x}-\vec{x}'|} \\ &= -\frac{1}{2}Gm^2A^4\int d^3x\, d^3x' \Bigg[\underbrace{\psi_1^2(\vec{x})\psi_1^2(\vec{x}')+\psi_2^2(\vec{x})\psi_2^2(\vec{x}')}_{\text{soliton self-energy}} + 2\underbrace{\psi_1^2(\vec{x})\psi_2^2(\vec{x}')}_{\text{classical gravity}} \\ &\quad +4\cos\alpha\,\underbrace{\psi_1(\vec{x})\psi_2(\vec{x})\left(\psi_1^2(\vec{x}')+\psi_2^2(\vec{x}')\right)}_{\text{long-distance interference}} + 4\cos^2\alpha\,\underbrace{\psi_1(\vec{x})\psi_2(\vec{x})\psi_1(\vec{x}')\psi_2(\vec{x}')}_{\text{short-distance interference}}\Bigg] /|\vec{x}-\vec{x}'| \end{aligned} \tag{2.24}$$

The self-energy term is simply the binding energies of the individual solitons, and can be coordinate transformed so that it is spherically symmetric and is easily solved:

$$I_1 = \sqrt{2}\pi^{5/2}\left(\frac{A_1^4}{k_1^5}+\frac{A_2^4}{k_2^5}\right) = 8\sqrt{\frac{2}{\pi}}\left(N_1^2k_1+N_2^2k_2\right) \tag{2.25}$$

This term, along with the "classical gravity" term are what you would expect if we were using regular mass densities $\rho = \rho_1 + \rho_2 = \psi_1^2 + \psi_2^2$. However, since we are using wave functions, we must add them together, then square, introducing interference effects. The "long distance interference" term is identified as such because it contributes more weight to the integral when $\vec{x}'$ is close to the center of either one of the solitons, whereas the "short distance interference" term must have $\vec{x}'$ near the center of both solitons to contribute significantly. Besides the first term, this expression is not analytically soluble, but we can make some headway numerically by using the Green function in cylindrical coordinates [113]:

$$g(\vec{x},\vec{x}') = \frac{1}{4\pi|\vec{x}-\vec{x}'|} = \frac{1}{2\pi^2}\sum_{m=-\infty}^{\infty}\int_0^\infty dk\, I_m(ks_<)K_m(ks_>)e^{im(\phi-\phi')}\cos(k(z-z')) \tag{2.26}$$

Due to cylindrical symmetry, only the $m = 0$ term contributes to the sum after integration over ϕ, ϕ', and the integrations over z, z' can be performed analytically, leaving us with a triple integral over s, s' and k. This must be evaluated numerically. Transforming to dimensionless units $(\sigma, \sigma', \kappa, x) \equiv (s/\ell, s'/\ell, \ell k, d/\ell)$, the expression to integrate shall be

$$\begin{aligned} E_{\text{grav}} = -4\pi^2 G m^2 A^4 \ell^3 \int_0^\infty d\kappa \int_0^\infty d\sigma\sigma \left[\int_0^\sigma d\sigma'\, \sigma' I_0(\kappa\sigma') K_0(\kappa\sigma) + \int_\sigma^\infty d\sigma'\, \sigma' I_0(\kappa\sigma) K_0(\kappa\sigma') \right] \\ \times \left[\frac{A_1^4}{2k_1^2} e^{-\kappa^2/4\ell^2 k_1^2} e^{-2\ell^2 k_1^2(\sigma^2+\sigma'^2)} + \frac{A_2^4}{2k_2^2} e^{-\kappa^2/4\ell^2 k_2^2} e^{-2\ell^2 k_2^2(\sigma^2+\sigma'^2)} \right. \\ +4A_1 A_2 \cos\alpha e^{-x^2-\ell^2(k_1^2+k_2^2)\sigma^2} \left(\frac{A_1^2 \cos\left(\frac{x\kappa}{\ell^2 k_1^2}\right)}{\sqrt{2}k_1\sqrt{k_1^2+k_2^2}} e^{-\frac{\kappa^2\ell_1^2}{8\ell^4 k_1^2}} e^{-2\ell^2 k_1^2\sigma'^2} + \frac{A_2^2 \cos\left(\frac{x\kappa}{\ell^2 k_2^2}\right)}{\sqrt{2}k_2\sqrt{k_1^2+k_2^2}} e^{-\frac{\kappa^2\ell_2^2}{8\ell^4 k_2^2}} \right) \\ \left. + \frac{4A_1^2 A_2^2 \cos^2\alpha}{k_1^2+k_2^2} e^{-2x^2-\frac{\kappa^2}{2\ell^4 k_1^2 k_2^2}} e^{-2\ell^4 k_1^2 k_2^2(\sigma^2+\sigma'^2)} + \frac{A_1^2 A_2^2}{k_1 k_2} \cos(\kappa x) e^{-\kappa^2/8} e^{-2\ell^2(k_1^2\sigma^2+k_2^2\sigma'^2)} \right] \end{aligned} \tag{2.27}$$

Evaluation of this integral for various values of x and α lead to the plots of fig. 2.3. We can see that at long distances, the gravitational interaction energy asymptotically approaches $-GM_1M_2/x - E_1 - E_2$, as one would expect from Newtonian theory. As the distance closes, a prominent rise in energy appears for relative phase $\alpha = \pi$. In the $N_1 \sim N_2$ regime, this rise can even cause the gravitational contribution to become positive (mildly disturbing, but we don't expect this analysis to be valid in the $x \ll 1$ limit as mentioned before), and clearly signals a strongly repulsive interaction. For relative phases less than about $\pi/2$, the energy falls, signaling a mildly attractive force, and potential merger. We can see that in the $\xi \gg 1$ regime, the gravitational binding energy is many orders of magnitude smaller than the equivalent situation with $\xi \ll 1$ due to the internal repulsive force spreading out the soliton.

Having evaluated and discussed the behavior of each of the contributions to the total energy separately, it is now of interest to see what they look like summed together into an effective potential, so that we may grasp the overall behavior of the interaction, which is plotted in fig. 2.4. The effective potential curves in each parameter regime are markedly different from each other, though with some unifying overall behavior. First, we may observe that in the

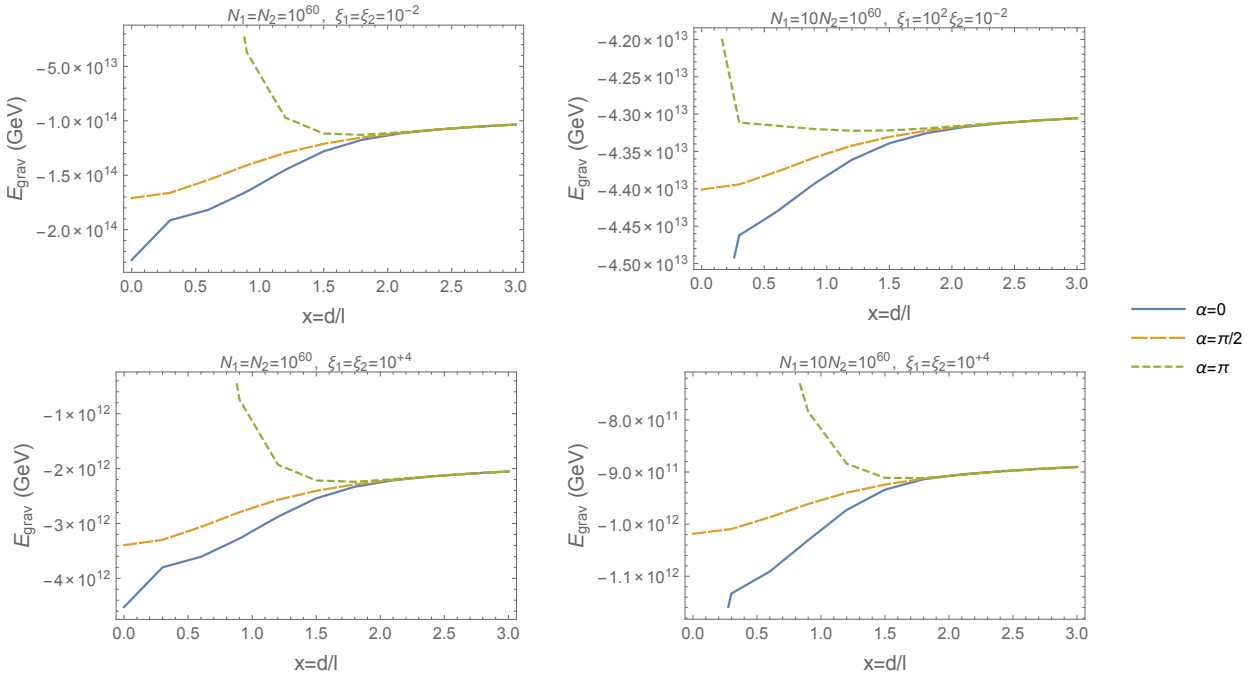

Figure 2.3: Gravitational energy as a function of scaled separation distance $x = d/\ell$. Solitons exhibit a universal behavior of mutual attraction when the relative phase is small, and mutual repulsion when the relative phase is close to $\alpha = \pi$. This repulsive behavior is very strong at small separations except in the case of asymmetric size solitons with weak self-interaction (top right).

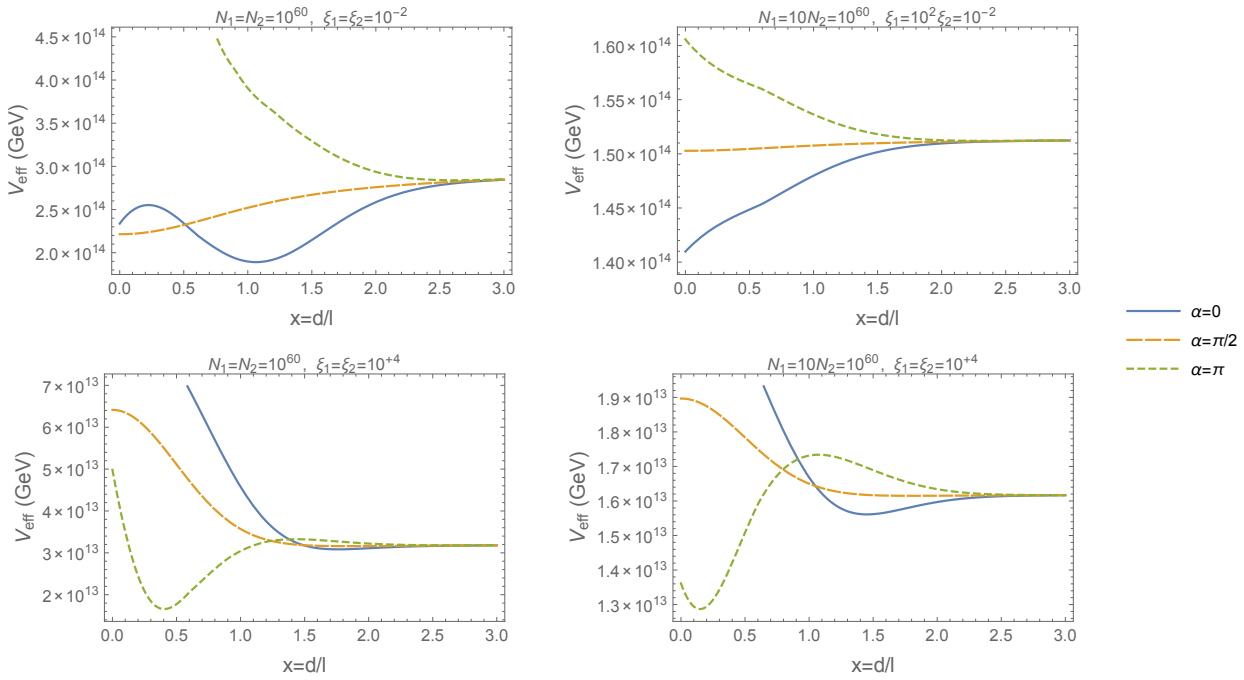

Figure 2.4: Effective potential (total energy) as a function of scaled separation distance $x = d/\ell$. Solitons exhibit a complicated interaction based on the physical parameters, though it is apparent that for $\xi \ll 1$ (top row), solitons in phase have a roughly attractive interaction, while pairs that are out of phase are roughly repulsive. For $\xi \gg 1$ (bottom row), this behavior is switched.

$\xi < 1$ regime, in phase solitons are attractive, whereas out of phase solitons are repulsive. In the $\xi > 1$ regime, this is switched. This is because the self-interaction contribution to the energy dwarfs the kinetic and gravitational contributions in this regime, and so the total energy is decently approximated by that term alone. Interesting to note is that in both the ($N_1 \sim N_2$, $\xi \ll 1$) and ($N_1 \gg N_2$, $\xi \gg 1$) regimes, a local minimum appears in the $\alpha = 0$ energy curve, suggesting a permanent bound state may be formed. In the first case, this does not appear likely, as the kinetic energy gained falling into this minimum from infinitely far away should be enough to avoid being bound and make it through the dip to $x = 0$, where a merger will occur, unless there is some initial kinetic energy allowing them to escape. In the second case, provided the initial kinetic energy isn't too high, a bound state does appear likely to form since the $\alpha = 0$ curve turns sharply upwards, creating a barrier to merger. The $\alpha = \pi$ curve, however, provides much less resistance to merger due to the much smaller energy barrier. Curiously, since it is more energetically favorable for the two solitons to be out of phase in the $\xi \gg 1$ regime at small x, it may be possible to have a shell-like structure where the core of the star is out of phase with respect to the exterior. This would result in a node in the radial wave function, leading one to believe that excited states may easily be formed from collisions of this type.

2.4 Numerical Simulation

In order to verify the above scattering predictions, I have employed a number of numerical simulations. These simulations solve the time-dependent Schrödinger-Poisson system with nonlinear self-interaction for initial states of two solitons, which are then evolved in time to determine scattering behavior. The code utilizes a grid method to calculate the wave function ψ by discretizing Schrödinger's equation on a 3D Cartesian grid and using a 2nd-order center-time, 1st-order center-space (CTCS) algorithm ($\partial\psi/\partial t \rightarrow (\psi(t+dt) - \psi(t-dt))/2dt$, $\partial^2\psi/dx_i^2 \rightarrow (\psi(x_i+dx_i) - 2\psi(x_i) + \psi(x_i-dx_i))/dx_i^2$) to iterate the value of the field at each grid point in time. The gravitational potential ϕ is also discretized on the same grid, and is solved for using a successive over-relaxation (SOR) algorithm with the ψ field from the

previous time step as the source. In order to satisfy the boundary condition that both ψ and ϕ should vanish at infinity, I have performed an asymptotic coordinate transformation $\chi_i = \tanh(x_i/R)$ to map the domain from $\mathbb{R}^3 \to [-1,1]^3$, which allows Dirichlet conditions to be imposed on the boundary of the box $[-1,1]^3$. The relation between the probability densities in these two coordinate systems is then

$$|\psi(\vec{x})|^2\, d^3x = |\psi(\vec{\chi})|^2 \left|\frac{\partial(x,y,z)}{\partial(\chi_1,\chi_2,\chi_3)}\right| d^3\chi = \frac{|\psi(\vec{\chi})|^2 R^3}{(1-\chi_1^2)(1-\chi_2^2)(1-\chi_3^2)} d\chi_1\, d\chi_2\, d\chi_3 \tag{2.28}$$

The parameter R is a scaling factor which is roughly the spatial extent of the radius within which the simulation should be contained. Outside this radius, the simulation will still run correctly, but spatial distances are severely distorted and might not capture all the details of the evolution. In terms of the discretized χ variables, Schrödinger's equation can be solved for the value of ψ at successive time steps:

$$\begin{aligned}\psi^{n+1}_{i_1,i_2,i_3} = \psi^{n-1}_{i_1,i_2,i_3} + \frac{i\,dt}{(d\chi\, R)^2 m}\big[&(1-\chi_1^2)(1-\chi_1^2-\chi_1\, d\chi)\psi^n_{i_1+1,i_2,i_3} \\ &+(1-\chi_1^2+\chi_1\, d\chi)\psi^n_{i_1-1,i_2,i_3} - 2(1-\chi_1^2)\psi^n_{i_1,i_2,i_3}\big] \\ &+(1\leftrightarrow 2)+(1\leftrightarrow 3) - \frac{i\lambda\, dt}{4m^2}|\psi^n_{i_1,i_2,i_3}|^2\psi^n_{i_1,i_2,i_3} - 2im\, dt\, \phi^n_{i_1,i_2,i_3}\psi^n_{i_1,i_2,i_3}\end{aligned} \tag{2.29}$$

where n denotes the time step and the i's index spatial grid points. ϕ refers to the gravitational potential, which is solved using the aforementioned SOR algorithm:

$$\begin{aligned}\phi^{n,n_r+1}_{i_1,i_2,i_3} = (1-\omega)\phi^{n,n_r}_{i_1,i_2,i_3} + \frac{\omega}{2\sum_{i=1}^3(1-\chi_i^2)^2}\big[&(1-\chi_1^2)(1-\chi_1^2-\chi_1\, d\chi)\phi^{n,n_r}_{i_1+1,i_2,i_3} \\ &+(1-\chi_1^2+\chi_1\, d\chi)\phi^{n,n_r+1}_{i_1-1,i_2,i_3} + (1\leftrightarrow 2)+(1\leftrightarrow 3) - 4\pi GmR^2\, d\chi^2|\psi^n_{i_1,i_2,i_3}|^2\big]\end{aligned} \tag{2.30}$$

where $\omega = 1.9$ is the over-relaxation parameter, and n_r denotes the relaxation time step. This is run repeatedly until the error between steps $(\phi^{n_r+1} - \phi^{n_r})/\phi^{n_r+1} < 10^{-4}$. As initial states, I take a superposition of two stationary states, similar to that of eqn. 2.18, though

with additional non-constant phase factors to account for initial velocities:

$$\Psi(\vec{r}, t_0) = A\left[\psi(\vec{r} - \vec{d}/2)e^{im\vec{v}_1\cdot\vec{r}} + e^{i\alpha}\psi(\vec{r} + \vec{d}/2)e^{im\vec{v}_2\cdot\vec{r}}\right] \tag{2.31}$$

where ψ is the stationary wave function, m is the mass of the scalar particle, α a constant phase factor, and $\vec{v}_i$ are the initial velocities. I do not use initial momentum here because the quantity in the exponential would be the average momentum *per particle*, which is somewhat confusing, especially in scenarios where the two solitons are different masses. In most of the cases that will follow, nonzero initial velocities will be equal and opposite: $\vec{v}_1 = -\vec{v}_2 \equiv \vec{v}$. In order to verify the predictions of the previous sections, I will perform a number of simulations under different conditions, listed here for clarity:

A. $N_1 = N_2$, $\xi \ll 1$, $\alpha = 0$, $v_0 = 0$: predicted to fall together then merge.

B. $N_1 = N_2$, $\xi \ll 1$, $\alpha = 0$, $v_0 \neq 0$: predicted to fall together, then pass through each other mostly intact.

C. $N_1 = N_2$, $\xi \ll 1$, $\alpha = \pi$, $v_0 = 0$: predicted to fall towards each other, reflect, then sit adjacent until eventual merger.

D. $N_1 = N_2$, $\xi \gg 1$, $\alpha = \pi$, $v_0 = 0$: predicted to fall towards each other and merge.

E. $N_1 \gg N_2$, $\xi \ll 1$, $\alpha = \pi$, $v_0 = 0$: predicted to fall towards each other, reflect, then sit adjacent until eventual merger.

F. $N_1 \gg N_2$, $\xi \gg 1$, $\alpha = 0$, $v_0 = 0$: predicted to fall towards each other, reflect, then sit adjacent to each other for an extended period (possibly indefinitely).

G. Single large soliton with self-interaction parameter past critical range $\xi < -1$: predicted to fracture into multiple smaller solitons.

There are too many parameter combinations to cover the entire parameter space, so we will focus on those with possibly interesting effects. In what follows, I will present the results of the simulations in the form of snapshots of the system at relevant times (where t refers

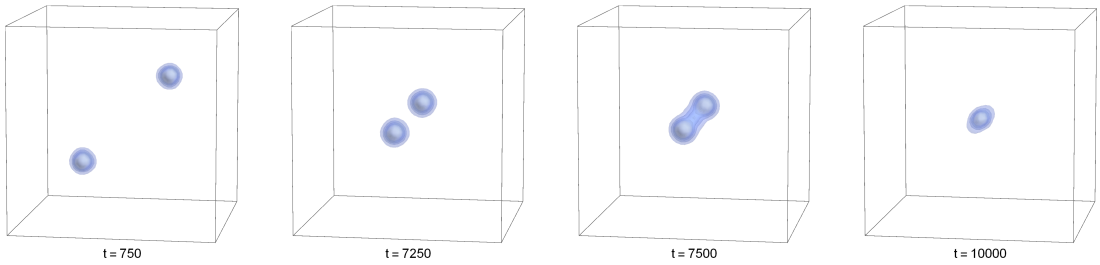

Figure 2.5: Snapshots of two colliding boson stars with $N_1 = N_2 = 10^{60}$, $\xi_1 = \xi_2 = 10^{-2}$, $\alpha = 0$ and $v_0 = 0$, explained in section (2.4.1).

to the number of timesteps since the simulation was initiated). The plots are of surfaces of constant $|\psi|^2$, with different contours representing half-logarithmic steps ($c_n = 10^{n/2}$).
The numerical stability of these simulations are governed by three different stability parameters s, s_λ, s_G, that determine the numerical instability corresponding to the dynamical, $\lambda\phi^4$, and gravitational interactions, each of which scales linearly with the time step Δt. For stability to reign, we need all three parameters to be significantly less than unity. This can always be accomplished by making Δt smaller, at the cost of increased CPU time, which scales as Δt^{-1} for simulations of the same length of time. This means that for reasonable-length simulations I can run on commercially-available hardware, I constrain $s \sim 10^{-1}$. Unfortunately, the ratio $s_\lambda/s \sim \xi^{1/2}/M^2$ for large ξ, where M is the number of grid points along one dimension of the simulation, so that simulating very strongly interacting systems becomes infeasible from a computational standpoint. This forces us to consider simulations of only mildly self-interacting systems with $\xi = 10^1$ rather than the $\xi = 10^4$ systems considered in section 2.3. Animations of these simulations can be found online at (`http://ecotner.bol.ucla.edu/Research/Solitons/BoseStars.html`).

2.4.1 $N_1 = N_2$, $\xi \ll 1$, $\alpha = 0$, $v_0 = 0$

In this first simulation, we look at the behavior of two equal-mass boson stars with a negligible self-interaction and no relative phase or initial velocity. As we can see from fig. 2.5, the solitons fall under gravitational attraction toward each other (taking time to accelerate, which explains the large delay between snapshots 1 and 2), merge together, and

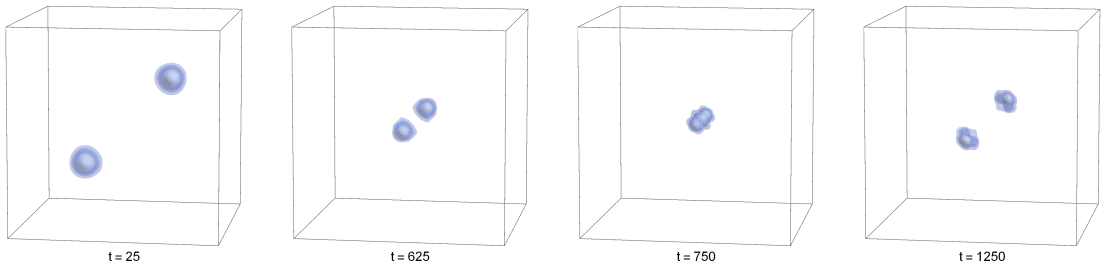

Figure 2.6: Snapshots of two colliding boson stars with $N_1 = N_2 = 10^{60}$, $\xi_1 = \xi_2 = 10^{-2}$, $\alpha = 0$ and $v_0 = 7 \times 10^{-15}$, explained in section (2.4.2).

then sit stationary in the center of mass while experiencing mild radial oscillations which are symmetric under rotations about the axis of approach. This is in line with the prediction from the effective potential: that the system doesn't have enough energy to overcome the hump at the origin and the two solitons merge.

2.4.2 $N_1 = N_2$, $\xi \ll 1$, $\alpha = 0$, $v_0 \neq 0$

In this second simulation, we look at the behavior of two equal-mass boson stars with negligible self-interaction and no relative phase. However, they do have initial velocities (directed towards each other). As we can see from fig. 2.6, the solitons accelerate towards each other, merge briefly, then continue onwards, their trajectories unaltered. This is as expected, as now the system has enough kinetic energy to get over the hump at the origin of the effective potential. Not shown is that significantly after passing through each other, the solitons bloom outward as though torn apart by the interaction. I believe this to be a numerical artefact, and will check with further simulations. If not, collisions of this type might be a possible mechanism for fracturing of larger boson stars into smaller ones.

2.4.3 $N_1 = N_2$, $\xi \ll 1$, $\alpha = \pi$, $v_0 = 0$

This next simulation looks at the effects of initial relative phase differences on the collision. From the effective potential, it appears that a collision between two out-of-phase solitons will result in a repulsive force at close range. As we can see from fig. 2.7, the two stars collide and rebound from each other. The scattering is inelastic, with translational

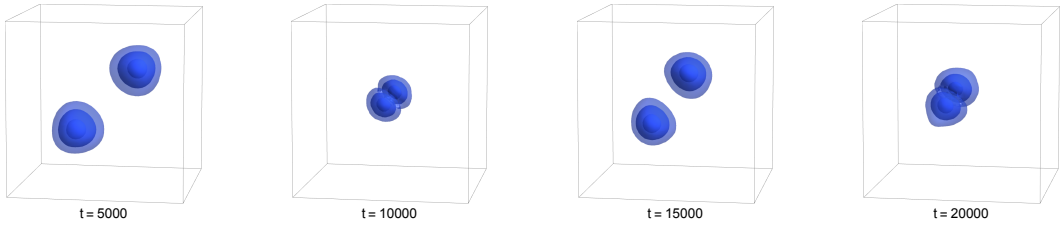

Figure 2.7: Snapshots of two colliding boson stars with $N_1 = N_2 = 10^{60}$, $\xi_1 = \xi_2 = 10^{-2}$, $\alpha = \pi$, and $v_0 = 0$, explained in section (2.4.3).

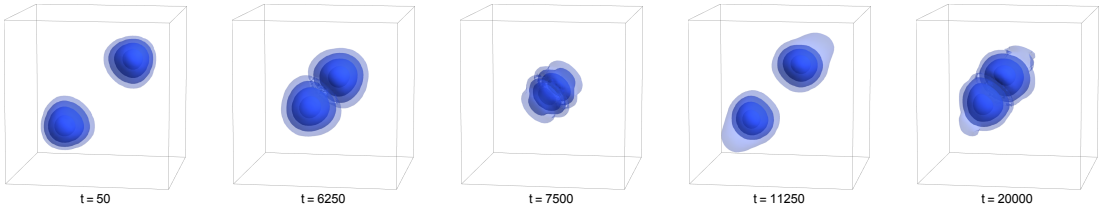

Figure 2.8: Snapshots of two colliding boson stars with $N_1 = N_2 = 10^{60}$, $\xi_1 = \xi_2 = 10^{1}$, $\alpha = \pi$, $v_0 = 0$, explained in (2.4.4).

kinetic energy being converted into vibrational energy with each collision. At much later times, the solitons will eventually merge together, as the phase of their wave functions in the overlap region rotates into some mutual value, and this has been confirmed with extended simulations.

2.4.4 $N_1 = N_2$, $\xi \gg 1$, $\alpha = \pi$, $v_0 = 0$

In this case, we consider a collision between equal mass solitons out of phase with each other in the strongly-interacting regime. From our effective potential plot, we would expect the two solitons to merge easily. Instead, as we can see from fig. 2.8, the solitons rebound off each other (three times in the span of this simulation before merging). The deviation from the potential prediction is likely because the potential is plotted for $\xi = 10^4$, whereas the simulation was performed with $\xi = 10^1$, so that the actual potential is more dominated by the kinetic energy contribution (which is repulsive for out of phase collisions) than the attractive effect of out of phase self-interactions, similar to the simulation of section 4.3.

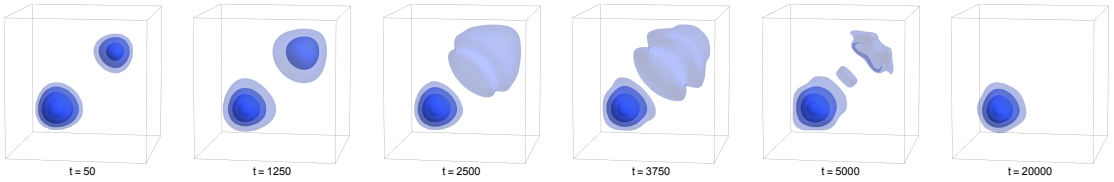

Figure 2.9: Snapshots of two colliding boson stars with $N_1 = 10N_2 = 10^{60}$, $\xi_1 = 10^2\xi_2 = 10^{-2}$, $\alpha = \pi$, $v_0 = 0$, explained in (2.4.5). Star one begins the simulation in the bottom left corner, and star two begins the simulation in the top right.

2.4.5 $N_1 \gg N_2$, $\xi \ll 1$, $\alpha = \pi$, $v_0 = 0$

In this case, we consider a collision between asymmetric masses in the weakly-interacting regime. The two stars are out of phase and so we expect them to repel from each other as they approach. However, this prediction is dependent on the assumption that the soliton stays intact throughout the collision. As we can see from fig. 2.9, the less massive of the two stars is torn apart by tidal forces from the larger one, and material is accreted onto the star. There is mild feedback due to the fact that the two wave functions are out of phase (as seen in the rippling effect as material is siphoned from the smaller star). Since the two bodies cannot merge at once due to the phase mismatch, the smaller star must shed its mass in chunks, which then have their phase rotated to align with the phase of the larger star, and are subsequently absorbed. If there was no phase difference, this piece-by-piece accretion would not occur and would be akin to that of fig. 2.6.

2.4.6 $N_1 \gg N_2$, $\xi \gg 1$, $\alpha = 0$, $v_0 = 0$

Another asymmetric-mass system, we would expect from the effective potential that the binary might be effectively stable against merger, since there is a local minimum in the energy around $x = 1.5\ell$. However, just as the situation of section 4.5, the simulation deviates from expectation, likely due to the effect of tidal forces. As we can see from fig. 2.10, the less massive star (upper right corner) is elongated by tidal forces and quickly accreted onto the more massive one (lower left corner). Due to the underlying grid of the simulation, especially dense configurations (such as the more massive star in this case) can get stuck on a specific grid point if the change in velocity is low enough. In this case, the more massive partner stays

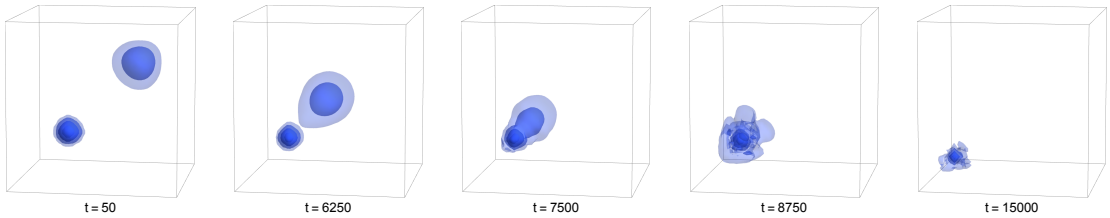

Figure 2.10: Snapshots of two colliding boson stars with $N_1 = 4N_2 = 10^{60}$, $\xi_1 = 4^2\xi_2 = 10^1$, $\alpha = 0$, $v_0 = 0$, explained in (2.4.6). Star one begins the simulation in the bottom left corner; star two in the top right.

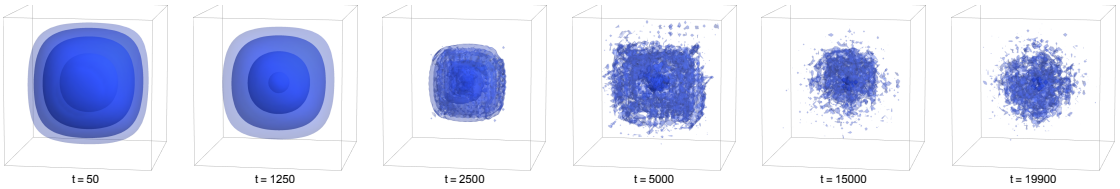

Figure 2.11: Collapse and evolution of an unstable soliton with $N = 10^{60}$ and $\xi = -10$, explained in section (2.4.7).

in the same position until the less massive partner collides with it, transferring momentum and pushing it further into the corner, as observed.

2.4.7 Behavior of unstable soliton with $\xi < -1$

In this situation, we initialize a condensate in the regime $\xi < -1$, which makes the variational energy/wave vector/length scale complex, signifying instability. Since there is no variational state to initialize in, we choose the initial state wave vector to be the imaginary part of the variational wave vector (since the real part is independent of ξ in this regime). We then initialize the simulation with one soliton having these parameters and allow it to evolve undisturbed. What we find is that the condensate collapses under its own gravity to an extremely dense core, with the density jumping up almost three orders of magnitude. Surrounding this core is a cloud of fluctuating points with densities roughly two orders of magnitude below the density of the core. The fact that the wave function has this discrete nature suggests large amounts of interference. This core then further fractures until it is composed of a handful of individual points of roughly the same particle number/mass. This fracturing of the condensate is reminiscent of the same process found in Affleck-Dine models

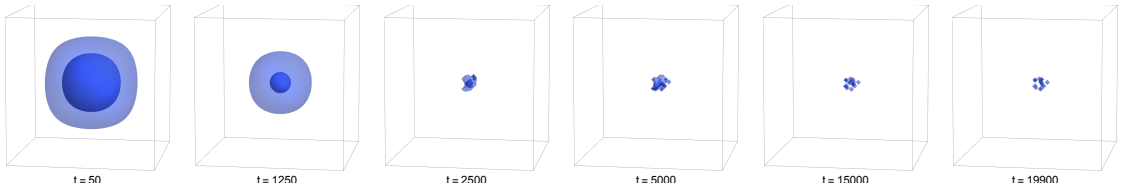

Figure 2.12: Same simulation results as fig. 2.11 from section (2.4.7), but with fluctuations filtered out. Note condensate core which forms at early times $t = 2500$ further breaks up into smaller pieces as time goes on.

of baryogenesis, only in this case the condensate is nonuniform and spherically symmetric to begin with, so it stands to reason it should collapse to a roughly spherical final state.

2.5 Discussion

2.5.1 Results of this paper

This study has explored the various properties of non-relativistic boson stars with a standard ϕ^4 self-interaction. Though this system has been studied before, both analytically and numerically, it has historically been done just for a stationary field configuration of a single soliton [114][115][107]. In recent years, some studies have looked at collisions between boson stars, though they are primarily numerical in scope [116][117][118][119]. This effective potential analysis provides good predictions for collisional behavior under a variety of circumstances and parameter ranges, and gives one the advantage of being able to understand qualitatively the outcome of a collision simply using concepts of conservation of energy. Of course, energy of translational motion of the solitons may be converted to radial oscillations, or even excite the solitons into a higher energy radial state with multiple nodes (as seen in some merger simulations), leading to dissipation of translational motion and eventual merger in most cases. Scattering from a nonzero impact parameter may lead to states with nonzero angular momenta, numerical simulations of which have been studied in [118]. Especially interesting (from an academic point of view) may be the possibility of forming stable bound states in strongly repulsive regimes, with the possibility of a centrifugal barrier provided by a nonzero angular momentum, effectively using this to construct “molecules"

from gravitationally-bound, astrophysical-scale objects.

In terms of support for the predictive ability of the effective potential, it is well supported by the results of many numerical scattering simulations of boson stars. Though not all the parameter space has been adequately explored in the literature, we can make some comparisons with previous numerical studies. Simulations of self-interacting solitons with nonzero relative velocities carried out in [116] appear consistent with the prediction of the effective potential and the results of this studies' simulations. In Bernal and Guzmán's (BG) paper, they study the head-on collision of two in phase ($\alpha = 0$) boson stars with weak quartic self-interaction ($\xi \ll 1$) for both equal mass and asymmetric mass stars. The main result of the paper is that systems with "negative" energy (systems with kinetic and self-interaction energy smaller than the gravitational binding energy) will combine and merge, whereas systems with "positive" energy will behave solitonically and pass right through each other. This is exactly what one would predict from the effective potential, and is confirmed with simulations 2.4.1 and 2.4.2. The effective potential for both mass ratios shows no "hump" at zero separation distance (for $\alpha = 0$), and so traversing through each other is no obstacle provided there is enough translational kinetic energy to make it out of the gravitational well. As mentioned before, there are energy losses from excitation and scalar radiation during the collision, which can be treated as frictional effects, and so one cannot simply expect a system of two boson stars initially at rest with a large separation distance (such as in simulation 2.4.1) to have enough kinetic energy at the point of contact; an initial translational kinetic energy at infinite separation distance is required. This is also confirmed in BG's figures 4 and 5, where they explore the outcome of scattering simulations for varying initial momenta; high relative p leads to solitonic behavior, whereas low p leads to mergers. One downside to the effective potential formalism is that since the two stars are assumed to remain intact, it does not allow for particle transfer during the collision. This is observed in BG's paper, where scattering between asymmetric-mass boson stars appear to transfer mass between each other.

The results of non-self-interacting ($\xi = 0$) boson-boson soliton scattering with different initial phases performed in [117] can be explained easily using the effective potential as well. In

this paper, Palenzuela, Olabarietta, Lehner, and Liebling (POLL) use the full Einstein-Klein-Gordon system, rather than the Schrödinger-Poisson, though the results are quite similar. They consider scattering between both boson-boson and boson-antiboson systems with equal masses and no initial velocities for a variety of initial relative phases, though we will only compare with the boson-boson experiments, for obvious reasons. Their simulation of in-phase scattering and merger agrees with BG's and my simulations, which were discussed above. Their simulation of out-of-phase scattering, which results in the two boson stars rebounding inelastically off each other, agrees perfectly with both the effective potential prediction and the results of my simulation 2.4.3. The effective potential for out-of-phase systems can be seen to rise steeply as the separation distance decreases, indicating a short-range repulsive force, resulting in a gravitationally-bound state, as observed in both POLL's paper an this paper's simulation 2.4.3.

Unfortunately, there appear to be no discussions in the literature regarding collisions between very strongly self-interacting ($\xi \gg 1$) boson stars, nor collisions between asymmetric-mass stars with $\alpha \neq 0$. Consequently, we cannot compare the results of this study to the existing literature, and it appears that this is the first attempt at simulating collisions in this parameter range. However, this is precisely this parameter range that likely requires further study, as there are multiple instances where the effective potential does not give good predictions that coincide with the outcome of the simulations. In particular, asymmetric-mass boson stars with low initial velocities are highly influenced by tidal forces, causing the smaller partner of the binary to be torn apart and accreted onto the larger partner, regardless of the value of α. I expect that for nonzero initial velocities, where the time the two solitons spend in each other's company is reduced, the effect of tidal forces should also be reduced. The timescale of the evolution of the wave function is roughly $1/m$ and a collision that occurs on a timescale shorter than this should therefore not affect the overall shape of the boson star. As for simulations in the strongly-interacting regime, the reason the literature does not focus on this regime is likely for the same reason given in section 2.4: increasing the value of ξ increases the instability associated with the self-interaction term in the simulation, which requires the use of smaller and smaller time steps, making simulation in the $\xi \gg 1$ regime

very computationally expensive. In addition, there is almost no discussion of boson stars with $\xi < 0$, likely due to the resultant collapse of the star.

2.5.2 Implications for dark matter

Dark matter of this composition can take on a phenomenally large array of forms, and depending on the mass of the constituent particles, can form astrophysical objects as massive as entire galaxies, and as far as I know, no lower bound on their mass exists. They can be extremely diffuse (especially in the $\xi \gg 1$ limit), leading some to interpret the galactic DM halo as a single boson star [114][120]. This has the advantage of naturally resolving the cusp-core problem without invoking self-interactions, and their propensity to merge through low relative-velocity collisions may help explain the lack of predicted satellite galaxies. On the other hand, head-on collisions at sufficient speed can cause the DM halos to pass right through each other, as is observed in the Bullet Cluster. They can also be extremely compact, guarded against collapse to a black hole by a strong repulsive self-interaction, or if attractive, can readily collapse to a black hole at some critical mass. If this is the case, supermassive black holes at the centers of galaxies may be made of - or initially formed from - boson stars [72]. Somewhere between these two extremes, these configurations can form roughly stellar-mass objects that may have interesting interactions with themselves or existing stellar populations in the disk. As mentioned before, the MACHO, EROS and OGLE collaborations have all independently found a significant excess of gravitational lensing events over the number expected. Though limits have been placed on the maximum fraction of the halo mass that these objects can make up, they may still exist in a partially condensed phase, where some of the particles are contained in compact objects while others would be free-streaming. Objects on an infall trajectory from the outer parts of the halo could transfer momentum to stars and other dark objects in the galactic center through the collisional interactions elucidated in this paper, reducing the central density, as is observed in multiple DM-dominated dwarf spheroidal galaxies. Even in the non-self-interacting limit, these solitons can rebound off each other to transfer momentum and mass purely through gravity and BE statistics. Though I do not explore any of these ideas in detail in this paper,

further work must be done to determine if any of these scenarios are consistent or desirable.

2.6 Conclusion

I have presented approximate analytical solutions to the nonlinear Schrödinger-Poisson system, constructed stable solitonic states, and explored the collisional interactions between two solitons. I have found that these boson stars can exist in a wide range of stable states, with a number of properties that make them good candidates for dark matter, such as momentum transfer (or lack thereof) through scattering and gravitational encounters, and their wide range of possible masses, densities, and length scales make them a general prediction of practically any theory of a cold, light scalar particle. I have elucidated the mechanism behind the results of direct collisions, finding it to be dependent on the relative phase, mass ratios, and self-coupling of the solitons in a way that is easily understandable in terms of energy conservation once the effective potential has been calculated. Some of these results in the weakly self-interacting regime have been confirmed by other numerical studies, while collisions with strong self-coupling and nonzero orbital angular momentum should be tested and treated in future work.

2.7 Acknowledgment

I would like to thank Alexander Kusenko for invaluable guidance while performing this work, and for useful comments during the writing/editing process; Rhyan Ghosh for helpful discussions and for keeping me focused when I didn't feel like doing any work; and the anonymous Reviewer who made many helpful suggestions regarding the presentation and scope of the paper.

CHAPTER 3

Infection of Neutron Stars by Baryonic Q-balls

The content of this chapter has been published in Physical Review D as *Astrophysical constraints on dark-matter Q-balls in the presence of baryon-violating operators*, E. Cotner and A. Kusenko, Phys. Rev. D **94**, no. 12, 123006 (2016) [121].

Supersymmetric extensions of the standard model predict the existence of non-topological solitons, Q-balls. Assuming the standard cosmological history preceded by inflation, Q-balls can form in the early universe and can make up the dark matter. The relatively large masses of such dark-matter particles imply a low number density, making direct detection very challenging. The strongest limits come from the existence of neutron stars because, if a baryonic Q-ball is captured by a neutron star, the Q-ball can absorb the baryon number releasing energy and eventually destroying a neutron star. However, in the presence of baryon number violating higher-dimension operators, the growth of a Q-ball inside a neutron star is hampered once the Q-ball reaches a certain size. We re-examine the limits and identify some classes of higher-dimensional operators for which supersymmetric Q-balls can account for dark matter. The present limits leave a wide range of parameters available for dark matter in the form of supersymmetric Q-balls.

3.1 Introduction

Supersymmetric (SUSY) extensions of the standard model predict a scalar potential with a large number of flat directions [122]. Such potentials admit stable configurations, SUSY Q-balls [29, 31, 123]. Even if the scale of supersymmetry breaking is well above the reach of the present collider experiments, the flat directions can exist at a high scale and can

play an important role in cosmology. If inflation took place in the early universe, a scalar condensate can form along the flat directions, leading to matter–antimatter asymmetry[62, 63, 124]. In general, this scalar condensate is unstable with respect to fragmentation into Q-balls [31, 125, 126, 127], which can be entirely stable and can play the role of dark matter [31, 124, 128, 129]. This scenario offers a common origin to ordinary matter and dark matter.

Dark-matter Q-balls have relatively large masses, and, therefore, very small number densities. A direct detection of such dark matter is extremely challenging [125, 130]. These flat directions are only flat at tree level, and in general they are lifted by non-renormalizable terms in the potential coming from loop corrections and GUT or Planck-scale physics, taking the form of polynomials in the squark fields and their conjugates

$$V_{\text{lifting}} = \frac{g}{\Lambda^{n+m-4}}\phi^n(\phi^*)^m + \text{c.c.} \tag{3.1}$$

suppressed by some energy scale $\Lambda \sim 10^{16}$ GeV. If $n \neq m$, then baryon number is no longer conserved, fulfilling one of the Sakharov conditions for baryogenesis [131]. The same operators will destabilize the Q-ball [132] and allow it to decay via processes that do not conserve the baryon number. If supersymmetric Q-balls make up the main component of dark matter, limits on their lifetimes (namely $\tau \gtrsim H^{-1}$) restrict the set of operators in the lifting potential in order to prevent their decay on too short of a timescale.

However, one can set additional constraints on the types of operators in the lifting potential by examining the effects of a star infected with a Q-ball. A Q-ball composed of squarks in the presence of baryonic matter absorbs the net baryon number and radiates pions on its surface [133]. For a main sequence star, a Q-ball should pass through with a negligible change in velocity, due to the relatively low density of the star, and high inertia of the Q-ball. A neutron star, however, has a high enough density of baryons that a collision with a Q-ball should slow it to a crawl, at which point it would sink to the center of the star and begin to consume it from the inside out [134, 133]. If the Q-ball is absolutely stable, it grows without bound as it absorbs more neutrons until either the neutron star is completely consumed, or the Q-ball collapses into a black hole, causing the neutron star to collapse. Either way, we

find the star dies relatively quickly on cosmological timescales, on the order of 10^8 years.

However, the baryon number violation at a high scale is both plausible and necessary for the Affleck-Dine baryogenesis to work. In the presence of baryon-number violating operators, the growth of a Q-ball inside a neutron star may be stymied by the baryon number destruction in the Q-ball interior, which becomes important once the Q-ball VEV reaches a certain magnitude [133, 135]. In this paper, we will re-examine the astrophysical bounds taking into account the baryon number violating operators. The paper is organized as follows: section 3.2 provides a brief review of allowed Q-ball states, section 3.3 explains the machinery of calculating the decay rate of the Q-ball, section 3.4 details the interaction of the Q-ball with a neutron star, and section 3.5 explains the evolution of the baryon number within the Q-ball and star. Section 3.6 takes this analysis and applies limits to the class of baryon-violating operators.

3.2 Stable Q-ball states

We begin with a review of the stable ground states of Q-balls. The minimum necessary ingredients are a complex scalar field ϕ with a U(1) symmetry unbroken at the origin $\phi = 0$. Given a theory of multiple scalar fields with the action

$$S = \int d^4x \left[\partial_\mu \phi_i^\dagger \partial^\mu \phi_i + \frac{1}{2}\partial_\mu \chi_j \partial^\mu \chi_j - V(\phi_i, \chi_j)\right] \tag{3.2}$$

We can perform a Legendre transformation to get the Hamiltonian density of the theory, which gives us a functional for the energy.

$$E = \int d^3x\, \mathcal{H} \tag{3.3}$$

$$\mathcal{H} = |\dot{\phi}_i|^2 + |\nabla \phi_i|^2 + \frac{1}{2}\dot{\chi}_j^2 + \frac{1}{2}(\nabla \chi_j)^2 + V(\phi_i, \chi_j) \tag{3.4}$$

Explicitly adding a Lagrange multiplier $\omega_i \left(Q_i - i \int d^3x \left(\dot{\phi}_i^\dagger \phi_i - \phi_i^\dagger \dot{\phi}_i \right) \right)$ to enforce charge conservation, we get a modified energy functional

$$\mathcal{E} = \int d^3x \, \tilde{\mathcal{H}} + \omega_i Q_i \tag{3.5}$$

$$\tilde{\mathcal{H}} = |\nabla \phi_i|^2 + \frac{1}{2}(\nabla \chi_j)^2 + \tilde{V}(\phi_i, \chi_j) \tag{3.6}$$

$$\tilde{V}(\phi_i, \chi_j) = V(\phi_i, \chi_j) - \omega_i^2 |\phi_i|^2 \tag{3.7}$$

where we have assumed time dependence $\phi_i = \phi_i(\boldsymbol{x}) e^{i\omega_i t}$ and $\chi_j = \chi_j(\boldsymbol{x})$. If for any value of $\phi, \chi \neq 0$ and $0 < \omega_i < m$ there exists a point where $\tilde{V} < 0$, then stable Q-ball states exist. Furthermore, we can postulate that the stable states will be spherically symmetric, so that they depend only on the radial coordinate r.

3.2.1 Flat direction Q-balls

Assuming $V(\phi) \approx M^4 \sim (1 \text{ TeV})^4$ far from the origin, the vev in the interior of the Q-ball is not well-localized in ϕ-space and the thin wall approximation does not hold. Instead, one can consider a thick-wall variational *ansatz* $\phi = \phi_0 \exp\left(-(r/R)^2\right)$. While the $r \to 0$ behavior may be better described by $\sin(\omega r)/\omega r$, the analysis of Ref. [136] shows that the exponential *ansatz* is in good overall agreement with a numerical solution. Evaluating Eq. (3.5) with the assumption that $\int d^3x \, V \approx 4\pi R^3 M^4/3$, extremizing with respect to R and using Hamilton's equation of motion $\omega = \dot{\theta} = \partial \mathcal{E}/\partial Q$, we arrive at

$$\begin{aligned} \omega &= \pm M \left[4\pi \cdot 3^{3/2}/Q \right]^{1/4} \qquad \phi_0 = M \left[\frac{8Q}{3^{3/2}\pi^2} \right]^{1/4} \\ R &= \frac{1}{M} \left[\frac{3^{1/2} Q}{4\pi} \right]^{1/4} \qquad E = M \left[4\pi \cdot 3^{3/2} Q^3 \right]^{1/4} \end{aligned} \tag{3.8}$$

We can see that these types of Q-balls are stable in the large Q limit since $\omega < m$ for large charge (the critical charge is $Q_c = 12\sqrt{3}\pi (M/m)^4$ with m the mass of the scalar at $\phi = 0$), and $E \propto Q^{3/4}$.

Q-balls of this type are common in supersymmetric theories where a flat direction de-

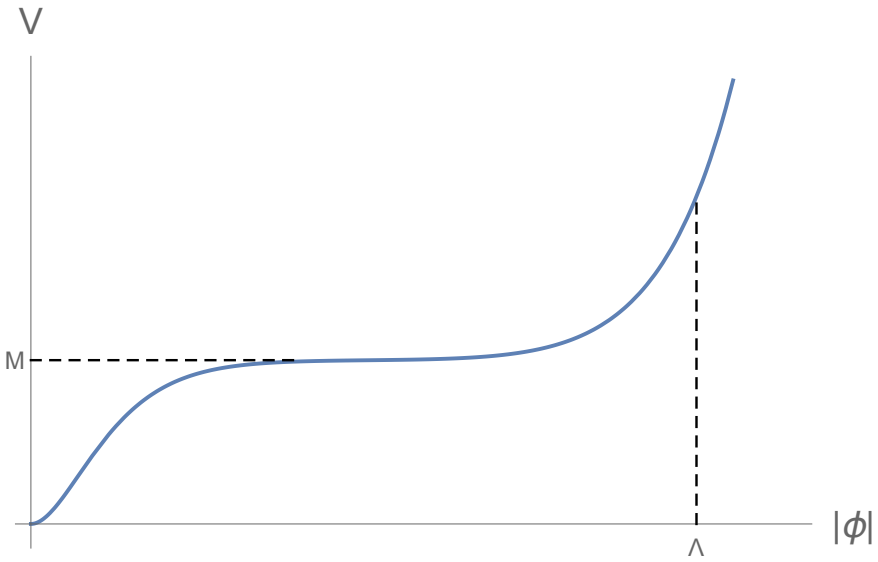

Figure 3.1: Schematic scalar potential with a flat direction which is lifted by higher-dimension terms near $|\phi| \sim \Lambda$. Potentials of this form admit flat direction Q-balls which eventually grow into the curved direction type once the critical charge is surpassed.

velops in the scalar potential for the superpartners of the quarks and leptons [134, **?**]. The conserved U(1) charge in these cases are then lepton and/or baryon number and are referred to in the literature as L-balls and B-balls. In addition to being able to form stable solitons, the interior of these Q-balls can sometimes support lepton- or baryon-violating vacuua [**?**], which may be exploited in theories of baryo- or leptogenesis. Theories with charged inflatons may also be able to support these types of Q-balls since inflaton potentials must be relatively "flat" to satisfy the slow-roll conditions.

3.2.2 Curved direction Q-balls

As the charge of a flat direction Q-ball grows, and the value of the scalar field vev ϕ_0 slides to higher values, the corrections introduced by the lifting potential V_{lifting} begin affecting the Q-ball (see figure 3.1). This happens when $\phi_0 \sim \Lambda$. If the lifting potential is of a form that respects the baryon number conservation, it can continue growing, albeit in a different manner. The vev hits a wall when it reaches its maximum at $\phi_0 = \Lambda$ and cannot climb any

higher, so we can approximate the scalar potential near this point as

$$V(\phi) \approx M^4 + V_{\text{lifting}}^{\not{B}=0} = M^4 + \frac{2\,\text{Re}(g)}{\Lambda^{2n-4}}|\phi|^{2n} \tag{3.9}$$

Since the vev is constrained to be near Λ, we can use the thin wall approximation. Substituting into equation 3.5 and fixing $\phi_0 = \Lambda$, we vary with respect to R to get

$$\begin{aligned} \omega &= \pm\Lambda\sqrt{2\,\text{Re}(g) + (M/\Lambda)^4} \qquad \phi_0 = \Lambda \\ R &= \frac{1}{2\Lambda}\left[\frac{3Q}{\pi\sqrt{2\,\text{Re}(g) + (M/\Lambda)^4}}\right]^{1/3} \\ E &= \Lambda\sqrt{2\,\text{Re}(g) + (M/\Lambda)^4}Q \end{aligned} \tag{3.10}$$

Since we expect $M/\Lambda \ll 1$, we can neglect those terms under the square roots for simplicity. The critical charge at which point a flat direction Q-ball will become a curved direction Q-ball is $Q_c \approx 6.4(\Lambda/M)^4 \sim 10^{52}$.

If the lifting potential is not baryon-conserving, the U(1) symmetry is no longer respected and the Q-ball destabilizes, rapidly decaying until the lifting term is negligible and the Q-ball has reverted back to the flat direction type. Since curved direction Q-balls are necessarily more massive than the flat direction type (and their baryon consumption rate even faster), any limits obtained for flat direction Q-balls will also apply to the curved direction type, so we need only consider those belonging to the flat direction classification from now on.

3.3 The decay rate

We would now like to calculate the decay rate of the quanta of the Q-ball to other particles. The decay of Q-balls to neutrinos was first treated as an evaporation phenomenon due to the Pauli exclusion principle preventing decays in the interior of the Q-ball [137]. Bosons present no such obstacles, and therefore decays to scalar and vector particles can occur throughout the volume of the Q-ball, provided their mass is less than ω. This may be difficult to achieve in general since most coupled scalar/gauge fields will get a mass term

due to the nonzero expectation value in the Q-ball interior. However, the Nambu-Goldstone modes of the Q-ball field itself do not suffer this mass term, and decays to these modes can occur if the $U(1)$ symmetry is very slightly broken by the lifting potential.

Much work has been done calculating the decay and evaporation rates and energy spectra of Q-ball decays to fermions (both massless and massive) [138, 139]. However, these previous studies did not treat decay of the condensate to bosons, and are related, but not relevant to the problem at hand. In this situation, we can utilize a simple method of calculating the decay rate that uses regular perturbation theory (with some extra steps).

3.3.1 Mathematical background

The probability for an initial state $|\{\phi_i\}\rangle$ to evolve into the final state $|\{\phi_f\}\rangle$ is given by $P = |\langle\{\phi_f\}|\{\phi_i\}\rangle|^2$. In the case of decays from a Q-ball, we are interested in the situation where the initial state is simply the scalar condensate describing the Q-ball: $|\phi_c\rangle$. Since the condensate is a persistent feature of the vacuum, the expectation value of the fields operator is simply the wave function: $\langle\phi(x)\rangle = \phi_c(x)$, a c-number function. $\phi_c(x)$ is the solution to the classical equations of motion in vacuum, which admit Q-ball solutions. Therefore, we can decompose the field operator into a classical and quantum part: $\phi = \phi_c + \hat{\phi}$ (we later employ a different decomposition in order to properly separate the field into its mass eigenstates, but it is conceptually similar to this one).

However, we are interested in how the Q-ball decays, so we must consider the state in which the scalar condensate is in the background of an interacting vacuum: $|\Phi_c\rangle$. The transition probability to any set of final state particles $\{\phi_f\}$ is then $P = |\langle\Phi_c|\Phi_c\{\phi_f\}\rangle|^2$. Using the single-particle expansion of the final particle states

$$|\{\phi_f\}\rangle = \int \prod_f \left(\frac{d^3 p_f}{(2\pi)^3} \frac{\phi_f(\boldsymbol{p}_f)}{\sqrt{2E_f}} \right) |\{\boldsymbol{p}_f\}\rangle \tag{3.11}$$

the transition probability is then

$$P = \left| \int \prod_f \left(\frac{d^3 p_f}{(2\pi)^3} \frac{\phi_f(\boldsymbol{p}_f)}{\sqrt{2E_f}} \right) \langle \Phi_c | \Phi_c \{\boldsymbol{p}_f\} \rangle \right|^2 \tag{3.12}$$

Instead of using arbitrary wave functions as the final state, we can simply use the states of definite momentum, as is typically done, so that $\phi_f(\boldsymbol{p}_f) = (2\pi)^3 \delta^3(\boldsymbol{p}_f - \boldsymbol{p})/\sqrt{V}$. In this case, the differential transition probability is then

$$dP = \prod_f \left(\frac{d^3 p_f}{(2\pi)^3} \frac{1}{2E_f} \right) | \langle \Phi_c | \Phi_c \{\boldsymbol{p}_f\} \rangle |^2 \tag{3.13}$$

The matrix element $\mathcal{M} = \langle \Phi_c | \Phi_c \{\boldsymbol{p}_f\} \rangle$ can be computed perturbatively just as is normally done in QFT, except that we have to keep in mind the expansion of the scalar field operator $\phi = \phi_c + \hat{\phi}$. This leads to a bit of a complication, since working in the momentum space involves a Fourier transform of ϕ_c, introducing an additional integral which consumes some of the delta functions that normally can be separated from the scattering amplitude $\mathcal{M}$. In addition, there is also no integral over the impact parameter since there are no collisions involved in this decay process. Depending on the number of interaction vertices in the process, we find the matrix element can be written schematically as

$$\mathcal{M} = \langle \Phi_c | \Phi_c \{\boldsymbol{p}_f\} \rangle = \mathcal{A}_n(\{\boldsymbol{p}_f\})(2\pi)\delta(n\omega - \Sigma_f E_f) \tag{3.14}$$

where ω is the Q-ball energy per particle (chemical potential), n is the number of Q-ball quanta consumed by the decay (determined by the number of external legs attached to the condensate), and $\mathcal{A}$ is a "reduced" matrix element. The delta function enforces global energy conservation, and although momentum is conserved at each vertex internal to the diagram, global momentum is not. This can be understood by the fact that the existence of the condensate breaks the spatial translation invariance of the vacuum, and therefore momentum is no longer a conserved quantity, the condensate instead absorbing the difference, similar to how a crystal lattice will absorb the recoil from a nuclear decay in the Mössbauer effect.

Now, one will find that equation 3.13 implicitly contains the square of a delta function, which is a little troubling. However, integration over the final state momenta will eat up one of the delta functions, leaving a $\delta(0)$, which is proportional to an infinite period of time $T = 2\pi\delta(0)$, in the sense that the limit of T is this quantity, so that stripping this from the RHS gives us a probability per unit time per unit phase space; in other words, the differential decay rate

$$d\Gamma = \prod_f \left(\frac{d^3 p_f}{(2\pi)^3} \frac{1}{2E_f} \right) |\mathcal{A}_n(\{\boldsymbol{p}_f\})|^2 (2\pi)\delta(n\omega - \Sigma_f E_f) \tag{3.15}$$

This method has wide applicability in calculating the decay of condensates and background fields, as the final state particles can be of either bosonic or fermionic type (the initial states can only be bosonic since fermions can't form condensates). The authors have also verified in the limit that the condensate wave function is that of a single zero-momentum particle $\phi_c \sim 1/\sqrt{V}$, the Fourier transform of which is a zero-momentum delta function, the decay rate reduces to that of a familiar single particle decay, as one would expect. The only drawback of this method is that it cannot handle decays that significantly alter the condensate wave function since ϕ_c would then be different in the initial and final states and it would not be appropriate to expand around. Thankfully, we will only be interested in decays involving $\Delta Q \lesssim 10$ from Q-balls with $Q \sim 10^{25}$, so the change in charge per decay is entirely negligible.

3.3.2 Mass eigenstates and phonons

As briefly mentioned earlier, we would like to use a decomposition of the field operator that respects the mass eigenstates of the theory. For a theory with an unbroken U(1), a polar decomposition $\phi = \rho e^{i\theta}/\sqrt{2}$ shows that the scalar potential depends only on the radial field ρ. Therefore, this field is massive with the same mass as the original complex field: $m^2|\phi|^2 = \frac{1}{2}m^2\rho^2$. The potential is completely devoid of any terms containing θ however, due to the U(1) symmetry. This angular degree of freedom is therefore a massless Goldstone boson of the theory (inside the Q-ball it picks up a small mass due to the fact that has a minimum

wavelength $\lambda \sim R$). Therefore we need a representation of the phonon operator that captures perturbations around the condensate while keeping the mass eigenstates separate. This leads us to consider the decomposition of the phonon field into a radial and angular part:

$$\begin{aligned}\phi &= \frac{1}{\sqrt{2}}\rho e^{i\theta} = \frac{1}{\sqrt{2}}(\rho_c + \hat{\rho})e^{i(\theta_c+\hat{\theta})} \\ &\approx \phi_c + \frac{1}{\sqrt{2}}\hat{\rho}e^{i\omega t} + \frac{i}{\sqrt{2}}\hat{\psi}e^{i\omega t} + \cdots\end{aligned} \tag{3.16}$$

where $\hat{\psi} \equiv \rho_c\hat{\theta}$, $\theta_c \equiv \omega t$, and the $\cdots$ refers to the higher-order terms in the Taylor expansion of the exponential. Although there is no way to invert the full relationship for $\hat{\rho}$ and $\hat{\psi}$ in terms of $\hat{\phi}$ and $\hat{\phi}^*$, the expansion to linear order can be inverted, and this gives us an approximate dictionary between the different phonon operators:

$$\begin{aligned}\hat{\phi} = \frac{1}{\sqrt{2}}(\hat{\rho} + i\hat{\psi})e^{i\omega t} \quad \hat{\phi}^\dagger = \frac{1}{\sqrt{2}}(\hat{\rho} - i\hat{\psi})e^{-i\omega t} \\ \hat{\rho} = \frac{1}{\sqrt{2}}\left(\hat{\phi}^\dagger e^{i\omega t} + \hat{\phi}e^{-i\omega t}\right) \quad \hat{\psi} = \frac{i}{\sqrt{2}}\left(\hat{\phi}^\dagger e^{i\omega t} - \hat{\phi}e^{-i\omega t}\right)\end{aligned} \tag{3.17}$$

Unfortunately, we cannot simply substitute the above relationships into the Lagrangian because these are only correct to first order; we must expand around ρ_c and θ_c in each term, then do a Taylor expansion in the exponential.

The $\hat{\phi}$ operator is complex, yet is not charged under the $U(1)$ of the theory inside the Q-ball because $\hat{\phi} \to \hat{\phi}e^{i\alpha}$ is not a symmetry of the Lagrangian unless $\phi_c = 0$ (in which case we are outside the Q-ball). Neither of the $\hat{\rho}$ or $\hat{\psi}$ is charged either, so a charged current cannot exist in the interior unless it is via bulk motion of, or interaction with, the condensate field ϕ_c.

3.3.3 Calculation of the matrix element

We will now use the method of sections 3.3.1 and 3.3.2 in order to derive the matrix element for decay of several Q-ball quanta to phonons within the Q-ball (the Feynman diagram representation of which is given by figure 3.2). We consider the lifting potential

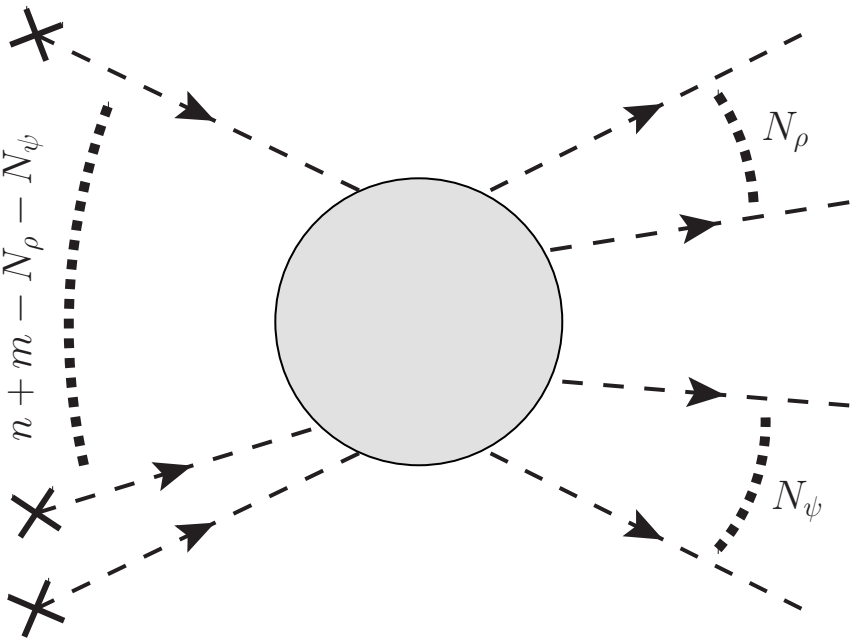

Figure 3.2: Feynman diagram representation of the matrix element responsible for decay of the Q-ball into phonons. External lines on the left marked by a cross are interactions of the operator with the condensate ϕ_c, whereas external lines on the right are the phonons produced from the decay. Arrows denote flow of momentum, not charge.

discussed earlier and expand it in polar form:

$$\begin{aligned}\mathcal{L}_{\text{lifting}} &= -\frac{g}{\Lambda^{n+m-4}}\phi^n(\phi^\dagger)^m + \text{c.c.} \\ &= -g_{nm}\left(\frac{\rho}{\sqrt{2}}\right)^{n+m} e^{i(n-m)\theta} + \text{c.c.}\end{aligned} \tag{3.18}$$

where $g_{nm} \equiv g/\Lambda^{n+m-4}$. We now expand around the Q-ball condensate in the way prescribed above, giving us

$$\mathcal{L}_{\text{lifting}} = -\frac{g_{nm}}{2^{(n+m)/2}}\sum_{j=0}^{n+m}\sum_{k=0}^{\infty}\binom{n+m}{j}\frac{i^k(n-m)^k}{k!}(\rho_c^{n+m-j-k}e^{i(n-m)\theta_c})\hat{\rho}^j\hat{\psi}^k + \text{c.c.} \tag{3.19}$$

Now we calculate the matrix element for the decay of the condensate to N_ρ ρ's and N_ψ ψ's:

$$\begin{aligned}\mathcal{M} &= \frac{i}{2^{(n+m)/2}} \sum_{j,k} \binom{n+m}{j} \frac{(n-m)^k}{k!} \int d^4x\, \rho_c^{n+m-j-k} \left[i^k g_{nm} e^{i(n-m)\omega t} + \text{c.c.} \right] \\ &\quad \times \left\langle 0 \left| \hat{\rho}^j \hat{\psi}^k \right| p_1, \cdots, p_{N_\rho}, k_1, \cdots, k_{N_\psi} \right\rangle \qquad (3.20) \\ &= \frac{2\pi i}{2^{(n+m)/2}} C^{nm}_{N_\rho N_\psi} \int \left(\prod_{q=q_1}^{q_D} \frac{d^3q}{(2\pi)^3} \rho_c(\boldsymbol{q}) \right) (2\pi)^3 \delta^3 \left(\boldsymbol{Q} - (\boldsymbol{P} + \boldsymbol{K}) \right) \\ &\quad \times \left[i^{N_\psi} g_{nm} \delta((n-m)\omega - (P^0 + K^0)) + (-i)^{N_\psi} g^*_{nm} \delta((m-n)\omega - (P^0 + K^0)) \right] \qquad (3.21)\end{aligned}$$

where $C^{nm}_{jk} \equiv j!\binom{n+m}{j}(n-m)^k$, $D \equiv n + m - N_\rho - N_\psi$ and $Q = \sum q$, $P = \sum p$, $K = \sum k$ are the sums of the various 4-momenta. We substitute in the Q-ball wave function to the Fourier transform $\rho_c(\boldsymbol{q}) = \sqrt{2}\phi_c(\boldsymbol{q}) = \sqrt{2}\pi^{3/2} R^3 \phi_0 e^{-q^2R^2/4}$:

$$\begin{aligned}\mathcal{M} &= \frac{i(2\pi)^{4-3D} 2^{D/2}}{2^{(n+m)/2}} C^{nm}_{N_\rho N_\psi} \left(\sqrt{2}\pi^{3/2} R^3 \phi_0 \right)^D \int \left(\prod_{q=q_1}^{q_D} d^3q\, e^{-\frac{R^2}{4}q^2} \right) \delta^3(\boldsymbol{Q} - (\boldsymbol{P} + \boldsymbol{K})) \\ &\quad \times \left[i^{N_\psi} g_{nm} \delta((n-m)\omega - (P^0 + K^0)) + (-i)^{N_\psi} g^*_{nm} \delta((m-n)\omega - (P^0 + K^0)) \right] \qquad (3.22)\end{aligned}$$

Now, we use an interesting geometric argument to solve this integral. Since $d^3q = dq_1\, dq_2\, dq_3$ and $q^2 = q_1^2 + q_2^2 + q_3^2$, we observe that (besides the delta functions), the integral is hyperspherically symmetric in the $3D$-dimensional q-space. The three delta functions each define a hyperplane in this space, the union of which is a $3(D-1)$-dimensional hypersurface which is a subspace of the larger $3D$-dimensional space. This hypersurface is displaced from the origin by the vector $\boldsymbol{v} = (\boldsymbol{P}+\boldsymbol{K})/\sqrt{D}$ (notice the hyperplane defined by $Q_i - (P_i + K_i) = 0$ has a unit normal vector of $\hat{n} = (1, 1, \cdots, 1)/\sqrt{D}$ and is displaced from the origin by a distance of $|P_i + K_i|/\sqrt{D}$). This integral therefore represents a spherically symmetric Gaussian integral over a $3(D-1)$-dimensional space offset from the origin by $\boldsymbol{v}$. We can therefore rotate our coordinate system so that $\boldsymbol{v}$ points in the new "$\hat{z}$" direction and transform to a type of "hypercylindrical coordinates": $(s, \phi, \theta_1, \cdots, \theta_{3(D-1)-2}, x, y, z)$ where the coordinates x, y, and z are Euclidean and a specification of $(x, y, z) = (0, 0, v)$ constrains one to the hypersurface. Then, we simply

perform the spherically symmetric integral over this surface:

$$\int \left(\prod_{q=q_1}^{q_D} d^3q\, e^{-\frac{R^2}{4}q^2} \right) \delta^3(\boldsymbol{Q} - (\boldsymbol{P} + \boldsymbol{K})) = \int d^{3(D-1)} s e^{-\frac{R^2}{4}(s^2+v^2)}$$
$$= \Omega_{3(D-1)-1} e^{-\frac{R^2}{4}v^2} \int_0^\infty ds\, s^{3(D-1)-1} e^{-\frac{R^2}{4}s^2} \tag{3.23}$$

where $\Omega_{n-1} = 2\pi^{n/2}/\Gamma(n/2)$ is the solid angle of the $(n-1)$-sphere, and the remaining integral can be written in terms of a gamma function as well (it actually cancels with the one from $\Omega_{3(D-1)-1}$). After the dust has settled, the matrix element is found to be

$$\mathcal{M} = 2i\pi^{5/2} 2^{(n+m)/2-N_\rho-N_\psi} C^{nm}_{N_\rho N_\psi} R^3 \phi_0^D e^{-\frac{R^2}{4D}(\boldsymbol{P}+\boldsymbol{K})^2}$$
$$\times \left[i^{N_\psi} g_{nm} \delta((n-m)\omega - (P^0 + K^0)) + (-i)^{N_\psi} g^*_{nm} \delta((m-n)\omega - (P^0 + K^0)) \right] \tag{3.24}$$

The number of Q-ball quanta that decay in each event (and thereby amount of charge violation) can be read off from the delta function, and is $\Delta Q = |n-m|$, as expected. One important note is that since $m_\rho \gg \omega$, the condensate cannot decay to ρ's unless $|n-m|\omega > m_\rho$, which requires the amount of charge violation to be very high. Decays to ψ's might appear to proceed unimpeded, however, because they are massless. However, these phonons pick up a small mass from two different sources. First, as mentioned before, because the phonons are confined to the Q-ball, they are essentially standing waves with a maximum (Compton) wavelength of $\lambda \approx 2R$, which implies a minimum rest energy $m_\psi = 1/k = 1/4\pi R$. Since in a thick-wall Q-ball $\omega R = \sqrt{3}$, we have $m_\psi = \omega/4\pi\sqrt{3} \approx \omega/22$, which is small, but still a significant fraction of ω! Second, the baryon-violating term itself introduces a small mass, which we can see by expanding to second order in $\hat{\psi}$:

$$\mathcal{L}_{\text{lifting}} \supset \frac{1}{2} \left[\frac{(n-m)^2 \rho_c^{n+m-2}}{2^{(n+m)/2-1}} \left(\text{Im}(g_{nm}) \sin((m-n)\omega t) - \text{Re}(g_{nm}) \cos((m-n)\omega t) \right) \right] \hat{\psi}^2 \tag{3.25}$$

where the quantity in square brackets can be identified with m_ψ^2. Not only is this mass small in magnitude compared with the first contribution, but it also has harmonic time dependence, and therefore averages out to zero over timescales longer than about $|n-m|/\omega$. Thus, it is safe to assume that the mass from the Compton wavelength is the only mass that contributes.

3.3.4 Calculation of the decay rate

We now apply equation 3.15 to calculate the decay rate, focusing on decays to only the Goldstone modes and setting $N_\rho = 0$ and $N \equiv N_\psi$. We take the squared amplitude (which can be simplified because the cross-terms are zero due to the conflicting delta functions), drop one of the delta functions, and integrate over the final state phase space:

$$\Gamma^N_{nm} = 4\pi^5 2^{n+m-2N} |g_{nm}|^2 (C^{nm}_{0N})^2 R^6 \phi_0^{2D} I_N \left(|(n-m)|\omega, R/\sqrt{2D}, m_\psi \right) \tag{3.26}$$

where

$$I_N(\Omega, a, m) = \int \left(\prod_{p=p_1}^{p_N} \frac{d^3p}{(2\pi)^3} \frac{1}{2\sqrt{p^2+m^2}} \right) e^{-a^2(\sum \boldsymbol{p})^2} \delta \left(\Omega - \sum \sqrt{p^2+m^2} \right) \tag{3.27}$$

For $N = 1$ we can get an exact answer:

$$I_1(\Omega, a, m) = \frac{1}{(2\pi)^2} e^{-a^2(\Omega^2-m^2)} \sqrt{\Omega^2-m^2} \Theta(\Omega - m) \tag{3.28}$$

However, using the relationships $m_\psi = \omega/4\pi\sqrt{3}$ and $R = \sqrt{3}/\omega$, we can reduce the integral to something even simpler:

$$\begin{aligned} &I_N(|n-m|\omega, R/\sqrt{2D}, m_\psi) \\ &\quad= \int \left(\prod_{p=p_1}^{p_N} \frac{d^3p}{(2\pi)^3} \frac{1}{2\sqrt{p^2+m_\psi^2}} \right) e^{-\frac{R^2}{2D}(\sum \boldsymbol{p})^2} \delta\left(|(n-m)\omega| - \sum \sqrt{p^2+m_\psi^2} \right) \\ &\quad= \omega^{2N-1} \int \left(\prod_{p=p_1}^{p_N} \frac{d^3(p/\omega)}{(2\pi)^3} \frac{1}{2\sqrt{(p/\omega)^2+(m_\psi/\omega)^2}} \right) e^{-\frac{24\pi^2}{D}(\sum(\boldsymbol{p}/\omega))^2} \\ &\qquad\times \delta\left(|n-m| - \sum \sqrt{(p/\omega)^2-(m_\psi/\omega)^2} \right) \end{aligned} \tag{3.29}$$

We then change coordinates to $\boldsymbol{\xi} \equiv \boldsymbol{p}/\omega$ and substitute the phonon mass so that $m_\psi/\omega \equiv \mu = 1/4\pi\sqrt{3}$:

$$= \omega^{2N-1} \left[\int \left(\prod_{\xi=\xi_1}^{\xi_N} \frac{d^3\xi}{(2\pi)^3} \frac{1}{2\sqrt{\xi^2+\mu^2}} \right) e^{-\frac{24\pi^2}{n+m-N}(\sum \boldsymbol{\xi})^2} \delta\left(|n-m| - \sum \sqrt{\xi^2+\mu^2} \right) \right] \tag{3.30}$$

where we will define the integral in square brackets as J^N_{nm} (note $J^N_{nm} = J^N_{mn}$ and $J = 0$ if $N \geq n+m$ or $n = m$). Because n, m, and N are integers and J is a dimensionless number, we can simply tabulate all its possible values using numerical integration such as Monte Carlo. However, because of the delta function, we can't do MC until we integrate that out. We convert to spherical coordinates and separate the Nth coordinate from the rest, then integrate over it to remove the delta function, leaving us with

$$\begin{aligned} J^N_{nm} = \frac{1}{(16\pi^3)^N} \prod_{\xi,\phi,\theta}{}' \left(\int_0^{2\pi} d\phi \int_0^{\pi} d\theta \, \sin\theta \int_0^{\infty} \frac{\xi^2}{\sqrt{\xi^2+\mu^2}} \right) \int_0^{2\pi} d\phi_N \int_0^{\pi} d\theta_N \, \sin\theta_N \xi_N(\{\xi\}) \\ \times e^{-\frac{24\pi^2}{n+m-N}\left(\sum_i' \xi_i^2 + \sum_{i\neq j}' \boldsymbol{\xi}_i \cdot \boldsymbol{\xi}_j + \xi_N^2(\{\xi\}) + 2\sum_i' \xi_N(\{\xi\})\xi_i(\sin\theta_N \sin\theta_i \cos(\phi_N - \phi_i) + \cos\theta_N \cos\theta_i) \right)} \end{aligned} \tag{3.31}$$

where the primed sums/products mean we sum/multiply over all coordinates except the Nth, and

$$\xi_N(\{\xi\}) \equiv \sqrt{\left(|n-m| - \sum{}' \sqrt{\xi^2+\mu^2}\right)^2 - \mu^2} \tag{3.32}$$

$$\boldsymbol{\xi}_i \cdot \boldsymbol{\xi}_j = \xi_i \xi_j \left(\sin\theta_i \sin\theta_j \cos(\phi_i - \phi_j) + \cos\theta_i \cos\theta_j\right) \tag{3.33}$$

Some sample values of J^N_{nm} (I'll restrict to $n+m>4$ and $|n-m|=1$ for now) are:

$N=1:$ $J^1_{23} = 5.5\times10^{-28}, J^1_{34} = 1.9\times10^{-19}, J^1_{45} = 3.8\times10^{-15}, J^1_{56} = 1.4\times10^{-12}, J^1_{67} = 7.1\times10^{-11}$

$N=2:$ $J^2_{23} = 1.\times10^{-7}, J^2_{34} = 3.\times10^{-7}, J^2_{45} = 5.\times10^{-7}, J^2_{56} = 8.\times10^{-7}, J^2_{67}1.2\times10^{-6}$

$N=3:$ $J^3_{23} = 2.\times10^{-11}, J^3_{34} = 5.\times10^{-10}, J^3_{45} = 1.\times10^{-9}, J^3_{56} = 2.\times10^{-9}, J^3_{67} = 7.\times10^{-9}$

$N=4:$ $J^4_{23} = 8.\times10^{-17}, J^4_{34} = 6.\times10^{-14}, J^4_{45} = 9.\times10^{-13}, J^4_{56} = 5.\times10^{-12}, J^4_{67} = 2.\times10^{-11}$

$N=5:$ $J^5_{34} = 3.\times10^{-19}, J^5_{45} = 7.\times10^{-17}, J^5_{56} = 3.\times10^{-15}, J^5_{67} = 2.\times10^{-14}$

Clearly, final states involving more phonons have a smaller amount of phase space volume. The exception is $N=1$, which gets extra suppression from the fact that any decay involving one final state particle does not conserve momentum. It should be noted that repeated evaluation of the Monte Carlo shows that the uncertainty in these answers is quite large; variation in the first digit is common, though the order of magnitude remains consistent over repeated evaluations. It turns out that this is not terribly important for computing the neutron star lifetimes; variations of $O(1)$ in J translate to variations of $O(10^{-3})$ in the lifetimes. This is because the dependence of Γ on Q is most important. There is also a small imaginary part attached to some of these numbers which is not shown. This is from integrating over a region in phase space which is not kinematically allowed, and it does not contribute to the decay rate, so we can simply ignore it.

If the dimension of the lifting potential is extremely high ($n+m \to \infty$), then the exponential in the integrand becomes order unity, and we can reduce this even further by transforming to a dimensionless energy coordinate $\sigma = \sqrt{\xi^2+\mu^2}$ and integrating out all the

angles. The integral J^N_{nm} approaches

$$J^N_{nm} \to \frac{1}{(2\pi)^{2N}} \left(\prod_{\sigma=\sigma_1}^{\sigma_N} \int_{\mu}^{|n-m|-(N-1)\mu} d\sigma \, \sqrt{\sigma^2 - \mu^2} \right) \delta \left(|n-m| - \sum \sigma \right) \tag{3.34}$$

This can be calculated via Monte Carlo in a similar manner to equation 3.31. Note that in this limit J^N_{nm} only depends on $\Delta Q = |n-m|$ and N. Now, putting all of this together, we can express the decay rate to N Goldstone bosons as

$$\Gamma^N_{nm} = 4\pi^5 2^{n+m-2N} |g_{nm}|^2 (N!)^2 (c^{nm}_{0N})^2 R^6 \phi_0^{2D} \omega^{2N-1} J^N_{nm} \tag{3.35}$$

Writing out R, ϕ_0 and ω in terms of Q (see equations 3.8) and lumping all the non-dimensional constants together,

$$\Gamma^N_{nm} = |g|^2 K^N_{nm} Q^{\frac{1}{4}(7+2(n+m-2N))} M \left(\frac{M}{\Lambda} \right)^{2(n+m)-8} \tag{3.36}$$

$$K^N_{nm} \equiv 2^{\frac{1}{2}(5(n+m-N)-3)} 3^{\frac{3}{8}(1-2(n+m-2N))} \pi^{\frac{13}{4}-(n+m-3N/2)} (n-m)^{2N} J^N_{nm} \tag{3.37}$$

where M is the mass scale associated with the potential energy density in the flat direction of the scalar potential ($V_0 = M^4$). We can now simply tabulate the K^N_{nm} and have a semi-analytic expression for the decay rate that will be easy to use in the analysis of section 3.5.

3.4 Interactions between Q-balls and neutron stars

We would now like to understand how a Q-ball interacts with its host star in order to determine the neutron consumption rate. As discussed in the work of one of us, Loveridge, and Shaposhnikov (KLS) [133], the transport mechanism of neutrons inside a neutron star is complicated and is not very well understood. The authors outline two different possible situations for neutron accretion, which we will summarize here for clarity.

3.4.1 Surface conversion of neutron flux

As a rough estimate, KLS assume the rate of neutron absorption is simply equal to the flux of neutrons moving across the surface of the Q-ball. In this scenario, the growth rate of the Q-ball is given by

$$\begin{aligned}\dot{Q} &= b^{-1} 4\pi R^2 n_0 v = \frac{4 \cdot 3^{5/4} n_0}{M^2 (4\pi)^{1/2}} Q^{1/2} \\ &\approx (2 \times 10^{-8} \text{ GeV}) Q^{1/2}\end{aligned} \tag{3.38}$$

where $b = 1/3$ is the baryon number of a squark, $n_0 \approx 10^{15}$ g/cm^3 $= 4 \times 10^{-3}$ GeV^3 is the neutron number density at the center of the star, and $v \approx 1$ is the speed of the neutrons, assumed to be of the order of the speed of light. This estimate for the absorption rate is likely too high, as it does not take into account the pressure backreaction from the pions and antineutrons produced on the surface of the Q-ball.

3.4.2 Hydrodynamic considerations due to pion production

Using a couple different methods, KLS determine the pressure at the center of the star in hydrostatic equilibrium is approximately $P \approx (0.1 \text{ GeV})^4$. For light degrees of freedom such as pions, electrons and neutrinos, this implies a temperature of about 100 MeV from the relation $P \approx gT^4/\pi^2$. This temperature cannot be maintained by thermal effects alone, but can be maintained by the pions produced on the surface of the Q-ball. The rate of pion loss to decay inside the star is given by

$$\dot{N}_\pi \approx 2\pi^{3/2} \sqrt{\frac{\lambda}{3\tau}} n_\pi(0) R^2 \tag{3.39}$$

where $\lambda \approx n_0^{-1/3}$ and $\tau \approx 10^8$ GeV^{-1} are the mean free path and neutral pion lifetime, respectively. They also assume $n_\pi(0) \approx n_0$ in order to maintain pressure. Each neutron only has enough mass and energy to supply about 4-5 pions, so the rate of neutron absorption is

about that much lower, giving us

$$\dot{Q} = \frac{10\pi^{3/2} n_0^{5/6} R^2}{b\sqrt{3\tau}} = \frac{5\pi n_0^{5/6}}{3^{1/4} b M^2 \tau^{1/2}}$$
$$\approx (10^{-11}\ \text{GeV}) Q^{1/2} \tag{3.40}$$

This estimate is slightly lower than the raw neutron flux estimate and is a little more realistic.

3.5 Baryon number evolution in an infected neutron star

Now that have expressions for both the growth rate and decay rate of the Q-ball, we can set up a simple set of differential equations to model the evolution of the baryon number in both the Q-ball and the neutron star:

$$\dot{B}_Q = b\dot{Q} = -\dot{N}_n - b\,|n-m|\,\Gamma_{nm} \tag{3.41}$$

$$\dot{B}_{\text{NS}} = \dot{N}_n = -(10^{-11}\ \text{GeV}) Q^{1/2} \tag{3.42}$$

where $\Gamma_{nm} \equiv \sum_N \Gamma^N_{nm}$. Or, eliminating N_n and assuming decays are dominated by a specific N (usually either 1 or 2), we can put it in a more aesthetically pleasing form:

$$\dot{Q} \approx 3\dot{N}_0 Q^{1/2} - \Gamma_0 Q^\alpha \tag{3.43}$$

where $\dot{N}_0 = 10^{-11}$ GeV, $\Gamma_0 = |g|^2 K^N_{nm} M (M/\Lambda)^{2(n+m)-8}$, and $\alpha = \frac{1}{4}(7 + 2(n+m-2N))$ ($\alpha > 1$ unless N is some ridiculously high number, which is unlikely). The initial conditions for this system are $Q(0) = Q_0 \approx 10^{25}$ and $N_n(0) = B_{\text{NS}} = 10^{57}$, and the total number of neutrons absorbed by the Q-ball is given by integrating equation 3.42:

$$\Delta N_n(t) = -\int_0^t dt'\, \dot{N}_0 Q^{1/2} \tag{3.44}$$

We can see that equation 3.43 has late-time attractor solutions, whereby setting $\dot{Q} = 0$, we solve for the equilibrium charge: $Q_{\text{eq}} = (3\dot{N}_0/\Gamma_0)^{\frac{1}{\alpha - 1/2}}$ (see figure 3.3). If this charge is

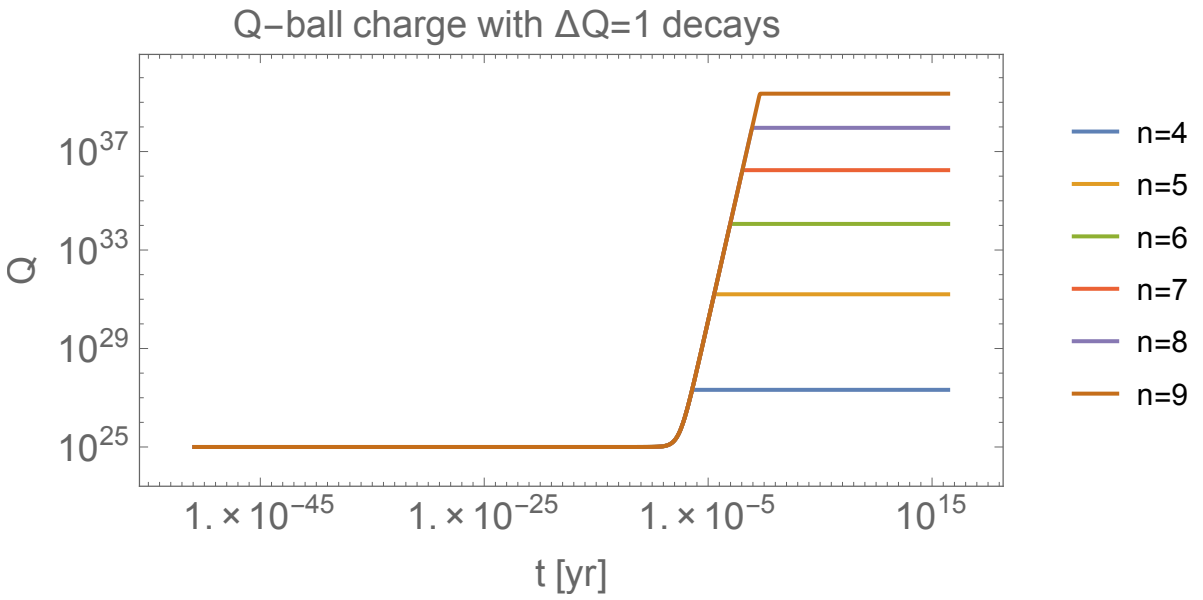

Figure 3.3: Plot of the evolution of charge within the Q-ball at the center of a neutron star with decay channels attributed to various $\Delta Q = 1$ operators, indexed by $(n, m) = (n, n+1)$. The Q-ball very quickly equilibrates so that the rate of decay is equal to the rate of neutron consumption. Not shown are the contours for $n = 2$ and $n = 3$, which are ruled out because the corresponding operators would destabilize the Q-ball in free space on short timescales.

reached relatively quickly compared to the total lifetime of the neutron star, then equation 3.44 implies that the neutron depletion is linear in time, and the lifetime of the star is then

$$\tau_{\rm NS} \approx \frac{B_{\rm NS}}{\dot{N}_0} \left(\frac{3\dot{N}_0}{\Gamma_0} \right)^{\frac{1/2}{1/2-\alpha}} \tag{3.45}$$

In free space, the evolution of the charge of a Q-ball is given by equation 3.43 with $\dot{N}_0 = 0$, which can easily be solved for:

$$Q(t) \approx \left[(\alpha - 1) \left(\frac{Q_0^{1-\alpha}}{\alpha - 1} + \Gamma_0 t \right) \right]^{\frac{1}{1-\alpha}} \tag{3.46}$$

The Q-ball lifetime can then be solved for by setting $Q(\tau_Q) = 1$, which gives us

$$\tau_Q \approx \frac{1 - Q_0^{1-\alpha}}{(\alpha - 1)\Gamma_0} \tag{3.47}$$

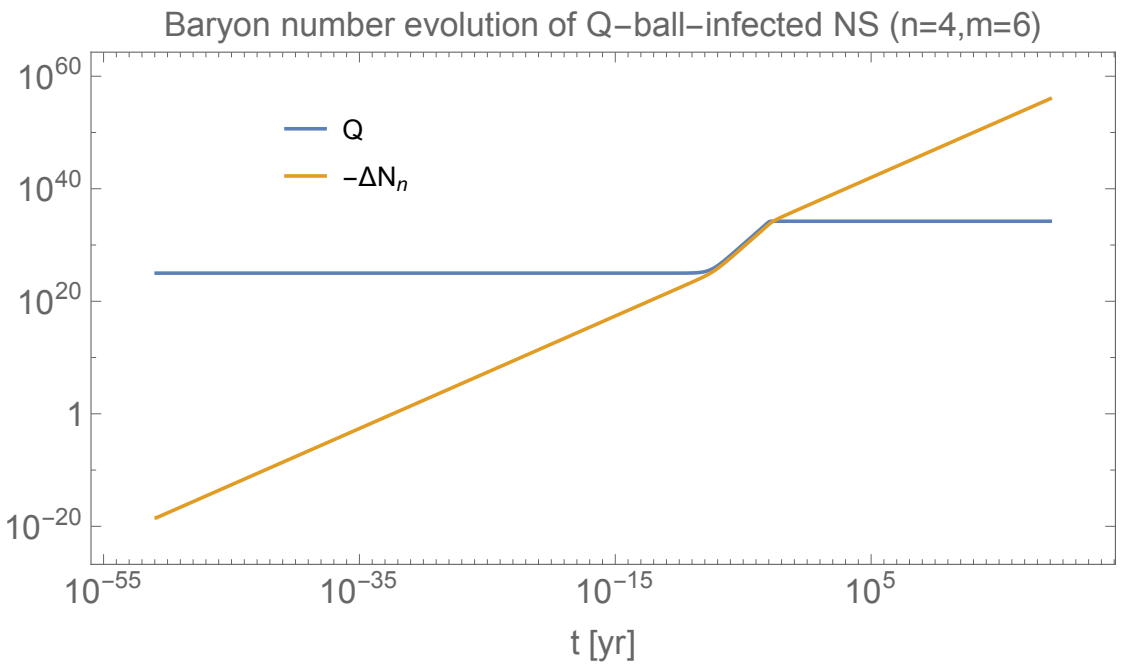

Figure 3.4: Plot of the charge Q contained within a Q-ball and the number of neutrons consumed by the Q-ball over the life of the neutron star. Once $-\Delta N_n = B_{\rm NS} = 10^{57}$, integration is stopped and the star is gone. This specific example is for a Q-ball with decays mediated by a $(n, m) = (4, 6)$ operator, resulting in a neutron star lifetime of $\tau_{\rm NS} = 1 \times 10^{20}$ years.

If we want to be more exact and take into account decays from all channels (not just the dominant one), we can numerically solve for $\tau_{\rm NS}$ and τ_Q by evolving equations 3.41 and 3.42 until $N_n = 0$ or $Q = 1$, at which point either the neutron star has been consumed or the Q-ball has decayed, and we stop integration (a specific example is given in figure 3.4). This is how we will derive the limits in the next section.

3.6 Limits on baryon-violating (and conserving) operators

Using equations 3.41 and 3.42 and the algorithm prescribed in the previous section, we can tabulate the lifetimes of infected neutron stars and free Q-balls endowed with the lifting potential of equation 3.1, indexed by the integers n and m. We will find that baryon-violating terms are necessary if an infected neutron star is to survive to present day.

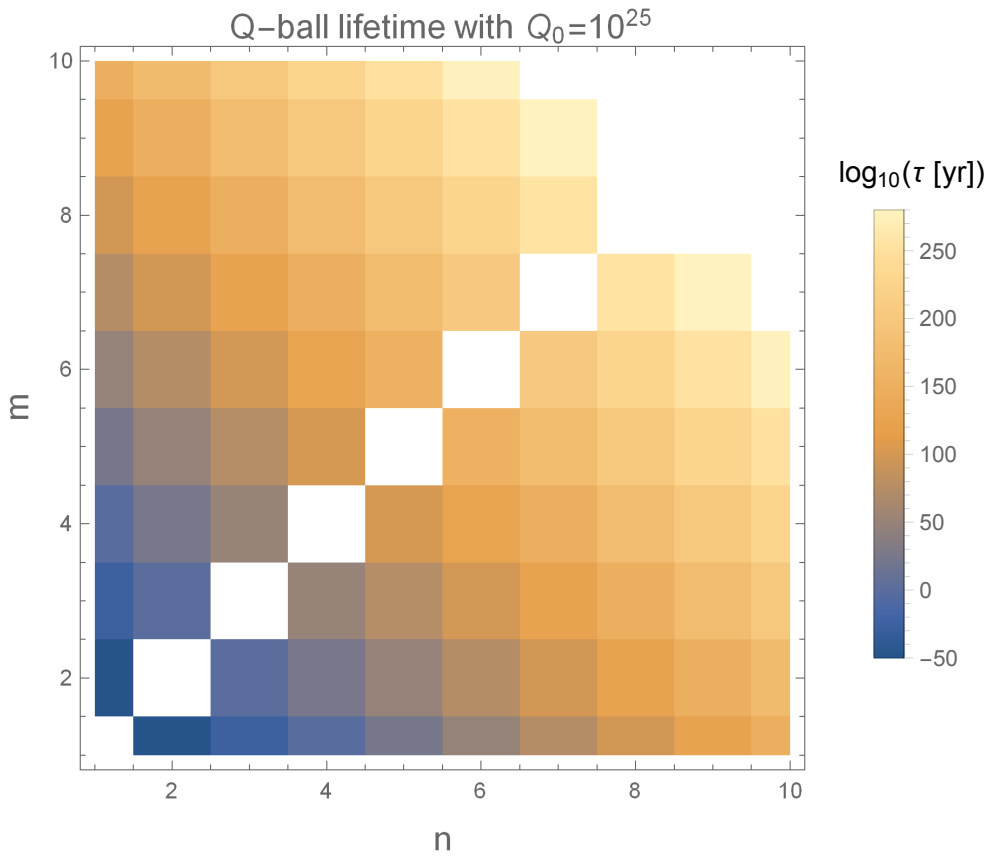

Figure 3.5: Plot of Q-ball lifetimes with an initial charge of $Q_0 = 10^{25}$ as a function of various n, m corresponding to the terms in the lifting potential. The diagonal $n = m$ is actually completely stable because decays are not permitted due to restoration of the $U(1)_B$ symmetry.

3.6.1 From decay of Q-balls in free space

We solve the baryon number evolution equations with $\dot{N}_0 = 0$ in order to model the decay of the Q-ball in free space. The results are plotted in figure 3.5 and tabulated in table 3.1 in the appendix. The most striking feature is that for $n = m$, the Q-ball is completely stable because the Goldstone field does not appear in the potential. We can also see that in general, as the dimension of the operator increases, so does the lifetime of the Q-ball. In fact, all Q-balls with lifting potentials of dimension 5 or less are unstable and decay in a matter of hours or less, whereas those with dimension greater than 5 are stable on timescales much longer than the age of the Universe. This immediately rules out dark matter Q-balls with $n + m \leq 5$. In the high-dimension limit ($n + m \to \infty$), we can calculate J^N_{nm} using

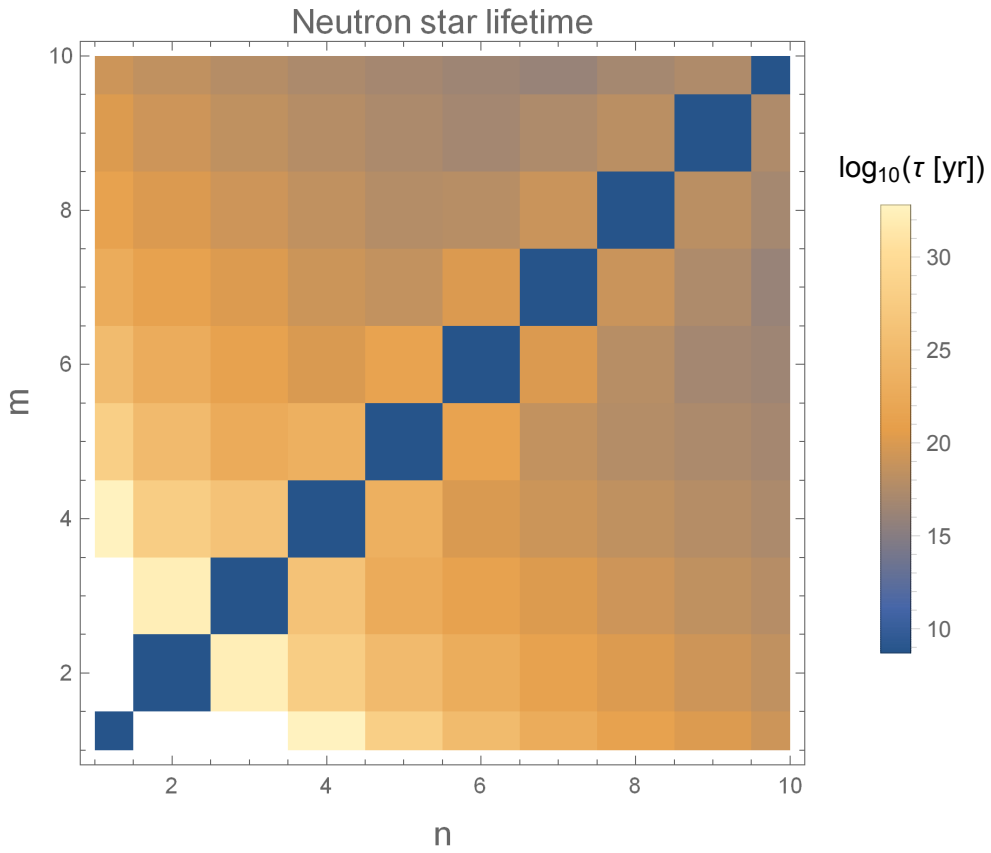

Figure 3.6: Plot of neutron star lifetimes after being infected by a Q-ball with initial charge $Q_0 = 10^{25}$ as a function of various n, m corresponding to the terms in the lifting potential. The diagonal $n = m$ is ruled out because the B-violating decays are forbidden, and the stability of the Q-ball causes it to grow without bound, quickly consuming the star.

equation 3.31 and solve the baryon evolution equations again, though this doesn't lead to any interesting revelations; the Q-ball lifetime continues to increase as the dimension of the operator increases, and is pretty much independent of ΔQ. The largest lifetime calculated (dim $= 100$) was over 10^{2000} years!

3.6.2 From lifetime of neutron stars

Solving the baryon number evolution equation with $\dot{N}_0 \neq 0$ and integrating until $N_n = 0$ gives us the lifetime of an infected neutron star. This information is plotted in figure 3.6 and table 3.2. As we can see, the diagonal where $n = m$ is ruled out, with a lifetime of about 10^8 years. This is due to the fact that the Q-ball is absolutely stable in this regime, and therefore

grows without bound as it eats away at the neutron star, quickly consuming it. In fact, this is an upper limit on the lifetime; the final charge of the Q-ball in this situation is 3×10^{57}, which is beyond the critical charge for a flat direction Q-ball to change into a curved direction type, which as mentioned before, has an even higher rate of neutron consumption. The highest charge for a Q-ball with baryon-violating decays is only 10^{42}, well below the critical charge. Interestingly, in the regions with operator dimension ≤ 4, the Q-ball decays so quickly that it breaks down completely before the neutron star is consumed. As mentioned in the previous subsection, Q-balls in this regime aren't stable in free space anyway. We can see that as we move away from the $n = m$ diagonal (increasing ΔQ), the lifetime of the star begins to drop, then levels out, with the magnitude of the drop decreasing as the operator dimension increases. In order to study the effects of very high-dimension operators ($n + m \to \infty$), we once again use equation 3.31 to calculate J^N_{nm} and solve the baryon number evolution equations. This is plotted in figure 3.7. What we find is quite interesting: the lifetime appears to approach a limiting value around 10^{12} years as the operator dimension increases. The lifetime is roughly independent of ΔQ, though it does drop slightly near $\Delta Q = 0$. This appears to match the trend of figure 3.6 as the operator dimension is increased.

3.7 Conclusion

We have shown here that Q-balls can make up dark matter if baryon-violating terms of dimension $n + m > 5$ are present in the scalar potential. Cases in which there is no baryon violation ($n = m$) are ruled out as well due to unrestricted Q-ball growth. The baryon number violation is also necessary for the Affleck-Dine mechanism to work. This eliminates the neutron star bounds. Beyond this, there appears to be no restriction on these operators, even at very high dimension. The low level of baryon number violation does not affect the experimental limits based on IceCube [130], Super-Kamiokande [140] and other direct detection experiments. However, one should keep in mind that Q-balls may carry some electric charge [125, 140, 141], making them almost invisible to most direct-detection searches. (A positively charged Q-ball cannot destabilize nuclei because the Coulomb repulsion prevents

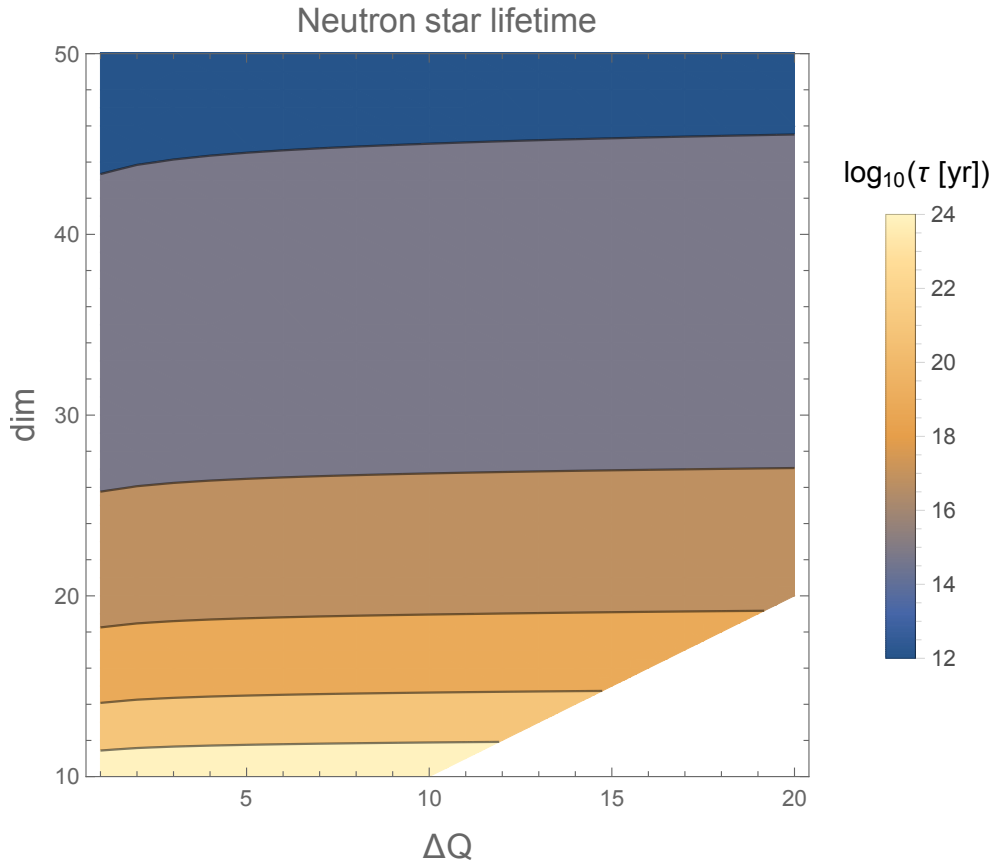

Figure 3.7: Plot of neutron star lifetimes after being infected by a Q-ball with initial charge $Q_0 = 10^{25}$ as a function of the charge violation per decay $\Delta Q > 0$ and the dimension of the operator in the lifting potential. The white region in the lower right corner is where $\Delta Q >$ dim, which is not allowed since it implies one of either n or m is negative.

any strong interactions between non-relativistic Q-balls and matter nuclei.) This leaves a wide range of parameters available for dark matter in the form of supersymmetric Q-balls.

3.8 Acknowledgements

This work was supported by the U.S. Department of Energy Grant No. DE-SC0009937. A.K. was also supported by the World Premier International Research Center Initiative (WPI), MEXT, Japan. A.K. appreciates the hospitality of the Aspen Center for Physics, which is supported by National Science Foundation grant PHY-1066293.

3.9 Appendix: Tables of Q-ball and neutron star lifetimes

These tables correspond to figures 3.5 and 3.6, and list the lifetimes of Q-balls and neutron stars infected by Q-balls with baryon-violating decays.

$n\backslash m$	1	2	3	4	5	6	7	8	9	10
1	∞	$7{\cdot}10^{-55}$	$9{\cdot}10^{-31}$	$6{\cdot}10^{-6}$	$1{\cdot}10^{20}$	$4{\cdot}10^{45}$	$7{\cdot}10^{71}$	$1{\cdot}10^{97}$	$2{\cdot}10^{123}$	$2{\cdot}10^{149}$
2	$7{\cdot}10^{-55}$	∞	$4{\cdot}10^{-4}$	$1{\cdot}10^{21}$	$1{\cdot}10^{46}$	$3{\cdot}10^{71}$	$1{\cdot}10^{97}$	$2{\cdot}10^{123}$	$7{\cdot}10^{148}$	$6{\cdot}10^{174}$
3	$9{\cdot}10^{-31}$	$4{\cdot}10^{-4}$	∞	$1{\cdot}10^{48}$	$5{\cdot}10^{72}$	$6{\cdot}10^{97}$	$1{\cdot}10^{123}$	$8{\cdot}10^{148}$	$1{\cdot}10^{175}$	$4{\cdot}10^{200}$
4	$6{\cdot}10^{-6}$	$1{\cdot}10^{21}$	$1{\cdot}10^{48}$	∞	$9{\cdot}10^{99}$	$3{\cdot}10^{124}$	$4{\cdot}10^{149}$	$1{\cdot}10^{175}$	$5{\cdot}10^{200}$	$9{\cdot}10^{226}$
5	$1{\cdot}10^{20}$	$1{\cdot}10^{46}$	$5{\cdot}10^{72}$	$9{\cdot}10^{99}$	∞	$7{\cdot}10^{151}$	$3{\cdot}10^{176}$	$4{\cdot}10^{201}$	$1{\cdot}10^{227}$	$4{\cdot}10^{252}$
6	$4{\cdot}10^{45}$	$3{\cdot}10^{71}$	$6{\cdot}10^{97}$	$3{\cdot}10^{124}$	$7{\cdot}10^{151}$	∞	$7{\cdot}10^{203}$	$3{\cdot}10^{228}$	$4{\cdot}10^{253}$	$9{\cdot}10^{278}$
7	$7{\cdot}10^{71}$	$1{\cdot}10^{97}$	$1{\cdot}10^{123}$	$4{\cdot}10^{149}$	$3{\cdot}10^{176}$	$7{\cdot}10^{203}$	∞	$7{\cdot}10^{255}$	$3{\cdot}10^{280}$	$> 10^{300}$
8	$1{\cdot}10^{97}$	$2{\cdot}10^{123}$	$8{\cdot}10^{148}$	$1{\cdot}10^{175}$	$4{\cdot}10^{201}$	$3{\cdot}10^{228}$	$7{\cdot}10^{255}$	∞	$> 10^{300}$	$> 10^{300}$
9	$2{\cdot}10^{123}$	$7{\cdot}10^{148}$	$1{\cdot}10^{175}$	$5{\cdot}10^{200}$	$1{\cdot}10^{227}$	$4{\cdot}10^{253}$	$3{\cdot}10^{280}$	$> 10^{300}$	∞	$> 10^{300}$
10	$2{\cdot}10^{149}$	$6{\cdot}10^{174}$	$4{\cdot}10^{200}$	$9{\cdot}10^{226}$	$4{\cdot}10^{252}$	$9{\cdot}10^{278}$	$> 10^{300}$	$> 10^{300}$	$> 10^{300}$	∞

Table 3.1: Table of Q-ball lifetimes (in years) for various lifting potentials. Lifetimes with an ∞ are absolutely stable due to restoration of the $U(1)_B$ symmetry.

$n\backslash m$	1	2	3	4	5	6	7	8	9	10
1	$5{\cdot}10^{8}$	∞	∞	$6{\cdot}10^{32}$	$1{\cdot}10^{28}$	$1{\cdot}10^{25}$	$7{\cdot}10^{22}$	$2{\cdot}10^{21}$	$1{\cdot}10^{20}$	$2{\cdot}10^{19}$
2	∞	$5{\cdot}10^{8}$	$2{\cdot}10^{32}$	$7{\cdot}10^{27}$	$9{\cdot}10^{24}$	$8{\cdot}10^{22}$	$2{\cdot}10^{21}$	$1{\cdot}10^{20}$	$2{\cdot}10^{19}$	$3{\cdot}10^{18}$
3	∞	$2{\cdot}10^{32}$	$5{\cdot}10^{8}$	$2{\cdot}10^{26}$	$5{\cdot}10^{22}$	$2{\cdot}10^{21}$	$1{\cdot}10^{20}$	$2{\cdot}10^{19}$	$3{\cdot}10^{18}$	$7{\cdot}10^{17}$
4	$6{\cdot}10^{32}$	$7{\cdot}10^{27}$	$2{\cdot}10^{26}$	$5{\cdot}10^{8}$	$3{\cdot}10^{23}$	$1{\cdot}10^{20}$	$1{\cdot}10^{19}$	$3{\cdot}10^{18}$	$7{\cdot}10^{17}$	$2{\cdot}10^{17}$
5	$1{\cdot}10^{28}$	$9{\cdot}10^{24}$	$5{\cdot}10^{22}$	$3{\cdot}10^{23}$	$5{\cdot}10^{8}$	$3{\cdot}10^{21}$	$4{\cdot}10^{18}$	$6{\cdot}10^{17}$	$2{\cdot}10^{17}$	$7{\cdot}10^{16}$
6	$1{\cdot}10^{25}$	$8{\cdot}10^{22}$	$2{\cdot}10^{21}$	$1{\cdot}10^{20}$	$3{\cdot}10^{21}$	$5{\cdot}10^{8}$	$1{\cdot}10^{20}$	$9{\cdot}10^{17}$	$6{\cdot}10^{16}$	$3{\cdot}10^{16}$
7	$7{\cdot}10^{22}$	$2{\cdot}10^{21}$	$1{\cdot}10^{20}$	$1{\cdot}10^{19}$	$4{\cdot}10^{18}$	$1{\cdot}10^{20}$	$5{\cdot}10^{8}$	$1{\cdot}10^{19}$	$2{\cdot}10^{17}$	$1{\cdot}10^{16}$
8	$2{\cdot}10^{21}$	$1{\cdot}10^{20}$	$2{\cdot}10^{19}$	$3{\cdot}10^{18}$	$6{\cdot}10^{17}$	$9{\cdot}10^{17}$	$1{\cdot}10^{19}$	$5{\cdot}10^{8}$	$1{\cdot}10^{18}$	$7{\cdot}10^{16}$
9	$1{\cdot}10^{20}$	$2{\cdot}10^{19}$	$3{\cdot}10^{18}$	$7{\cdot}10^{17}$	$2{\cdot}10^{17}$	$6{\cdot}10^{16}$	$2{\cdot}10^{17}$	$1{\cdot}10^{18}$	$5{\cdot}10^{8}$	$3{\cdot}10^{17}$
10	$1{\cdot}10^{19}$	$3{\cdot}10^{18}$	$7{\cdot}10^{17}$	$2{\cdot}10^{17}$	$7{\cdot}10^{16}$	$3{\cdot}10^{16}$	$1{\cdot}10^{16}$	$7{\cdot}10^{16}$	$3{\cdot}10^{17}$	$5{\cdot}10^{8}$

Table 3.2: Table of infected neutron star lifetimes (in years) for various lifting potentials. Lifetimes with an ∞ are absolutely stable.

CHAPTER 4

Primordial Black Holes from Q-ball Clustering

The content of this chapter has been published in Physical Review D as *Primordial black holes from scalar field evolution in the early universe*, E. Cotner, A. Kusenko, Phys. Rev. D, no. 10, 103002 (2017) [142].

Scalar condensates with large expectation values can form in the early universe, for example, in theories with supersymmetry. The condensate can undergo fragmentation into Q-balls before decaying. If the Q-balls dominate the energy density for some period of time, statistical fluctuations in their number density can lead to formation of primordial black holes (PBH). In the case of supersymmetry the mass range is limited from above by 10^{23}g. For a general charged scalar field, this robust mechanism can generate black holes over a much broader mass range, including the black holes with masses of 1–100 solar masses, which is relevant for LIGO observations of gravitational waves. Topological defects can lead to formation of PBH in a similar fashion.

4.1 Introduction

It is well established that stellar core collapse can lead to formation of black holes. However, it remains an open question whether some processes in the early universe could produce primordial black holes (PBH) [143, 82, 83, 144, 145, 146, 147, 148, 149, 150, 151, 152, 153, 154]. PBHs can account for all or part of dark matter [143, 82, 83, 144, 145, 146, 148, 149, 150, 151, 152, 153, 154]. Furthermore, they could be responsible for some of the gravitational wave signals observed by LIGO [155, 156, 157], In addition, PBHs can invade and destroy neutron stars, ejecting neutron rich material in the process, which can account

for for all or part of the r-process nucleosynthesis, as well as the 511-keV line in the galactic center [87]. Finally, PBHs could provide seeds for supermassive black holes [147]. A number of scenarios for black hole formation have been considered [145], and many of them rely on a spectrum of primordial density perturbations that has some additional power on certain length scales, which can be accomplished by means of tuning an inflaton potential.

It was recently pointed out that PBHs can form in a very generic scenario, which does not require any particular spectrum of density perturbations from inflation [158]. Scalar fields with slowly growing potentials form a coherent condensate at the end of inflation [159, 160, 161, 162]. In general, the condensate is not stable, and it breaks up in lumps, which evolve into Q-balls [31]. The gas of Q-balls contains a relatively low number of lumps per horizon, and the mass contained in these lumps fluctuates significantly from place to place. This creates relatively large fluctuations of mass density in Q-balls across both subhorizon and superhorizon distances. Since the energy density of a gas of Q-balls redshifts as mass, it can come to dominate the energy density temporarily, until the Q-balls decay, returning the universe to a radiation dominated era. The growth of structure during the Q-ball dominated phase can lead to copious production of primordial black holes. In this paper we will investigate this scenario in further detail.

Formation of Q-balls requires nothing more than some scalar field with a relatively flat potential at the end of inflation. For example, supersymmetric theories predict the existence of scalar fields with flat potentials. PBH formation in supersymmetric theories is, therefore, likely, even if the scale of supersymmetry breaking exceeds the reach of existing colliders.

A similar process can occur with topological defects, which can also lead to relatively large inhomogeneities. The discussion of topological defects is complicated by their non-trivial evolution. We will focus primarily on Q-balls, and will briefly comment on topological defects.

The format of this paper is as follows: in Section 4.2, we describe the fragmentation of the condensate and the production of Q-balls, then in Section 4.3 we derive the formalism for calculating the statistical moments of collections of Q-balls. In Section 4.4 we use the

results of the previous Section to calculate the expected PBH density and mass spectrum, and in Section 4.5 we account for the effects on cosmological thermal history and evolve the PBH distribution to the present day. In Section 4.6, we then compare our results with current observational constraints, and in Section 4.7 explore the available parameter space. In Section 4.8, we comment on the applicability of this mechanism to topological defects.

4.2 Formation of Q-balls

Formation of a scalar condensate after inflation and its fragmentation [31] is a fairly generic phenomenon. While supersymmetry is a well-motivated theory for scalar fields carrying global charges and having flat potentials [161, 124], our discussion can be easily generalized to an arbitrary scalar field with a global U(1) symmetry in the potential. Supersymmetric potentials generically contain flat directions that are lifted only by supersymmetry breaking terms. Some of the scalar fields that parameterize the flat directions carry a conserved U(1) quantum number, such as the baryon or lepton number. During inflation, these field develop a large vacuum expectation value (VEV) [159, 160, 161, 162], leading to a large, nonzero global charge density. When inflation is over, the scalar condensate $\phi(t) = \phi_0(t)\exp\{i\theta(t)\}$ relaxes to the minimum of the potential by a coherent classical motion with $\dot{\theta} \neq 0$ due to the initial conditions and possible CP violation at a high scale.

The initially homogeneous condensate is unstable with respect to fragmentation into non-topological solitons, Q-balls [64]. Q-balls exist in the spectrum of every supersymmetric generalization of the Standard Model [29, 163], and they can be stable or long-lived along a flat direction [31, 123]. In the case of a relatively large charge density (which is necessary for Affleck-Dine baryogenesis [161, 124]), the stability of Q-balls can be analyzed analytically [31, 126, 136]; these results agree well with numerical simulations [127]. One finds that the almost homogeneous condensate develops an instability with wavenumbers in the range $0 < k < k_{\rm max}$, where $k_{\rm max} = \sqrt{\omega^2 - V''(\phi_0)}$, and $\omega = \dot{\theta}$. The fastest growing modes of instability have a wavelength $\sim 10^{-2\pm1}$ of the horizon size at the time of fragmentation, and they create isolated lumps of condensate which evolve into Q-balls. Numerical simulations

[127, 164] indicate that most of the condensate ends up in lumps. However, since the mass of Q-balls is a non-linear function of the Q-ball size, Q-ball formation, in general, leads to a non-uniform distribution of energy density in the matter component represented by the scalar condensate. Q-balls can also form when the charge density is small or zero, in which case both positively and negatively charged Q-balls are produced [127]; here we do not consider this possibility.

Depending on the potential, the Q-balls with a global charge Q have the following properties [123, 31, 133, 121]:

$$\omega \sim \Lambda Q^{\alpha-1}, \qquad R \sim |Q|^{\beta}/\Lambda, \tag{4.1}$$

$$\phi_0 \sim \Lambda |Q|^{1-\alpha}, \qquad M \sim \Lambda |Q|^{\alpha}, \tag{4.2}$$

where Λ is the energy scale associated with the scalar potential, Q is the global U(1) charge and $0 < \alpha < 1$, $0 < \beta < 1$ denotes which type of Q-ball is under consideration (and also depends on the form of the scalar potential). For "flat direction" (FD) Q-balls, $\alpha = 3/4$ ($\beta = 1/4$), and for "curved direction" (CD) Q-balls, $\alpha = 1$ ($\beta = 1/3$) [123, 31].

4.3 Q-ball charge/mass distributions

Numerical simulations of condensate fragmentation and Q-ball formation have been performed in the past, from which we are able to determine the resulting charge and mass distributions [165, 164]. These distributions appear to be very sensitive to initial conditions in the condensate, such as the ratio of energy to charge density ($x = \rho/mq$), and to the details of the scalar potential. In addition, the resultant charge distribution can be very non-Gaussian due to the high degree of nonlinearity and chaos in the fragmentation process.

It should be understood that the results of these simulations are statistical in nature: a large number of Q-balls are created within the simulation volume so that the charge distribution tends towards a statistical average. In reality, if one were to perform a large simulation and look at the charge distributions in a number of small sub-volumes, you will

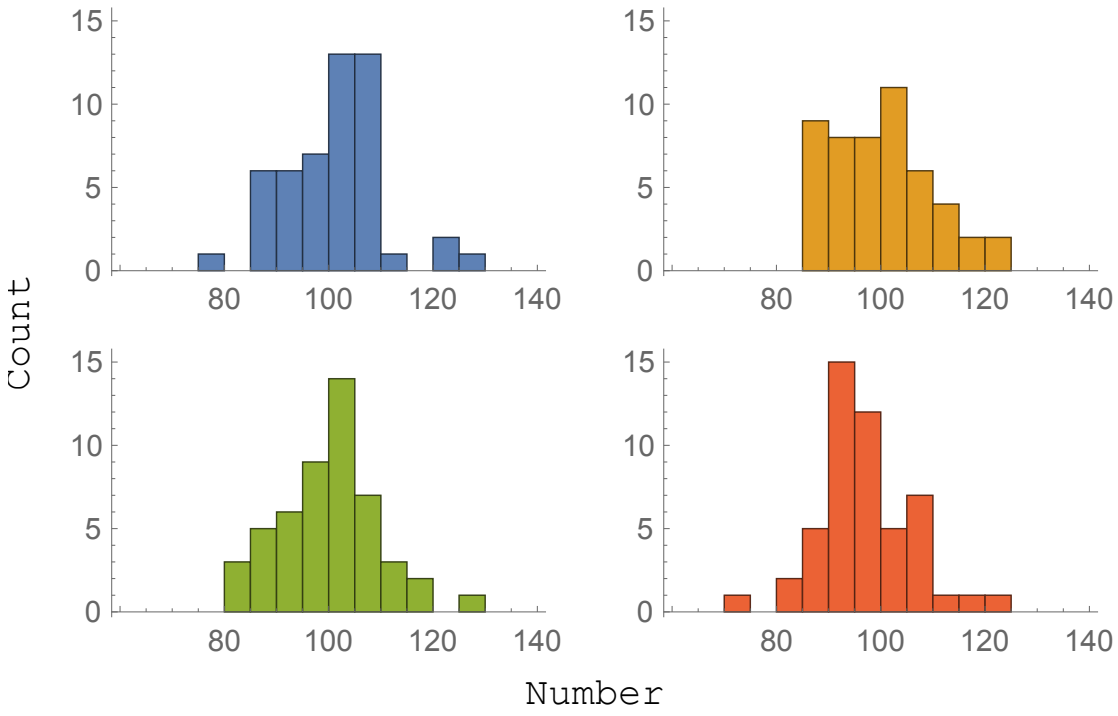

Figure 4.1: Schematic illustration of 4 histograms each containing 100 samples from the same Poisson distribution ($\lambda = 100$). The differences due to fluctuations are clearly visible.

find a large degree of variation, with more variation on smaller scales due to small sample sizes (this is not to say that the *variance* will be larger, just that the differences between distributions are large), as can be seen in Fig. 4.1. It is these large fluctuations relative to the mean that will be the source of density perturbations.

Once the resultant charge distribution of Q-balls $f_Q(Q)\,dQ$ has been calculated from these numerical simulations, we can use this to calculate the mass distribution for single Q-balls using $M = \Lambda|Q|^\alpha$ (we will absorb all numerical factors into the definition of Λ without loss of generality):

$$f_M(M) = \frac{M^{\frac{1-\alpha}{\alpha}}}{\alpha\Lambda^{1/\alpha}}\left[f_Q((M/\Lambda)^{1/\alpha}) + f_Q(-(M/\Lambda)^{1/\alpha})\right]. \tag{4.3}$$

It is important to note that a distribution well-localized in charge is also well-localized in mass. We can also use probability theory to calculate the mass of a collection of Q-balls. Under the assumption that a charge $Q_{\rm tot}$ is distributed amongst N Q-balls whose distribution is described by $f_Q(Q)$, the probability distribution function (PDF) for the total mass of this

collection of Q-balls is given by

$$f_M(M, Q_{\rm tot}, N) = \frac{\psi(M, Q_{\rm tot}, N)}{\int dM\, \psi(M, Q_{\rm tot}, N)}, \tag{4.4}$$

$$\psi(M, Q_{\rm tot}, N) = \int \left(\prod_{i=1}^{N} dQ_i\, f_Q(Q_i) \right) \times \delta\left(M - \Lambda \sum_{i=1}^{N} |Q_i|^\alpha \right) \delta\left(Q_{\rm tot} - \sum_{i=1}^{N} Q_i \right), \tag{4.5}$$

where ψ admits a simple-looking Fourier transform in M and $Q_{\rm tot}$:

$$\tilde{\psi}(\xi_M, \xi_{Q_{\rm tot}}, N) = \left[\int dQ\, e^{i(\xi_M |Q|^\alpha + \xi_{Q_{\rm tot}} Q)} f_Q(Q) \right]^N. \tag{4.6}$$

The power of α prevents analytic calculation of this PDF for all but the simplest charge distributions. Specifically, if we take the charge distribution to be a delta function: $f_Q(Q) = \delta(Q - Q_0)$, then the mass distribution is also a delta function: $f_M(M, Q_{\rm tot}, N) = \delta(M - NM_0)$, where $M_0 = \Lambda Q_0^\alpha$, and $Q_0 = Q_{\rm tot}/N$ to satisfy charge conservation (this constraint comes from a mathematical issue that arises due to the canceling of a delta function of the form $\delta(Q_{\rm tot} - NQ_0)/\delta(Q_{\rm tot} - NQ_0)$; we can see that if we consider $\delta(x)$ as the limit of a smooth function that approaches this distribution, then this ratio is unity provided $Q_0 = Q_{\rm tot}/N$).

For ease of computation, we will assume the delta function charge/mass distribution for the rest of this paper. This also has good theoretical motivation, as the Affleck-Dine baryogenesis scenario requires a large nonzero charge density, which tends to result in a highly-localized charge distribution.

4.3.1 Single length scale

One should notice that the mass distribution function calculated earlier is also a function of both the total charge $Q_{\rm tot}$ and the number of Q-balls N. During the chaotic fragmentation procedure, the number of Q-balls will fluctuate between horizons. So in order to get a full description of the fluctuations, we must supplement the mass distribution with a number distribution $p(N)$. This can be calculated from a simulation by simply counting the number

of Q-balls within the simulation volume. Here, we will assume that the number of Q-balls per horizon N is described by a Poisson distribution, as is typical for a random process such as fragmentation:

$$p(N) = e^{-N_f} \frac{N_f^N}{N!}, \tag{4.7}$$

where N_f is the average number of Q-balls per horizon at fragmentation. We then combine Equations 4.4 and 4.7 to create a joint PDF which describes the distribution of mass M within a horizon composed of N Q-balls (we also set $Q_{\rm tot} = Q_f$, the total charge on the horizon at t_f): $F_Q(M, N) = f_M(M, Q_f, N)p(N)$. This is manifestly normalized since $\sum_N \int dM\, F_Q = \sum_N (\int dM\, f_M)p = \sum_N p = 1$. We can then use this to calculate statistical moments such as the average horizon mass, average horizon Q-ball number, RMS fluctuations, etc:

$$\langle M \rangle = \sum_{N=1}^{\infty} \int_0^{\infty} dM\, M F_Q(M, Q_f, N) \approx M_f, \tag{4.8}$$

$$\langle N \rangle = \sum_{N=1}^{\infty} \int_0^{\infty} dM\, N F_Q(M, Q_f, N) = N_f, \tag{4.9}$$

$$N_{\rm RMS} = \left[\sum_{N=1}^{\infty} \int_0^{\infty} dM\, N^2 F_Q(M, Q_f, N) \right]^{1/2} = N_f, \tag{4.10}$$

where $M_f = \Lambda Q_f^{\alpha} N_f^{1-\alpha}$ is the horizon mass of Q-balls at t_f (the first relation is only approximate because $\langle N^{1-\alpha} \rangle \approx N_f^{1-\alpha}$, though the relative error scales as $|\langle N^{1-\alpha} \rangle - N_f^{1-\alpha}| / \langle N^{1-\alpha} \rangle \approx 1/10N_f$, so totally negligible for large N_f).

4.3.2 Multiple length scales

The previous treatment has the shortcoming that it can only describe Q-ball distributions with spatial extent the size of the horizon at the time of fragmentation. We now generalize this to handle distributions on an arbitrary scale. First, when considering a physical volume V at the time of fragmentation, the charge contained within this volume (assuming initial uniformity of the condensate) is given by $Q_{\rm tot} = Q_V = Q_f(V/V_f)$, where $V_f = \frac{4\pi}{3} t_f^3$ is the horizon volume at t_f. Second, the number distribution is altered so that the number of

Q-balls within volume V (assuming the same average number density $n_f = N_f/V_f$ across all scales) is described by

$$p(N,V) = e^{-N_f V/V_f} \frac{(N_f V/V_f)^N}{N!}. \tag{4.11}$$

The joint PDF for a mass M composed of N Q-balls contained within a volume V at the time of fragmentation t_f is then given by

$$F_Q(M,V,N) = \delta\left(M - M_f \left(\frac{N}{N_f}\right)^{1-\alpha} \left(\frac{V}{V_f}\right)^{\alpha}\right) p(N,V). \tag{4.12}$$

Note that if $V = V_f$, this reduces to the single-scale, horizon-size treatment.

In addition to being able to calculate quantities on each scale V individually, we will also want to sum the contributions from each scale in some cases (such as contributions to the PBH density from both subhorizon and superhorizon modes). To do so, we will sum over all volume scales from $V_{\min}$ to $V_{\max}$ using a coarse-graining method. We consider an arbitrary function of volume $g(V)$. The sum of the contributions from each scale $V_i = V_{\max}/\chi^{i-1}$ is then given by

$$\sum_{\{V\}} g(V) = \sum_{i=1}^{\lfloor 1+\log_\chi \frac{V_{\max}}{V_{\min}} \rfloor} g(V_i) \tag{4.13}$$

$$\approx \int_1^{1+\log_\chi \frac{V_{\max}}{V_{\min}}} di\, g(V_{\max}/\chi^{i-1}) \tag{4.14}$$

$$= \frac{1}{\ln \chi} \int_{V_{\min}}^{V_{\max}} \frac{dV}{V}\, g(V), \tag{4.15}$$

where we have used Euler-Maclaurin to approximate the sum, and $\chi \sim$ few is a parameter of the spacing between intervals of the coarse-graining procedure. We will take $\chi = e$ from now on for simplicity; another choice does not significantly affect the outcome provided it is not too close to unity. $V_{\min}$ is the smallest volume under consideration; there will be a natural cutoff due to the fact that Q-balls have a finite size, and so this scale is generally defined as the volume which contains some number $N_{\min} \sim 10$ Q-balls on average: $V_{\min}/N_{\min} = N_f/V_f$.

4.4 Q-ball and PBH densities

Using the framework of Section 4.3, we are now in a position to begin calculating the energy densities associated with the Q-balls, fluctuations in that energy density, and the resulting density of black holes.

4.4.1 Q-ball density at fragmentation

Using the formalism of Section 4.3.2, we can calculate the background energy density (over the largest scales) of Q-balls at t_f:

$$\langle \rho_Q(t_f) \rangle = \lim_{V \to \infty} \frac{\langle M \rangle}{V} = \frac{M_f}{V_f}, \tag{4.16}$$

which will be important in the discussion of density perturbations in Section 4.4. Since Q-balls are formed at rest, the evolution of the Q-ball density after fragmentation is simply that of decaying nonrelativistic matter $\langle \rho_Q(t) \rangle = \langle \rho_Q(t_f) \rangle \, (a_f/a)^3 e^{(t_f - t)/\tau_Q}$, where $\tau_Q = 1/\Gamma_Q$ is the lifetime of the Q-balls. Q-balls are generally considered stable with respect to decay into the quanta of the scalar field, but it is possible to decay through other processes. For example, if a coupling of the scalar field to a light fermion with mass $m < \omega$ exists, Q-balls can decay to these fermions through an evaporation process [166, 167, 168]. Q-balls can also decay if the U(1) symmetry is broken by some higher-dimension operators [133, 132, 135, 121]. We define Γ_Q to include all such decay channels.

4.4.2 Q-ball density perturbations due to fluctuations

Due to the stochastic nature of the fragmentation process, volumes of space can arise within which the number density of Q-balls exceeds the average number density. Due to the nonlinear relationship between Q-ball mass and charge $M = \Lambda |Q|^\alpha$, this also gives rise to fluctuations in the energy density within that volume. The density contrast in Q-balls at

fragmentation $\delta(t_f)$ for a volume V containing mass M is defined as

$$\delta(t_f) = \frac{\delta\rho_Q}{\langle\rho_Q\rangle} = \frac{M/V}{\langle\rho_Q\rangle} - 1 = \left(\frac{N/N_f}{M/M_f}\right)^{\frac{1-\alpha}{\alpha}} - 1 \tag{4.17}$$

where in the last line we have used the argument of the delta function in Equation 4.12 to eliminate V (this will be justified by an integral over V later). Note that if the Q-ball mass-charge relationship were linear ($\alpha = 1$), the perturbations would vanish identically.

The subhorizon density perturbations ($V < V_f$) are frozen during the initial radiation dominated era, but they grow linearly in the scale factor during the Q-ball dominated epoch: $\delta(t) = \delta(t_f)(a/a_Q) = \delta(t_f) = (t/t_Q)^{2/3}$, where t_Q is the beginning of the era of Q-ball domination. The structure growth generally goes nonlinear and decouples from the expansion around $\delta > \delta_c \sim 1.7$, at which point the overdense regions collapse and become gravitationally bound. However, some structures with $\delta < \delta_c$ can still collapse, and not all structures with $\delta > \delta_c$ are guaranteed to collapse into black holes. Due to nonsphericity of the gravitationally-bound structures, only a fraction $\beta = \gamma\delta^{13/2}(t_R)(M/M_Q)^{13/3}$ (where $\gamma \approx 0.02$ is a factor due to the nonsphericity, $M_Q = M_f(t_Q/t_f)^{3/2}$ is the horizon mass at the beginning of the Q-ball dominated era, and t_R is the end of the Q-ball dominated era, when the radiation comes to dominate again) will actually collapse to black holes [149, 169, 170] by the end of the Q-ball dominated era. We assume that structures with $\delta \geq \delta_c$ do not continue to grow past the point of nonlinearity, as they have already collapsed and had their chance to form a PBH; for these perturbations we set $\beta = \gamma\delta_c^{13/2}(M/M_Q)^{13/3}$ for $\delta(t_R) > \delta_c$. This refinement may not be necessary, as the average density perturbations are generally so small they never reach δ_c, and indeed, changing the value of δ_c does not seem to significantly alter the outcome.

Additional care must be taken to extend this to scales which enter the horizon at later times, and thus may not subject to the same amount of growth as subhorizon modes. Those that enter the horizon between $t_f < t < t_Q$ can be treated as effectively subhorizon since they enter the horizon before the Q-ball dominated epoch begins, and thus fluctuations are subject to the same amount of amplification as initially subhorizon modes. This includes

all volumes $V < V_Q$, where $V_Q = \frac{4\pi}{3} t_Q^3 (t_f/t_Q)^{3/2}$ is defined as the (initially superhorizon) physical volume at t_f which enters the horizon at t_Q: $(a_Q/a_f)^3 V_Q = \frac{4\pi}{3} t_Q^3$. Fluctuations which enter the horizon during the Q-ball dominated epoch are treated slightly differently, as they are only subjected to amplification from the time they enter the horizon t_h until the radiation comes to dominate again at t_R. We can account for this by calculating t_h for a given scale V via $(a(t_h)/a_f)^3 V = \frac{4\pi}{3} t_h^3$ (which gives us $t_h = (3/4\pi)(V/t_f^{3/2} t_Q^{1/2})$), and then replacing the scale factor a_R/a_Q with $a_R/a(t_h)$ in the definition of β above. This treatment is valid for all scales between $V_Q < V < V_R$, where $V_R = (4\pi/3) t_R^3 (t_Q/t_R)^2 (t_f/t_Q)^{3/2}$ is the physical volume at t_f which enters the horizon at t_R.

In addition to these details, we also enforce the constraint $\beta \leq 1$ in order to prevent PBH production probabilities over unity, though this does not become relevant unless the Q-ball dominated era is extremely long.

4.4.3 Primordial black hole density

We are now in a position to calculate the average energy density in PBH created during the Q-ball dominated era. We do this by calculating the energy density of Q-balls at t_f that *will eventually* form black holes by t_R by weighting the Q-ball energy density M/V by the collapse fraction/probability β evaluated at t_R, summing over all scales V, and then redshifting this value appropriately. The expression for this procedure is given by

$$\langle \rho_{\rm BH}(t_R) \rangle = \left(\frac{a_f}{a_R} \right)^3 \sum_{N=1}^{\infty} \int_{V_{\rm min}}^{V_R} \frac{dV}{V} \int_0^{\infty} dM \left(\beta \frac{M}{V} \right) F_Q, \tag{4.18}$$

where it should be understood that the integral over V is broken up into two separate domains, $[V_{\rm min}, V_Q]$ and $[V_Q, V_R]$, where separate definitions of β apply, as described in Section 4.4.2. Due to the complicated piecewise nature of the function β, the authors are unaware of any analytic solution, and further progress must be made numerically.

We find that Equation 4.18 can be rewritten in such a way that it only depends on the dimensionless numbers N_f, $r_f = t_Q/t_f$, and $r = t_R/t_Q$. r_f and r can be interpreted as measures of the duration of the era between the fragmentation and the beginning of Q-

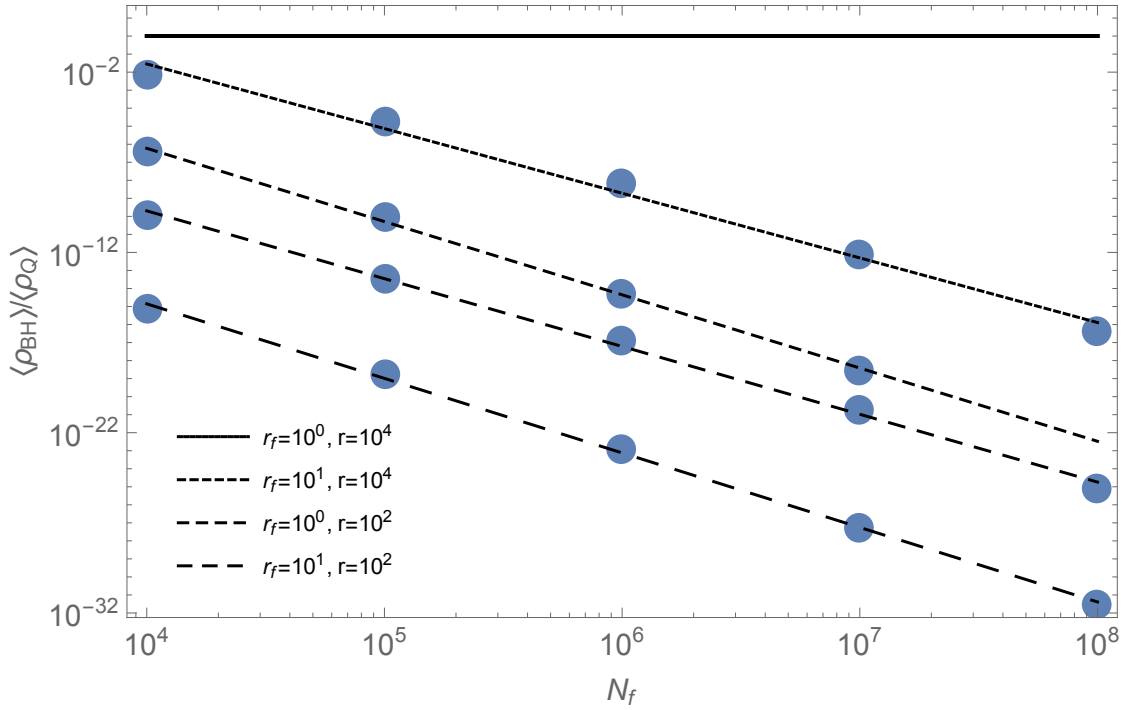

Figure 4.2: Fraction of Q-ball energy that goes into black holes. The ratio roughly scales as $\langle\rho_{\rm BH}\rangle\,/\,\langle\rho_Q\rangle \sim (4.6\times10^{-4})r_f^{-5.9}r^{4.4}N_f^{-3.7}$. The thick black line is the unity bound where 100% of the Q-ball energy goes into creating black holes.

ball domination, and the length of the Q-ball dominated era, respectively. The effect of these parameters on the black hole density can be seen in Figure 4.2. Larger r_f will reduce the fraction of Q-ball energy that goes into making black holes due to the dilution of the number density and increased horizon mass at t_Q due to the delay of the Q-ball dominated era. Larger r leads to an increased fraction of Q-ball energy that goes into black holes due to more amplification of the density perturbations, leading to a higher probability of PBH formation. Larger N_f reduces the fraction because of higher suppression of fluctuations due to the Poisson statistics. The form of the contours in this plot suggest that this ratio roughly scales as $\langle\rho_{\rm BH}\rangle\,/\,\langle\rho_Q\rangle \sim (4.6\times10^{-4})r_f^{-5.9}r^{4.4}N_f^{-3.7}$.

4.4.4 Black hole mass spectrum

One can derive the mass spectrum of the black holes by not integrating over M in Equation 4.18:

$$\frac{d\left\langle \rho_{\mathrm{BH}} \right\rangle}{dM} = \left(\frac{a_f}{a_R}\right)^3 \sum_{N=1}^{\infty} \int_{V_{\min}}^{V_R} \frac{dV}{V} \left(\beta \frac{M}{V}\right) F_Q. \tag{4.19}$$

This yields the differential black hole energy density $d\left\langle \rho_{\mathrm{BH}} \right\rangle / dM$. We find that the spectrum can be rewritten in terms of the parameter $\eta = M/M_f$ (fraction of horizon mass at t_f), along with the previously mentioned parameters $r_f = t_Q/t_f$, $r = t_R/t_Q$, and N_f. Calculation of this function can be done by evaluating Equation 4.19 at multiple values of η and then interpolating. An example is given in Figure 4.3. First, it's obvious from the normalization of each curve that the lower the number of Q-balls per horizon, the more black holes that are created. This is expected, as the Poisson statistics suppress the density fluctuations for large Q-ball number. The normalization also increases with r, as explained in Figure 4.2. Second, there is a hard lower cutoff in the PBH mass, which occurs at $\eta = N_{\min}/N_f$, which is due to the lower cutoff in the volume mentioned earlier. Above that, the BH number sharply increases with a power law $\propto \eta^{2.85\pm0.15}$; the extent of this region depends on the magnitude of r, with larger values leading to a larger range. We suspect that this is due to the fact that the small-scale density fluctuations have already reached their critical value δ_c and can no longer continue growing, whereas the large-scale fluctuations (which started out smaller) still have room to do so. Above that, the spectrum becomes approximately flat ($\propto \eta^{-0.15}$), meaning that the number of black holes in each decade of mass are comparable. Of course, the upper end of this range dominates the energy density of the distribution. Then, at around $M = M_Q$, there is a sharp transition and the slope becomes strongly negative ($\propto \eta^{-4.5}$) due to the reduced growth the superhorizon modes are subject to. Then, there is an upper exponential cutoff at $\eta \sim 10^8/N_f$ due once again to the Poisson statistics (the cutoff appears to take precedence over previously mentioned transitions).

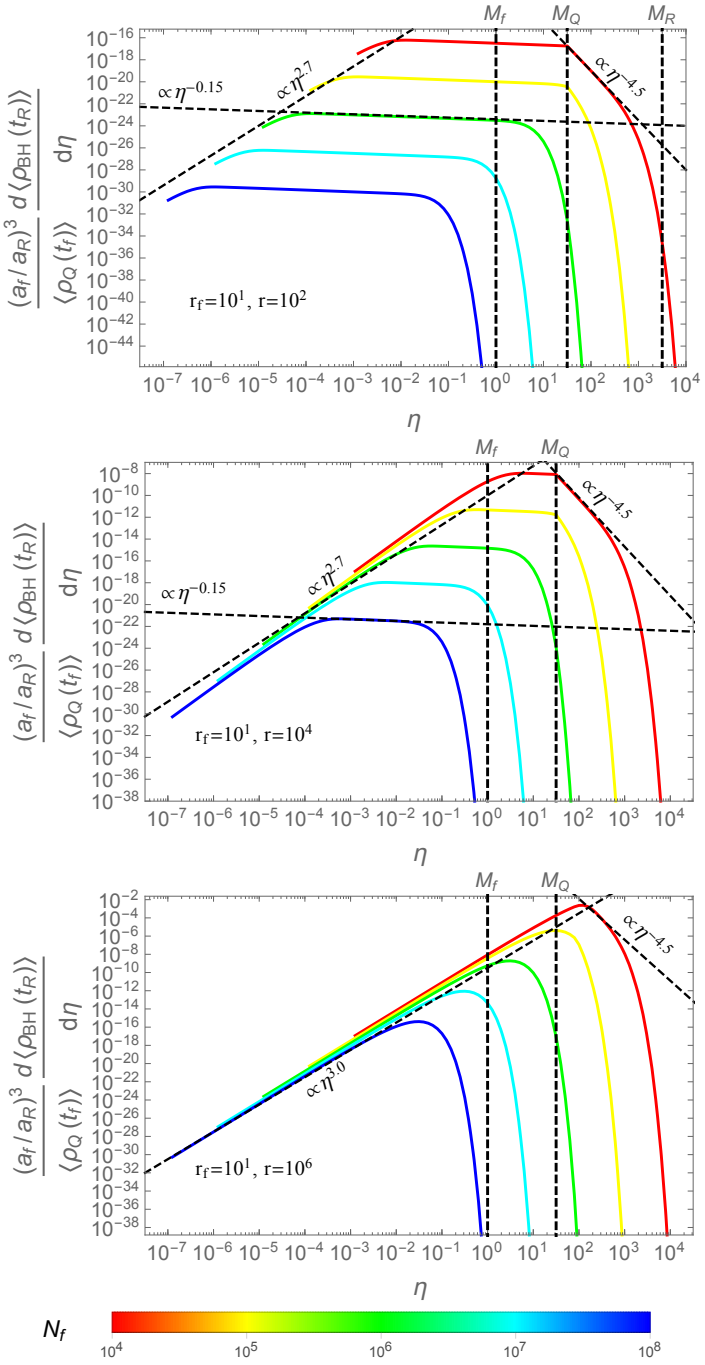

Figure 4.3: Differential PBH/Q-ball density ratio as a function of $\eta = M/M_f$. The density of black holes at t_R has been blueshifted back to t_f for comparison with the initial Q-ball density. The integral of these curves over η is the fraction of energy in Q-balls that goes into black holes, as shown in Figure 4.2. Notice that as r increases, the flat region shrinks. Parameters for the given spectra are shown in the lower left corner.

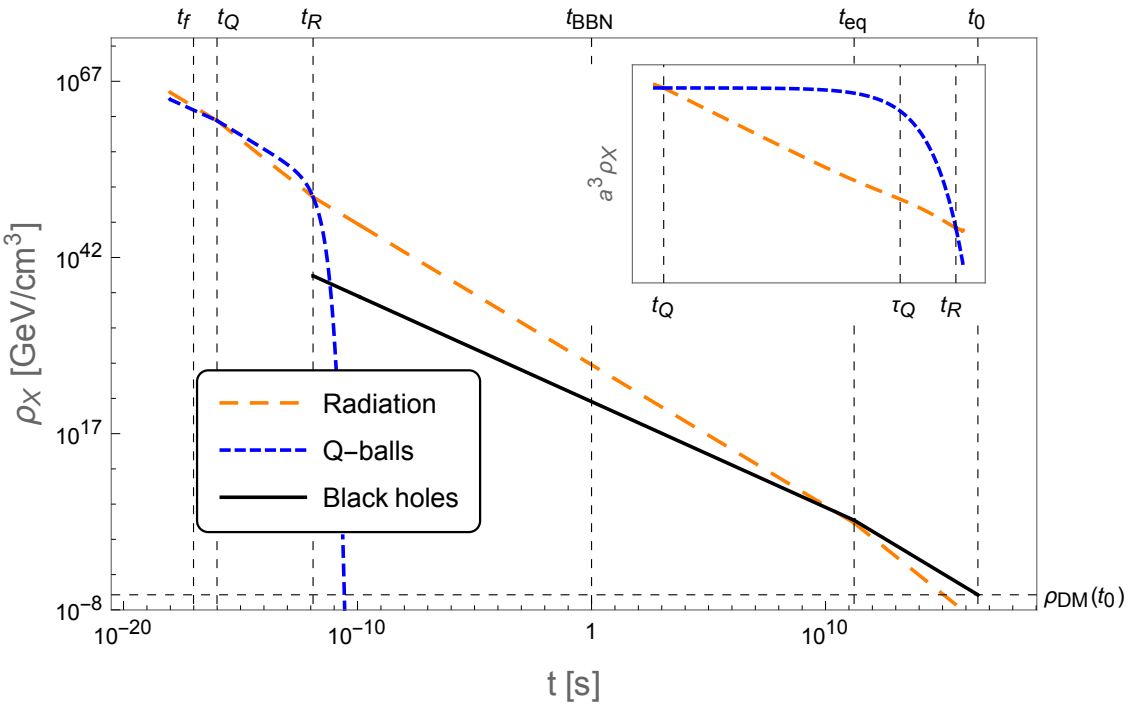

Figure 4.4: Evolution of energy density over cosmological history. The evolution of three "species" is plotted: radiation ρ_R (orange, long dash), Q-balls $\langle\rho_Q\rangle$ (blue, short dash), and black holes $\langle\rho_{\rm BH}\rangle$ (black, solid). Inset in the upper right corner is a zoomed-in view of the Q-ball dominated era ($t_Q < t < t_R$). The vertical axis is scaled by a factor of a^3, so that the decay of the Q-balls is evident (non-decaying matter would be represented by a straight horizontal line). The parameters of this model are $N_f = 10^6$, $t_f = 9.7 \times 10^{-18}$ s, $r_f = 10$, and $r = 1.3 \times 10^4$, which corresponds to production of PBH with peak mass of 4.4×10^{20} g making up 100% of the dark matter.

4.5 Cosmological history

We now give a detailed account of how the Q-balls, radiation, and black holes evolve throughout the history of the universe up until the present day, as seen in Figure 4.4. In summary: we assume an initial period of inflation and reheating in order to create a radiation dominated era with a uniform charged scalar field as a subdominant component of the energy density. The scalar field fragments into Q-balls at t_f, which then come to dominate the energy density at t_Q. During the Q-ball dominated epoch, primordial black holes are produced, and at t_R, their density is frozen in and evolves as nonrelativistic matter. After this initial matter dominated epoch, the Standard Model of cosmology resumes, and evolves through all the eras we are familiar with (BBN, matter-radiation equality, etc.) up to the present day.

The functions used to model the energy density evolution for each species is summarized in Appendix 4.12.

4.5.1 Initial radiation dominated era

After the end of inflation, the Universe enters a brief matter dominated era due to the coherent oscillations of the inflaton field. The decay of the quanta of this field at time $t_{\rm RH} = \Gamma_I^{-1}$ reheats the Universe, which enters a radiation dominated epoch with temperature $T_{\rm RH} = 0.55 g_*^{-1/4} (\Gamma_I M_p)^{1/2}$ and radiation energy density

$$\rho_R(t_{\rm RH}) = \frac{\pi^2}{30} g_*(T_{\rm RH}) T_{\rm RH}^4 \approx \frac{\pi^2}{327} \Gamma_I^2 M_p^2, \tag{4.20}$$

where $\Gamma_I \sim 1/t_{\rm RH}$ is the decay width of the inflaton oscillations. The radiation density redshifts as $\rho_R(t) = \rho_R(t_{\rm RH})(a_{\rm RH}/a)^4 = \rho_R(t_{\rm RH})(t_{\rm RH}/t)^2$ during this epoch, which ends up canceling the factor of Γ_I to give us

$$\rho_R(t) = \frac{\pi^2 M_p^2}{327 t^2}; \qquad t_{\rm RH} < t < t_Q \tag{4.21}$$

At some point t_f, the scalar condensate fragments into Q-balls, resulting in an energy density given by Equation 4.16. The Q-balls then redshift as decaying nonrelativistic matter:

$$\langle \rho_Q(t) \rangle = \langle \rho_Q(t_f) \rangle \left(\frac{a_f}{a} \right)^3 e^{-(t-t_f)/\tau_Q} \tag{4.22}$$

$$= \frac{3 \Lambda Q_f^\alpha N_f^{1-\alpha}}{4\pi t_f^{3/2} t^{3/2}} e^{-(t-t_f)/\tau_Q}; \qquad t_f < t < t_Q \tag{4.23}$$

4.5.2 Q-ball dominated era

At some point t_Q, the Q-balls come to dominate the energy density. This time is defined by $\rho_R(t_Q) = \langle \rho_Q(t_Q) \rangle$, using the equations of the previous section. During this era, Q-ball decays begin to affect the radiation density, causing the radiation temperature to decrease less slowly than it normally would due to the expansion. Following the analysis of Scherrer

and Turner [171], the radiation density in this epoch due to the decay of the Q-balls can be modeled as

$$\rho_R(t) = \left[\rho_R(t_Q) + \langle\rho_Q(t_Q)\rangle \int_{x_0}^{x} dx'\, z(x') e^{-x'}\right] z^{-4}, \tag{4.24}$$

where $x \equiv \Gamma_Q t$, $x_0 = \Gamma_Q t_Q$, and $z = (x/x_0)^{2/3}$. The Q-balls continue to redshift and decay, leading to

$$\langle\rho_Q(t)\rangle = \frac{3\Lambda Q_f^\alpha N_f^{1-\alpha} t_Q^{1/2}}{4\pi t_f^{3/2} t^2} e^{-(t-t_f)/\tau_Q}; \qquad t_Q < t < t_R \tag{4.25}$$

As the Q-balls decay, eventually the radiation comes to dominate again at t_R, defined by $\rho_R(t_R) = \langle\rho_Q(t_R)\rangle$. Using Equations 4.21, 4.22, 4.24 and 4.25, this gives us the relation

$$1 + \left(\frac{t_R}{\tau_Q}\right)^{-2/3} \Gamma\left(\frac{5}{3}, \frac{t_Q}{\tau_Q}, \frac{t_R}{\tau_Q}\right) = \left(\frac{t_R}{t_Q}\right)^{2/3} e^{(t_Q - t_R)/\tau_Q}, \tag{4.26}$$

where Γ is the generalized incomplete gamma function. This allows us to solve (numerically) for $r_Q \equiv \tau_Q/t_Q$ as a function of $r = t_R/t_Q$. At this point, if we specify t_f, r_f and r, we can calculate the other parameters t_Q, t_R, τ_Q, and ΛQ_f^α via

$$t_Q = t_f r_f, \quad t_R = t_f r_f r, \quad \tau_Q = t_f r_f r_Q(r), \tag{4.27}$$

$$\Lambda Q_f^\alpha = \frac{4\pi M_p^2 t_f}{3 \cdot 327 r_f^{1/2} N_f^{1-\alpha}} e^{(1-1/r_f)/r_Q(r)}, \tag{4.28}$$

from which we can calculate all other quantities of interest ($M_f = \Lambda Q_f^\alpha N_f^{1-\alpha}$, $M_Q = M_f r_f^{3/2}$, etc.).

4.5.3 Standard cosmological era

After the Q-balls have decayed sufficiently, the universe returns to a radiation dominated era, and the standard cosmology begins. In order to evolve the radiation, Q-ball, and black hole densities to the present day, one would naïvely use $a_1/a_2 = (t_1/t_2)^n$, where

$n = \frac{1}{2}\,(\frac{2}{3})$ in a radiation (matter) dominated era, keeping in mind that the universe transitions between the two at $z_{\rm eq} \approx 3360$, or $t_{\rm eq} \approx 4.7 \times 10^4$ yr. However, due to the extended era of matter domination, the time at which cosmological events (such as BBN, matter-radiation equality, or recombination) occur are not the same as in the standard cosmology. Instead, one must evolve according to the universe's *thermal* history, where cosmological events occur at specific temperatures. In this case, one must use $a_1/a_2 = g_{*S}^{1/3}(T_2)T_2/g_{*S}^{1/3}(T_1)T_1$ and evolve from T_R (defined by $\rho_R(t_R) = (\pi^2/30)g_*(T_R)T_R^4$) to $T_0 = 2.7$ K $= 2.3$ meV. This has the advantage of accurately accounting for any deviation from cosmological history. We can then find the time at which some event X occurs by solving $\rho_R(t_X) = (\pi^2/30)g_*(T_X)T_X^4 = \rho_R(T_R)(a(t_R)/a(t))^4$. In order to ensure that this early matter dominated era does not spoil the canonical cosmological thermal history, we enforce an additional constraint $T_R > T_{\rm BBN} \sim$ MeV, so that the entropy injection from Q-ball decays does not interfere with nucleosynthesis.

4.6 Observational constraints

We now examine the observational constraints on primordial black holes and where our results fit in. The constraints come from a wide variety of sources, such as extragalactic gamma rays from evaporation [172, 173], femtolensing of gamma ray bursts (GRB) [174], capture by white dwarfs [175], microlensing observations from HSC [90], Kepler [176, 177], and EROS/MACHO/OGLE [178], measurements of distortion of the CMB [179, 180], and bounds on the number density of compact X-ray objects [181] (constraints summarized in [182, 146, 183]). The constraints are typically expressed in a form that assumes a monochromatic distribution of PBH masses. However, in the case of an extended mass distribution (such as we have in this scenario), care must be taken to apply the limits correctly. To do this, we follow the procedure outlined in [149, 183], which amounts to dividing the mass spectrum into a number of bins (labeled by the index i), then integrating the dark matter fraction over the interval contained in the bin:

$$f_i = \frac{1}{\rho_{\rm DM}} \int_{M_i}^{M_{i+1}} dM\, \frac{d\,\langle \rho_{\rm BH}(t_0)\rangle}{dM}, \tag{4.29}$$

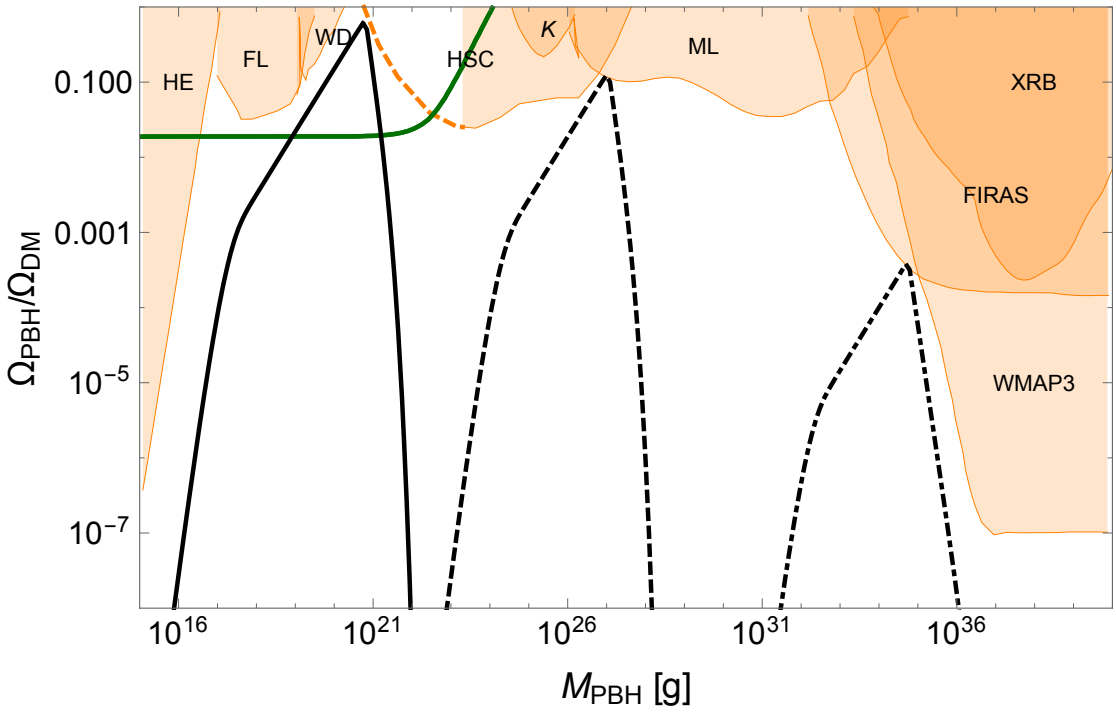

Figure 4.5: Comparison of observational PBH constraints $f_{\rm con}(M) = \Omega_{\rm PBH}(M)/\Omega_{\rm DM}$ (orange, shaded) with the dark matter fraction per logarithmic interval (black), defined by $f(M) = \frac{M}{\rho_{\rm DM}} \frac{d\langle \rho_{\rm BH}(t_0) \rangle}{dM}$. This is a crude comparison, and to be rigorous one should use the procedure outlined by the use of Equation 4.29. Parameters for the three curves are $t_f = 1.12 \times 10^{-17}$ s, $r_f = 1.1$, $r = 4.47 \times 10^2$, $N_f = 10^6$, $f = 1$ (solid line), $t_f = 2.0 \times 10^{-11}$ s, $r_f = 1.1$, $r = 1.58 \times 10^3$, $N_f = 10^6$, $f = 0.2$ (dashed line), and $t_f = 1.0 \times 10^{-3}$ s, $r_f = 1.1$, $r = 4.47 \times 10^2$, $N_f = 10^5$, $f = 0.001$ (dot-dashed line). The HSC constraints reported in [90] do not apply below 10^{-10} solar masses because the Schwarzschild radius of the black hole becomes smaller than the wavelength of light, and the wave effects suppress the magnification [184, 185]. Also shown is the boundary of the parameter range (dark green) above which PBH collisions with neutron stars can account for all r-process element production in the Milky Way [87].

which is then compared with the constraints on a bin-by-bin basis. We find that for sufficient choices of the parameters N_f, t_f, r_f, and r, our model can produce black holes over practically the entire parameter space allowed by the constraints (see Fig. 4.5). Notably, this Figure illustrates two interesting points: 1) that this mechanism is capable of generating black holes which can account for both 100% of the dark matter in the region $M \sim 10^{20}$ g and production or r-process elements [87], and 2) it is also capable of generating black holes with sufficient mass to explain the recent LIGO observation GW150914 [186]. Some studies have even argued that PBH can account for 100% of the DM in this range by contesting the CMB

constraints [155]. The three contours in Figure 4.5 are, however, simply chosen by hand for illustrative purposes, and are therefore not representative of the entire parameter space allowed to this mechanism, which is much wider than suggested by the given parameters.

4.7 Parameter space

We now explore the parameter space available to this mechanism in which it is possible to account for a considerable fraction of the dark matter while avoiding observational constraints. To do so, we develop an algorithm to accomplish this task in the following manner: since the function $\left((a_f/a_R)^3/\left\langle\rho_Q(t_f)\right\rangle\right)\left(d\left\langle\rho_{\rm BH}(t_R)\right\rangle/d\eta\right)$ is determined solely by the parameters r_f and r, we generate a list of such functions by sampling the $r - r_f$ plane at various points. Then, for each (r, r_f) pair, we vary t_f using a weighed bisection method until $\max(|1 - f_i/f_{\rm con}(M_i)|) < \epsilon = 10^{-1}$, with f_i given by Equation 4.29. This determines the value of t_f which gives the maximum dark matter fraction allowed by the constraints for the given values of r and r_f. Once that has been determined, we can calculate all other relevant quantities of interest, such as $M_{\rm BH,peak}$, T_R, and the dark matter fraction $f = \Omega_{\rm PBH}/\Omega_{\rm DM}$. The results for $N_f = 10^6$ are shown in Figure 4.6.

We can see from this Figure that the contours of constant f are highly correlated with the values of $M_{\rm BH,peak}$. This is due to the fact that the observational constraints are solely a function of M, and the calculated spectrum $f(M)$ is quite sharply peaked at $M_{\rm BH,peak}$. The region of $f \geq 1$ roughly follows the contour of $M_{\rm BH,peak} = 10^{20}$ g, where the constraints are weakest, due to this fact. The general tendency appears to be that for increasing r, the spectrum favors heavier black holes, while for increasing r_f, it favors lighter black holes. This is because the longer the period of structure formation, the more the large mass perturbations (which initially have small δ) grow, increasing the probability that they collapse to black holes, whereas the longer the period between fragmentation and Q-ball domination, the more the energy density of Q-balls is diluted, so that the value of t_f has to be lower in order to achieve the same value of f that one would with smaller r_f. The smaller t_f, the smaller the horizon mass, and the smaller the PBH masses. This can be quantified, as the contours of

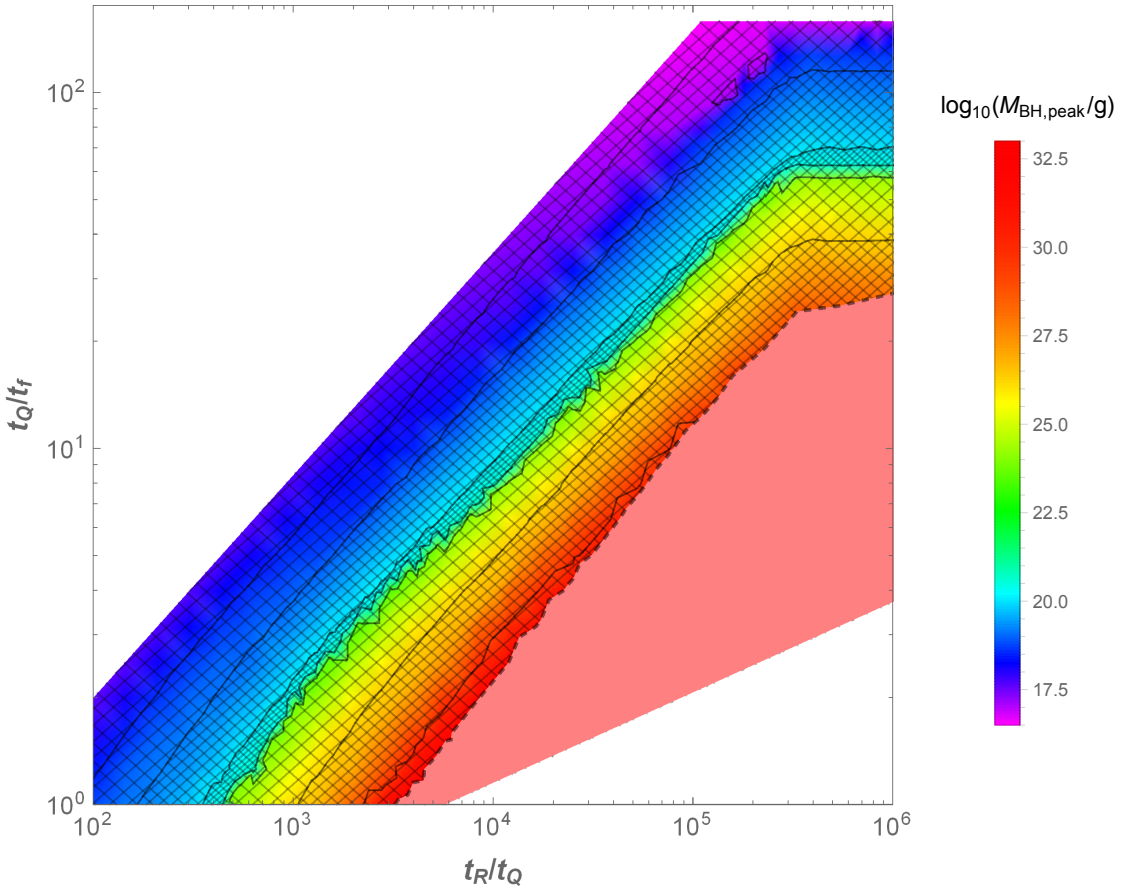

Figure 4.6: Parameter space available to the model with $N_f = 10^6$. Color gradient denotes the peak black hole mass $M_{\mathrm{BH,peak}}$ (warmer colors denote higher masses), and the black contours are surfaces of constant $f = \Omega_{\mathrm{PBH}}/\Omega_{\mathrm{DM}}$. Different levels of cross-hatching between f contours indicate the range of maximum f values, with the densest corresponding to $f \geq 1$ (highly correlated with $M_{\mathrm{BH,peak}} = 10^{20}$ g), the next dense $10^{-1} < f < 1$, and so on, down to $f < 10^{-3}$. Pink shaded region to the bottom right is ruled out due to $T_R \geq 1$ MeV for that set of parameters. Jagged edges of the contours are likely due to shortcomings of the interpolation method.

constant f very roughly follow $r^{0.63}/r_f \sim$ const.

However, at around $r \gtrsim 3.2 \times 10^5$, the character of the plot changes so that the spectrum appears to no longer depend on r, only on r_f. This is likely due to the definition of β discussed in Section 4.4.2, in which density perturbations are not allowed to grow past δ_c, which makes it so that further increases in r have no effect on the spectrum. Further increases in r_f, however, serve to further dilute the Q-ball density before structure formation can occur, lowering the necessary t_f as mentioned above.

The pink region where $T_R > 1 MeV$ is ruled out since in this region Q-ball decays begin to interfere with nucleosynthesis. We can see that it is correlated with high mass, as the later the fragmentation (meaning larger horizon mass), the less time there is for the Q-balls to dominate before the universe cools sufficiently enough that nucleosynthesis begins. One might notice that the mass of the black holes seen at LIGO in the GW150914 event lies beyond the range indicated in this Figure, but in Figure 4.5 we have plotted a contour that has $M_{\rm BH,peak} \sim 30$ M$_\odot$. This is because the contour in Fig. 4.5 is for $N_f = 10^5$, whereas Fig. 4.6 has N_f fixed at 10^6. We can see in Fig. 4.3 that the density spectrum has a peak at higher masses for lower values of N_f, so that the equivalent plot to Fig. 4.6 for $N_f < 10^6$ would see the $T_R < 1$ MeV constraint pushed to higher values of $M_{\rm BH,peak}$; enough so that they could explain the 30 M$_\odot$ black holes while avoiding the nucleosynthesis constraint.

4.8 Topological defects

Topological defect formation can also lead to the production of PBHs if the topological defects come to dominate the energy density. The analysis is sufficiently different from that of Q-balls, primarily because typically only one defect per horizon is produced at the time of formation due to the Kibble mechanism [187]. However, the general mechanism remains the same: small number densities of defects lead to large fluctuations relative to the background density, these fluctuations become gravitationally bound and collapse to form black holes once the relic density has come to dominate, and the relics decay due to some instability (such as gravitational waves or decay to Nambu-Goldstone bosons in the case of

cosmic strings). In order to accurately model production of PBHs from these defects, one should calculate the expected density perturbations on initially superhorizon scales, which only begin to grow once these scales pass back within the horizon and the defects come to dominate the universe's energy density.

Cosmic strings are probably the most likely candidate for primordial relics due to the fact that they are typically cosmologically safe, as the energy density in string loops is diluted during expansion at the same rate as radiation, a^{-4} [188, 189]. In contrast, the string "network" (i.e. infinitely long strings) energy density redshifts as a^{-2} so that they quickly come to dominate the universe's energy density. However, once long strings start intercommuting to produce loops, and these loops subsequently self-intersect to fragment into smaller loops, the string network approaches a scaling solution which leads to the a^{-4} dilution of string loops [190].

However, this scaling solution critically relies on the probability of string intercommutation being very close to unity so that the long strings can efficiently break into small loops. If this probability was sufficiently low, then the string density could redshift as a^{-2} or a^{-3}, survive until a matter/string dominated era, initiate structure formation, collapse to form PBHs, and then subsequently decay. As long as these conditions are satisfied, cosmic strings could act as a source of PBH. In addition, there exists a large class of solutions to the string equations of motion which never self-intersect [191], making this scenario plausible.

4.9 Discussion

The mechanism we have discussed has a number of advantages over some other models. It is extremely effective in creating primordial black holes across a broad range of masses, and it does not require the tuning of the inflaton potential [151, 144, 150, 148]. In addition, we did not have to make any ad-hoc assumptions regarding density contrast fluctuations; the fluctuations are calculable from first principles.

The mechanism is also generally applicable to practically any complex scalar field with a conserved global charge and flat potential, so that the formation of PBH is now a gen-

eral prediction of any theory containing such charged scalars. In particular, supersymmetric extensions to the Standard Model typically have such fields, making the production of primordial black holes a general prediction of such theories. For the case of supersymmetric Q-balls with the SUSY-breaking scale $\Lambda_{\rm SUSY} > 10$ TeV, the fragmentation time cannot be much longer than the Hubble time $H^{-1} \sim M_p/g_*^{1/2}\Lambda_{\rm SUSY} \lesssim 8 \times 10^{-15}$ s, which corresponds to peak PBH masses of about 10^{23}g (assuming $N_f \sim 10^6$). The solid black curve illustrated in Figure 4.5 satisfies this bound, thus primordial black holes from supersymmetric Q-balls can account for 100% of the dark matter.

Supersymmetric Q-balls themselves have been suggested as the source of dark matter in models where they are entirely stable [133, 121, 29, 168, 31]. However, the stability is model-dependent, and it only applies to Q-balls carrying baryonic charge (so-called B-balls), since those carrying leptonic charge (L-balls) would quickly evaporate to neutrinos [166]. In our scenario, a short evaporation timescale is precisely what is needed to end the early era of Q-ball domination before nucleosynthesis begins. The L-balls would then be composed of slepton fields which subsequently decay to neutrinos at an early time. Since neutrinos do not decouple from the plasma until just before nucleosynthesis ($T \gtrsim$ few MeV), they thermalize quickly. If they decay early enough, it may even be possible to generate the baryon asymmetry through conversion of lepton number to baryon number via sphaleron processes during the electroweak phase transition [192].

Just like the typical scenario for PBH formation during the radiation-dominated era, the primary factor in determining the mass of the resultant PBH is the horizon mass at the time of PBH production. In Fig. 4.3, you can see that the peak BH mass is typically within an order of magnitude or two of the horizon mass at the time of fragmentation ($\eta = 1$) (since the curves plotted are $d\rho_{\rm BH}/d\eta$, one must multiply by η to get an idea of the total PBH density within a specific mass interval, which puts the peak of $\eta\, d\rho_{\rm BH}/d\eta$ near the location of the exponential cut-off as you go to higher η). The variation in the location of the peak for different N_f can be explained due to the observation that smaller numbers of Q-balls lead to higher initial density contrast, which makes it easier to form larger black holes, and in greater numbers. Larger numbers of Q-balls per horizon would have the opposite effect.

But the mass of the horizon at fragmentation remains the primary factor. The horizon mass at the time of fragmentation is simply the energy density of Q-balls (which is diluted by t^-2) times the horizon volume (which scales as t^3), though in order to calculate this in a self-consistent way that takes the parameters of this mechanism into account we can use Eq. 4.28 along with the comment immediately following it. The main takeaway is that it is linear in t, so that later fragmentation leads to larger black holes in general. Though the value of $M_{\rm peak}$ has a very large range, it cannot be made arbitrarily high. Specifically, the constraint that fragmentation (and decay) of the Q-balls must occur before BBN acts as a constraint on the horizon mass at fragmentation, and therefore restricts the masses of the largest black holes produced to be less than about $10\,\mathrm{M}_\odot$.

There are some remaining open questions, such as how well the assumption that all Q-balls within the volume V are the same charge models this scenario. Simulations show that for scalar condensates with a high ratio of charge density to energy density, this is a good prediction, as all the Q-balls formed from this initial condition typically have similar sizes. This is also theoretically understood for a scalar condensate with a sufficiently large charge density [31, 126, 124]. However, condensates with a large energy density and small charge density generally produce broad charge distributions, nearly symmetric about $Q = 0$, since the excess energy cannot be contained in Q-balls with the same sign of Q while also conserving charge. We suspect that in this scenario the production of PBH will be reduced, since the charge conservation does not play as significant a role. Loss of energy due to scalar radiation in the fragmentation process may still be able to produce energy density inhomogeneities, but this will require further study. In the same manner, the production of oscillons from the fragmentation of a real scalar field may be able to produce significant numbers of PBH as well.

One may also wonder what sort of mechanism is needed in order to ensure the Q-balls decay at the correct time. As an example, following the work of [121], the lifetime of a Q-ball with initial charge Q_0 decaying to pseudo-Goldstone bosons through the effects of a

charge-violating operator of the form $V_{\not Q}(\phi) = g\phi^n(\phi^*)^m/\Lambda_*^{n+m-4} + \text{c.c.}$ is given by

$$\tau \approx \frac{1 - Q_0^{1-a}}{(a-1)\Gamma_0}, \tag{4.30}$$

where

$$a = \frac{1}{4}(7 + 2(n+m-2)), \tag{4.31}$$

$$\Gamma_0 = 112.7|g|^2 e^{-0.236(n+m)}(n-m)^2 J_{nm}\Lambda(\Lambda/\Lambda_*)^{2(n+m)-8}, \tag{4.32}$$

and $J_{nm} \sim O(10^{-7} - 10^{-6})$. For $g \sim 0.1$, $\Lambda_* \sim 10^{16}$ GeV, and $\Lambda \sim 10^9$ GeV, the lifetime of a Q-ball decaying through an operator with $(n, m) = (2, 3)$ is about $\tau \sim 10^{-13}$ s, which is sufficient to explain the curve of Figure 4.4 (and satisfies the SUSY bound). Decay through these higher-dimension operators isn't the only way to induce the decay of Q-balls though; many other scenarios have been explored in the literature [133, 132, 135].

This work also begs the question of what possible observables exist that could show the Q-ball clusters collapse to black holes. We assume that the collapse will produce a stochastic gravitational wave background [193], which could be detected by future observatories (or put constraints on the model). Further evolution of the PBH population could see successive mergers, which in addition to creating another stochastic GW background [194], could also alter the distribution of black hole masses (in addition to evaporation/accretion effects [195, 196]). We propose to calculate the gravitational wave spectrum in a future publication.

4.10 Conclusion

In summary, we have shown that the number density fluctuations of a Q-ball population in the early universe can lead to production of primordial black holes with sufficient abundance to explain the dark matter. Scalar fields and Q-ball formation are general features of supersymmetric extensions to the Standard Model, which provides a good motivation for this mechanism. A similar mechanism using solitons, topological defects, or other compact ob-

jects associated with scalar fields in the early universe can also lead to a copious production of primordial black holes.

4.11 Acknowledgements

This work was supported by the U.S. Department of Energy Grant No. DE-SC0009937. A.K. was also supported by the World Premier International Research Center Initiative (WPI), MEXT, Japan.

4.12 Appendix: Evolution of energy densities

Here we tabulate the functional form of the energy density for each species (radiation, Q-ball, black hole) up until the present day. The values for t_f, t_Q, t_R, and τ_Q are taken as input parameters (subject to some self-consistency conditions), while the values of $t_{\rm eq}$ and t_0 are calculated from the procedure described in Section 4.5.3.

4.12.1 Radiation

The radiation density begins after reheating and is given by Equation 4.21. From this point we evolve it through time to the present day, taking into account the contribution due to Q-ball decays during the period $t_Q < t < t_R$.

$$\rho_R(t) = \begin{cases} \frac{\pi^2 M_p^2}{327 t^2} & t_{\rm RH} < t < t_Q \\ \frac{\pi^2 M_p^2}{327 t_Q^2}\left[1+\left(\frac{\tau_Q}{t}\right)^{2/3}\Gamma\left(\frac{5}{3},\frac{t_Q}{\tau_Q},\frac{t}{\tau_Q}\right)\right]\left(\frac{t_Q}{t}\right)^{8/3} & t_Q < t < t_R \\ \frac{\pi^2 M_p^2}{327 t_Q^2}\left[1+\left(\frac{\tau_Q}{t_R}\right)^{2/3}\Gamma\left(\frac{5}{3},\frac{t_Q}{\tau_Q},\frac{t_R}{\tau_Q}\right)\right]\left(\frac{t_Q}{t_R}\right)^{8/3}\left(\frac{t_R}{t}\right)^2 & t_R < t < t_{\rm eq} \\ \frac{\pi^2 M_p^2}{327 t_Q^2}\left[1+\left(\frac{\tau_Q}{t_R}\right)^{2/3}\Gamma\left(\frac{5}{3},\frac{t_Q}{\tau_Q},\frac{t_R}{\tau_Q}\right)\right]\left(\frac{t_Q}{t_R}\right)^{8/3}\left(\frac{t_R}{t_{\rm eq}}\right)^2\left(\frac{t_{\rm eq}}{t}\right)^{8/3} & t_{\rm eq} < t < t_0 \end{cases} \tag{4.33}$$

4.12.2 Q-balls

The Q-balls are created at the time of fragmentation t_f, and evolve as decaying nonrelativistic matter. The magnitude of the energy density becomes insignificant shortly after t_R. $M_f = \Lambda |Q_f|^\alpha N_f^{1-\alpha}$ can be determined from specifying t_f, r_f, r, and N_f, as given in Section 4.5.

$$\langle \rho_Q(t) \rangle = \begin{cases} \frac{3M_f}{4\pi t_f^3} \left(\frac{t_f}{t}\right)^{3/2} e^{-(t-t_f)/\tau_Q} & t_f < t < t_Q \\ \frac{3M_f}{4\pi t_f^3} \left(\frac{t_f}{t_Q}\right)^{3/2} \left(\frac{t_Q}{t}\right)^2 e^{-(t-t_f)/\tau_Q} & t_Q < t < t_R \\ \frac{3M_f}{4\pi t_f^3} \left(\frac{t_f}{t_Q}\right)^{3/2} \left(\frac{t_Q}{t_R}\right)^2 \left(\frac{t_R}{t}\right)^{3/2} e^{-(t-t_f)/\tau_Q} & t_R < t < t_{\rm eq} \\ \frac{3M_f}{4\pi t_f^3} \left(\frac{t_f}{t_Q}\right)^{3/2} \left(\frac{t_Q}{t_R}\right)^2 \left(\frac{t_R}{t_{\rm eq}}\right)^{3/2} \left(\frac{t_{\rm eq}}{t}\right)^2 e^{-(t-t_f)/\tau_Q} & t_{\rm eq} < t < t_0 \end{cases} \tag{4.34}$$

4.12.3 Black holes

The black holes are created towards the end of the initial Q-ball dominated era, and their density at t_R is given by Equation 4.18:

$$\langle \rho_{\rm BH}(t_R) \rangle = \left(\frac{a_f}{a_R}\right)^3 \sum_{N=1}^{\infty} \int_{V_{\rm min}}^{V_R} \frac{dV}{V} \int_0^\infty dM \left(\beta \frac{M}{V}\right) F_Q \tag{4.35}$$

$$= \left(\frac{t_f^{3/2} t_Q^{1/2}}{t_R^2}\right) \frac{M_f}{V_f} \sum_{N=1}^{\infty} \int_{x_{\rm min}}^{x_R} dx\, \beta(x,N) x^{N+\alpha-2} e^{-x} \tag{4.36}$$

where

$$\beta(x,N) = \begin{cases} \left(\left(\frac{N}{x}\right)^{1-\alpha} - 1\right) \left(\frac{t_R}{t_*}\right)^{2/3} \geq \delta_c : \min\left(1, \gamma \delta_c^{13/2} \left(\frac{N}{N_f} \frac{x^\alpha}{N^\alpha}\right)^{13/3} r_f^{-13/2}\right) \\ \left(\left(\frac{N}{x}\right)^{1-\alpha} - 1\right) \left(\frac{t_R}{t_*}\right)^{2/3} < \delta_c : \min\left(1, \gamma \left(\left(\frac{N}{x}\right)^{1-\alpha} - 1\right)^{13/2} \left(\frac{t_R}{t_*} \frac{N}{N_f} \frac{x^\alpha}{N^\alpha}\right)^{13/3} r_f^{-13/2}\right) \end{cases} \tag{4.37}$$

and

$$t_* = \begin{cases} t_Q & x_{\min} < x < x_Q \\ \frac{3V_f x}{4\pi N_f t_f^{3/2} t_Q^{1/2}} & x_Q < x < x_R \end{cases} \tag{4.38}$$

where $x_{\min} = N_f V_{\min}/V_f = N_{\min}$, $x_Q = N_f V_Q/V_f$, and $x_R = N_f V_R/V_f$. After this has been evaluated, the evolution of the black hole density is fairly straightforward:

$$\langle \rho_{\rm BH}(t) \rangle = \begin{cases} \langle \rho_{\rm BH}(t_R) \rangle \left(\frac{t_R}{t}\right)^{3/2} & t_R < t < t_{\rm eq} \\ \langle \rho_{\rm BH}(t_R) \rangle \left(\frac{t_R}{t_{\rm eq}}\right)^{3/2} \left(\frac{t_{\rm eq}}{t}\right)^2 & t_{\rm eq} < t < t_0 \end{cases} \tag{4.39}$$

CHAPTER 5

Primordial Black Holes from Inflaton Fragmentation into Oscillons

The content of this chapter has been submitted for publication and can be found on the arXiv as *Primordial Black Holes from Inflaton Fragmentation into Oscillons*, E. Cotner, A. Kusenko, and V. Takhistov, arXiv:1801:03321 (2018) [197].

We show that fragmentation of the inflaton into long-lived spatially localized oscillon configurations can lead to copious production of black holes. In a single-field inflation model primordial black holes of *sublunar* mass can form, and they can account for all of the dark matter. We also explore the possibility that solar-mass primordial black holes, particularly relevant for gravitational wave astronomy, are produced from the same mechanism.

5.1 Introduction

Primordial black holes (PBHs) can form in the early Universe and can account for all or part of the dark matter (DM) (e.g. [143, 82, 83, 144, 145, 146, 148, 158, 149, 150, 151, 198, 181, 152, 199, 200, 201]). They have also been linked to a variety of topics in astronomy, including the recently discovered [202, 203, 204] gravitational waves [205, 206, 155, 207, 208, 157, 209, 210], formation of supermassive black holes [211, 147, 206] as well as r-process nucleosynthesis [87] and gamma-ray bursts [84] from compact star disruptions.

Many proposed scenarios of PBH formation assume that inflation has generated some excess of density perturbations on certain scales, which produce PBHs when they re-enter the Hubble horizon during the radiation dominated phase or during some intermediate matter-

dominated stage (for review, see [169, 145]). The required inflaton potentials could be *ad hoc*, or can be well-motivated in the context of hybrid inflation [144], supergravity [148], etc. PBHs can also form from large extended objects, such as non-topological solitons in supersymmetric theories, which behave as matter and come to dominate the universe for a short time before decaying [158, 142]. In this case, the overdensities needed for PBH formation result from statistical fluctuations in a system with a relatively low number of very massive "particles" and not from the spectrum of primordial density fluctuations. In this *Letter* we show that if the inflaton potential admits long-lived oscillon solutions, their formation can lead to copious production of PBHs.

5.2 Oscillons

Oscillons [212, 213, 214, 215, 216, 217] arise in many well motivated theories with scalar fields, such as models of inflation [218], axions [77] or moduli [219]. The oscillons are localized, metastable, pseudo-solitonic configurations of real scalar fields. The stability of an oscillon is not guaranteed by a conserved charge and its long lifetime is associated with an approximate adiabatic invariant [220, 216]. Early Universe oscillons have been recently studied in connection with primordial gravity waves [221] as well as baryogenesis [222].

For definiteness, we consider the model with a single inflaton field ϕ that has a canonical kinetic term, minimal coupling to Einstein gravity and a potential [223, 224, 218, 225]

$$V = \frac{m^2}{2}\phi^2 - \frac{\lambda}{4}\phi^4 + \frac{g^2}{6m^2}\phi^6 \ . \tag{5.1}$$

Here $\lambda > 0$ and for convenience, following the original studies, we take $\lambda, g, m/M_{pl} \ll 1$, where M_{pl} is the Planck mass. The model [223, 224, 218, 225] is inspired by a class of well motivated supergravity and string theories [226, 227, 218] and could be considered as a Taylor series expansion of a more general potential for some range of the scalar field. We assume that the density perturbations that seed cosmological structures are generated when the inflaton field has a much larger value, for which the shape of the potential is not necessarily

described by Eq. (5.1). After the inflationary phase, the inflaton begins to oscillate near the minimum of the potential as described by Eq. (5.1). At this time, the inflaton condensate fragments into oscillons.

A necessary condition for oscillon formation is that the potential is shallower than quadratic near the minimum (making the scalar self-interactions attractive). This is the case for $\lambda > 0$. For $(\lambda/g)^2 \ll 1$, the above potential admits "flat-top" oscillons, which are extremely stable on the cosmological time scales and for which the analytic description is known [223, 224, 218, 225].

5.3 Parametric Resonance

An initially homogeneous inflaton condensate can fragment into lumps, corresponding to oscillons. The inflaton self-resonance parametrically amplifies field fluctuations $\delta\phi_k$ in some band of wave-numbers k around the background field $\overline{\phi}$. This can be analytically investigated through Floquet analysis, where the most unstable modes behave as $\delta\phi_k(t) \propto e^{\mu_k t} P(t)$, with μ_k denoting the Floquet exponent and $P(t)$ a periodic function. In an expanding background significant amplification of fluctuations requires $\mu_k(a)/H \gg 1$, where $a(t)$ is the cosmic scale factor and $H = H_i/\sqrt{a^3}$ is the Hubble parameter at the bottom of potential. At fragmentation $H_i \simeq \sqrt{\lambda/10g^2}(m/M_{pl})m$ and $a_i = 1$. The amplification condition translates to [223]

$$\frac{\mu_k(a)}{H} = \frac{M_{pl}}{m}\Big(\frac{\lambda^{3/2}}{g}\Big)\Big[\sqrt{\frac{9}{4}\frac{\tilde{k}^2}{a^2}\Big(1-\frac{1}{a^3}\Big) - \Big(\frac{\tilde{k}^4}{a}\Big)}\Big] \gg 1 \ , \tag{5.2}$$

where $\tilde{k} = (g/\lambda m)k$, with k being related to the physical wavenumber via $k = a\, k_p$. The total amplification of fluctuations as they pass through the instability band is found by integrating over the Floquet exponent as

$$\delta\phi_k(a) \sim \frac{1}{\sqrt{2\omega_k}}\frac{1}{a^{3/2}} e^{\beta f(\tilde{k},a)} \ , \tag{5.3}$$

where

$$f(\tilde{k},a)=\sqrt{\frac{5}{2}}\int_C d\log\overline{a}\Big[\tilde{k}\sqrt{\frac{9}{10\overline{a}^2}\Big(1-\frac{1}{\overline{a}^3}\Big)-\frac{\tilde{k}^2}{\overline{a}}}\Big] \tag{5.4}$$

and $C=\frac{a^3-1}{a^4}>\frac{10}{9}\tilde{k}^2$, $\beta=\sqrt{\lambda}(\lambda/g)(M_{pl}/m)$ and $\omega_k^2\simeq k^2+m^2$. Since $\beta\sim\mu/H$, we are interested in the $\beta\gg 1$ regime.

The condition [223] for formation of oscillons from amplified perturbations can be formulated as $k^{3/2}\delta\phi\sim\overline{\phi}$. The average number density of oscillons can then be estimated as $\overline{n}\sim(k_{nl}/2\pi)^3/a^3$, where $k_{nl}\sim\beta^{-1/5}(\lambda/g)m$ label the modes that become non-linear the earliest. While the model supports several distinct oscillon populations, we focus on the flat-top oscillons due to their stability. Unlike the usual Gaussian-profile oscillons, they possess an approximately uniform core density of $\rho_c\simeq m^4(9\lambda/20g^2)$ [224]. Taking the characteristic radius of oscillons to be $R\sim\pi/k_{nl}$, we can estimate their energy as

$$E\sim\frac{4\pi\rho_c R^3}{3}\simeq\frac{3\pi^4m^4}{5k_{nl}^3}\Big(\frac{\lambda}{g^2}\Big)\,. \tag{5.5}$$

The above provides $\overline{n}(E)$ through k_{nl} substitution.

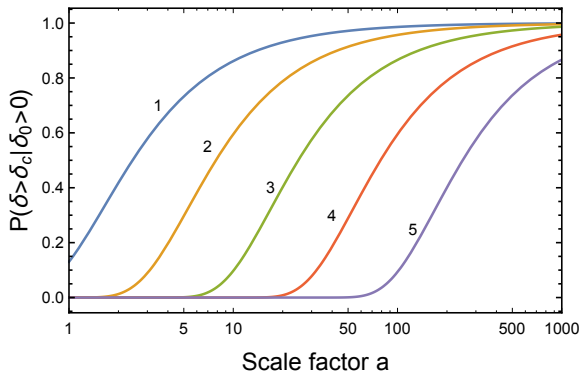

Figure 5.1: Fraction of super-critical overdensities as a function of the scale factor $a(t)$. Results are shown for several different volumes, which are expressed in terms of the Hubble horizon as $V/V_H=3\times10^{-5}$, 3×10^{-4}, 3×10^{-3} , 3×10^{-2} , 3×10^{-1} and labeled "1", "2", "3", "4" and "5", respectively. The values of the input parameters $(\lambda/g)^2=0.2$ and $\beta=56.1$ correspond to those of Model A.

5.4 Density Perturbations

Given an average number density $\overline{n}$ of uniformly distributed objects, the probability of finding N objects within a volume V follows the Poisson distribution

$$P_N(N) = \frac{(\overline{n}V)^N}{N!} e^{-\overline{n}V} \ . \tag{5.6}$$

The total mass of a cluster of oscillons is $M = NE$. Hence, the probability distribution of oscillon cluster mass is given by $P_M(M) = \sum_N P_N(N)\delta(M - NE)$. The delta-function can be eliminated through a Fourier transform

$$\tilde{P}_M(\mu) = \int dM\, P_M(M)\, e^{iM\mu} = e^{\overline{n}V(e^{iE\mu}-1)} \ , \tag{5.7}$$

followed by an inverse transform

$$P_M(M) = \frac{1}{2\pi} \int d\mu\, e^{-iM\mu}\, e^{\overline{n}V(e^{iE\mu}-1)} \ . \tag{5.8}$$

An approximate analytic non-integral form of Eq. (5.8) can be found through the method of steepest descent. The resulting expression is

$$P_\eta(\eta) = \frac{1}{\sqrt{2\pi\beta^{3/5}\eta}} e^{\beta^{-3/5}[\eta(1-\ln\{(2\pi)^3\eta/v\})-v/(2\pi)^3]} \ , \tag{5.9}$$

where $v = V(\lambda m/g)^3 = V[M_{pl}(\lambda/g)(m/M_{pl})]^3$ and $\eta = M/E_0$, with $E_0 = (3\pi^4/5)[M_{pl}(\lambda/g)/\beta^2(m/M_{pl})]$, denote the rescaled dimensionless volume and mass, respectively.

Using $P_\eta(\eta)$ we can now calculate the distribution of the initial density contrasts δ_0. In terms of η, δ_0 is

$$\delta_0 = \frac{\delta\rho}{\overline{\rho}} = \frac{\rho - \overline{\rho}}{\overline{\rho}} = \frac{M/V - \overline{\rho}}{\overline{\rho}} = (2\pi)^3\Big(\frac{\eta}{v}\Big) - 1 \ , \tag{5.10}$$

where $\overline{\rho} = \overline{n}\, E = E_0(\lambda m/g)^3/(2\pi)^3$ denotes the average background energy density of oscillons. The η prefactor can be restated in terms of $\overline{n}$ as $(\overline{\rho}V/E_0) \simeq (\lambda m/g)^3 V/(2\pi)^3 =$

$\beta^{-3/5}\overline{n}V$. The probability distribution of δ_0 is then

$$P_{\delta_0}(\delta_0) = P_\eta(\eta)\left|\frac{d\eta}{d\delta_0}\right| = \frac{v}{(2\pi)^3}P_\eta\Big(\frac{v}{(2\pi)^3}[1+\delta_0]\Big)\ . \tag{5.11}$$

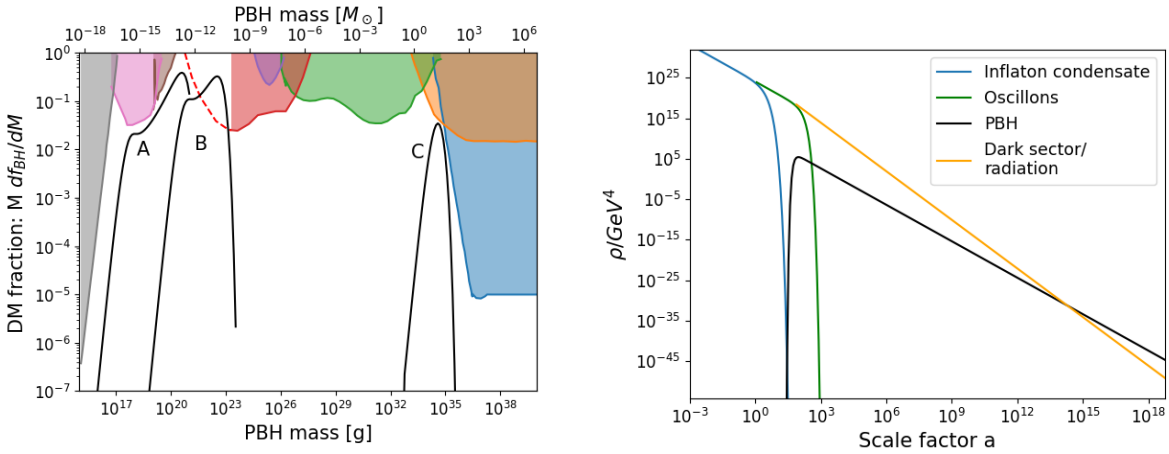

Figure 5.2: [Left] DM fraction in primordial black holes. Fits for parameter choices corresponding to Model A, B, C are shown. Constraints from extragalactic γ-rays from BH evaporation [182] (EGγ), femto-lensing [174] (FL), white dwarf abundance [228] (WD), Kepler star milli/micro- lensing [177] (K), Subaru HSC micro-lensing [90] (HSC) and MACHO/EROS/ OGLE micro-lensing [178] (ML) are displayed. Dashed line indicates that HSC constraints [88] are expected to be weaker than reported when PBH Schwarzschild radius becomes smaller than the wavelength of light [185, 184]. [Right] Evolution of cosmological density for parameters of Model A. Contributions from the un-fragmented inflaton, oscillons, PBHs as well as the radiation sector are shown.

The initial overdensities evolve due to gravitational self-attraction and grow according to the scale factor during the oscillon matter-dominated era as $\delta(t) = \delta_0 a(t) = \delta_0(t/t_0)^{2/3}$. Once overdensities δ exceed the critical threshold $\delta_c \sim 1$, regions start collapsing and forming black holes. Using Eq. (5.10) to exchange δ_c for η_c, we obtain the condition for η to be super-critical

$$\eta \geq \eta_c(a, V) = \frac{\overline{\rho}V}{E_0}\left(\frac{\delta_c}{a}+1\right)\ . \tag{5.12}$$

The total fraction of super-critical overdensities as a function of scale factor a can be found through integration

$$P(\delta \geq \delta_c) = \int_{\delta_c=1}^{\infty}\frac{d\delta}{a}P_{\delta_0}(\delta/a). \tag{5.13}$$

In Figure 5.1 we display this fraction for several different volume values. As can be seen,

already within a few a from the time of fragmentation the amount of super-critical regions becomes significant.

5.5 Formation of black holes

Not all super-critical regions result in a black hole. Unlike the radiation-era PBH formation [229], absence of pressure gradient in the matter-dominated era greatly enhances black hole production [169]. On the other hand, non-spherical density anisotropies now play a dominant role with final stages of collapse being described by a "Zel'dovich pancake" [230], whose parameter distribution can found in [231]. Using Thorne's hoop conjecture [232] as a requirement for formation of the black hole horizon, PBH production was recently reanalyzed in [233] (see discussion in text for comparison with [169]). The probability for a super-critical overdensity region to result in a black hole is given by

$$B(M) \simeq 0.05556\,\delta^5 \left(\frac{M}{\overline{M}(V_H)}\right)^{10/3} , \tag{5.14}$$

where $\overline{M}(V_H) = (4\pi/3)\overline{\rho}/H_i^3$ denotes the average mass in the Hubble horizon volume $V_H(t) = (4\pi/3)t^3$ at fragmentation, with $t = 1/H$. We have further checked that including the effects of PBH spins [234], relevant for small overdensities, will not significantly alter our results.

Model	β	$(\lambda/g)^2$	a_R	m_ϕ (GeV)	$\overline{\phi}_{\rm frag}$ (GeV)	H_i (GeV)	Γ_ϕ (GeV)	T_R (GeV)	$f_{\rm PBH}$
A	56.1	0.2	70	$5{\cdot}10^{-5}$	$6.7{\cdot}10^{15}$	$4.6{\cdot}10^{-7}$	$1.2{\cdot}10^{-10}$	$6.6{\cdot}10^{3}$	1.0
B	35.5	0.2	20	$9{\cdot}10^{-8}$	$1.1{\cdot}10^{16}$	$1.3{\cdot}10^{-9}$	$2.2{\cdot}10^{-12}$	$9.0{\cdot}10^{2}$	1.0
C	10.7	0.2	2	$1{\cdot}10^{-20}$	$5.3{\cdot}10^{16}$	$7.2{\cdot}10^{-22}$	$3.8{\cdot}10^{-23}$	$3.8{\cdot}10^{-3}$	$5.1{\cdot}10^{-2}$

Table 5.1: Parameter sets for three specific model realizations (Model A, B, C). In Models A, B PBHs can account for all of the DM, while model C allows for PBHs to contribute to the observed LIGO black hole merger events. Vertical double line divides the input quantities [left-side] β, $(\lambda/g)^2$, reheating time $a_R = a(T_R)$, inflaton mass m_ϕ and the derived quantities [right-side]: inflaton VEV at fragmentation $\overline{\phi}_{\rm frag}$, initial Hubble rate H_i, inflaton decay rate Γ_ϕ, reheating temperature T_R and the fraction of DM in PBHs $f_{\rm PBH}$.

At some scale factor a_R the oscillon matter-dominated era ends and the Universe is

reheated, entering the radiation-dominated phase. Specifying the energy density of the overdensities as $\rho = M/V = E_0\eta/V$, the PBH spectrum at a_R is given by

$$\frac{d\langle\rho_{\rm PBH}\rangle}{d\eta} = \int_{V_{\rm min}}^{V_{\rm max}} \frac{dV}{V}\left(B(\eta)\frac{E_0\eta}{V}\right) P_\eta(\eta) \times \theta[\eta - \eta_c(a_R, V)]\theta\left[\rho_0 - \frac{E_0\eta}{V}\right] , \tag{5.15}$$

where $\theta[x]$ is the Heaviside step function and $V_{\rm min}$, $V_{\rm max}$ are the average volume of a single oscillon and the Hubble horizon volume, respectively. The first step function selects supercritical regions. The second step function imposes energy conservation by requiring that an overdensity doesn't exceed the inflaton energy density, assuming that both have the same volume. The inflaton energy density ρ_0 at the bottom of its potential can be found from the mass term $\rho_0 a_i^3 = (1/2)m^2\overline{\phi}_i$, where $\overline{\phi}_i = \sqrt{3\lambda/5g^2}m$. A similar relation can be obtained directly from the Friedmann equations.

5.6 Evolution to present day

In order to get the present day distribution we must redshift the results obtained at fragmentation time. The redshift factor $(a_F/a_R) = g_{*S}^{1/3}(T_F)T_F/g_{*S}^{1/3}(T_R)T_R$ accounts for evolution from T_R (defined by $\rho_R(T_R) = (\pi^2/30)g_*(T_R)T_R^4$) to $T_0 = 2.7\text{K} = 2.3$ meV. Here, g_* denotes the relevant number of relativistic degrees of freedom. Reverting from η back to M, the fraction of DM residing in PBHs is then

$$\frac{df_{PBH}}{dM} = \frac{1}{\rho_{DM}a^3}\frac{d\langle\rho_{PBH}\rangle}{dM} , \tag{5.16}$$

where ρ_{DM} is the present-day DM density and the $1/a^3$ factor accounts for the redshift In Figure 5.2 we display the fraction of PBHs as DM for several specific parameter sets (denoted as "Model A", "B", "C") along with the current experimental constraints. Model A, B correspond to the region where PBHs can make up all of the DM, while Model C covers the region where PBHs can contribute to the observed LIGO black hole merger events

[155, 157, 209]. Exact values of the parameters, including both the input and the derived quantities, can be found in Table 5.1. We note that Model C is phenomenologically not viable; the relevant parameters are shown for completeness.

In Figure 5.2 we display the cosmological history of the setup, showing energy density evolution of the inflaton, oscillons, PBHs as well as radiation from reheating. During inflation, the inflaton dominates the Universe. As the inflaton settles at the bottom of potential the Universe becomes matter-dominated with the density scaling as a^{-3}. After fragmentation of the inflaton into oscillons and PBH formation the Universe is reheated, becoming radiation-dominated with the density scaling as a^{-4}. At redshift $z \approx 3600$ dark matter in the form of PBHs, whose density scales also as a^{-3}, overtakes the radiation contribution, and the Universe again enters matter-dominated regime. Unlike the case of Q-balls [142, 158], there is no intermediate radiation-dominated era before the fragmentation time in our setup, since oscillons form directly from the inflaton during the early stages of reheating.

We further comment on two important cosmological aspects of the setting, the inflationary phase and reheating. Taken at face value, the potential of Eq. (5.1) produces unphysical perturbation spectrum during inflation due to the dominance of ϕ^6 term (see [218] for discussion). However, the field value $\overline{\phi}$ at the bottom of potential is far below the Planck scale that sets the initial inflaton displacement. Hence, our region of interest where inflaton oscillates near the potential minimum is decoupled from the large values that determine the inflationary phase. In this work we remain agnostic regarding the exact shape of the potential and the early Universe dynamics. We focus on the effective potential at a relatively small vacuum expectation value (VEV), well below the values that are relevant for structure formation.

5.7 Reheating

The Universe is reheated from oscillon decay. If PBHs are to constitute a significant fraction of DM, the inflaton must be very light, and the reheating temperature is very low (see Table 5.1). To avoid affecting the Big Bang nucleosynthesis (BBN), reheating should occur above $T \gtrsim 4$ MeV scale (e.g. [235]). While it is commonly assumed that the Universe

was reheated to a much higher temperature, a cosmological history with ∼MeV reheating is possible and is consistent with observations [236, 237]. Neglecting the oscillon quantum decay [238], the allowed direct inflaton decay channels are limited by the total invariant mass. The simplest decay mode is to photons $\phi \to \gamma\gamma$, proceeding through an effective $(g_{\gamma\gamma}/4)F_{\mu\nu}F^{\mu\nu}\phi$ operator, where $F_{\mu\nu}$ is the electromagnetic field strength tensor and $g_{\gamma\gamma}$ is the coupling. The relevant decay rate is given by $\Gamma_{\phi\to\gamma\gamma} = (g^2_{\gamma\gamma}/64\pi)m^3_\phi$. However, axion-like particle searches already strongly constrain this channel [239, 240]. Thus, without an extended dark sector, Model C is not viable. In a more complicated model, the reheating may be possible if the inflaton decays into some dark sector particles, which produce the Standard Model degrees of freedom via mixing (e.g. [241, 242]). Generating the matter-antimatter asymmetry in a low-reheating scenario also presents a model building challenge.

In summary, inflaton fragmentation into oscillons can lead to formation of primordial black holes in a single-field inflation model or other models that admit oscillon solutions. This novel production mechanism can generate a sufficient density of PBHs to account for all or part of dark matter. It is also possible that solar-mass black holes can be produced this way, but the required mass of the inflaton is very small, and the need for reheating and baryogenesis will lead to more complicated models.

5.8 Acknowledgments

This work was supported by the U.S. Department of Energy Grant No. DE-SC0009937 A.K. was also supported by the World Premier International Research Center Initiative (WPI), MEXT, Japan.

REFERENCES

[1] Fritz Zwicky. On the masses of nebulae and of clusters of nebulae. *Astrophys. J.*, 86:217, October 1937.

[2] Vera Rubin and Kent W. Ford. Rotation of the andromeda nebula from a spectroscopic survey of emission regions. *Astrophys. J.*, 159:379, February 1970.

[3] Jaco de Swart, Gianfranco Bertone, and Jeroen van Dongen. How Dark Matter Came to Matter. 2017. [Nature Astron.1,0059(2017)].

[4] Gianfranco Bertone, Dan Hooper, and Joseph Silk. Particle dark matter: evidence, candidates and constraints. *Physics Reports*, 405(5):279 – 390, 2005.

[5] Vera C. Rubin, W. Kent Ford Jr., and Norbert Thonnard. Rotational properties of 21 sc galaxies with a large range of luminosities and radii, from ngc 4605 (r = 4 kpc) to ugc 2885 (r = 122 kpc).

[6] Julio F. Navarro, Carlos S. Frank, and Simon D. M. White. The structure of cold dark matter halos. *Astrophys. J.*, 462:563–575, May 1996.

[7] Dan P. Clemens. Massachusetts-stony brook galactic plane co survey: The galactic disk rotation curve. *Astrophys. J.*, 295:422–436, August 1985.

[8] Michel Fich, Leo Blitz, and Antony A. Stark. The rotation curve of the milky way to $2r_0$. *Astrophys. J.*, 342:272–284, July 1989.

[9] N. W. Halverson, E. M. Leitch, C. Pryke, J. Kovac, J. E. Carlstrom, W. L. Holzapfel, M. Dragovan, J. K. Cartwright, B. S. Mason, S. Padin, T. J. Pearson, A. C. S. Readhead, and M. C. Shepherd. Degree angular scale interferometer first results: A measurement of the cosmic microwave background angular power spectrum. *The Astrophysical Journal*, 568(1):38, 2002.

[10] C. B. Netterfield, P. A. R. Ade, J. J. Bock, J. R. Bond, J. Borrill, A. Boscaleri, K. Coble, C. R. Contaldi, B. P. Crill, P. de Bernardis, P. Farese, K. Ganga, M. Giacometti, E. Hivon, V. V. Hristov, A. Iacoangeli, A. H. Jaffe, W. C. Jones, A. E. Lange, L. Martinis, S. Masi, P. Mason, P. D. Mauskopf, A. Melchiorri, T. Montroy, E. Pascale, F. Piacentini, D. Pogosyan, F. Pongetti, S. Prunet, G. Romeo, J. E. Ruhl, and F. Scaramuzzi. A measurement by boomerang of multiple peaks in the angular power spectrum of the cosmic microwave background. *The Astrophysical Journal*, 571(2):604, 2002.

[11] Wayne Hu and Martin White. Acoustic signatures in the cosmic microwave background. *The Astrophysical Journal*, 471(1):30, 1996.

[12] Will J. Percival, Beth A. Reid, Daniel J. Eisenstein, Neta A. Bahcall, Tamas Budavari, Joshua A. Frieman, Masataka Fukugita, James E. Gunn, Željko Ivezić, Gillian R. Knapp, Richard G. Kron, Jon Loveday, Robert H. Lupton, Timothy A. McKay, Avery

Meiksin, Robert C. Nichol, Adrian C. Pope, David J. Schlegel, Donald P. Schneider, David N. Spergel, Chris Stoughton, Michael A. Strauss, Alexander S. Szalay, Max Tegmark, Michael S. Vogeley, David H. Weinberg, Donald G. York, and Idit Zehavi. Baryon acoustic oscillations in the sloan digital sky survey data release 7 galaxy sample. *Monthly Notices of the Royal Astronomical Society*, 401(4):2148–2168, 2010.

[13] Lauren Anderson, Eric Aubourg, Stephen Bailey, Dmitry Bizyaev, Michael Blanton, Adam S. Bolton, J. Brinkmann, Joel R. Brownstein, Angela Burden, Antonio J. Cuesta, Luiz A. N. da Costa, Kyle S. Dawson, Roland de Putter, Daniel J. Eisenstein, James E. Gunn, Hong Guo, Jean-Christophe Hamilton, Paul Harding, Shirley Ho, Klaus Honscheid, Eyal Kazin, David Kirkby, Jean-Paul Kneib, Antoine Labatie, Craig Loomis, Robert H. Lupton, Elena Malanushenko, Viktor Malanushenko, Rachel Mandelbaum, Marc Manera, Claudia Maraston, Cameron K. McBride, Kushal T. Mehta, Olga Mena, Francesco Montesano, Demetri Muna, Robert C. Nichol, Sebastián E. Nuza, Matthew D. Olmstead, Daniel Oravetz, Nikhil Padmanabhan, Nathalie Palanque-Delabrouille, Kaike Pan, John Parejko, Isabelle Pâris, Will J. Percival, Patrick Petitjean, Francisco Prada, Beth Reid, Natalie A. Roe, Ashley J. Ross, Nicholas P. Ross, Lado Samushia, Ariel G. Sánchez, David J. Schlegel, Donald P. Schneider, Claudia G. Scóccola, Hee-Jong Seo, Erin S. Sheldon, Audrey Simmons, Ramin A. Skibba, Michael A. Strauss, Molly E. C. Swanson, Daniel Thomas, Jeremy L. Tinker, Rita Tojeiro, Mariana Vargas Magaña, Licia Verde, Christian Wagner, David A. Wake, Benjamin A. Weaver, David H. Weinberg, Martin White, Xiaoying Xu, Christophe Yèche, Idit Zehavi, and Gong-Bo Zhao. The clustering of galaxies in the sdss-iii baryon oscillation spectroscopic survey: baryon acoustic oscillations in the data release 9 spectroscopic galaxy sample. *Monthly Notices of the Royal Astronomical Society*, 427(4):3435–3467, 2012.

[14] Douglas Clowe, Anthony Gonzalez, and Maxim Markevitch. Weak-lensing mass reconstruction of the interacting cluster 1e 0657–558: Direct evidence for the existence of dark matter. *The Astrophysical Journal*, 604(2):596, 2004.

[15] Nick Kaiser and Gordon Squires. Mapping the dark matter with weak gravitational lensing. *Astropys. J.*, 404:441–450, February 1993.

[16] David M. Wittman, J. Anthony Tyson, David Kirkman, Ian Dell'Antonio, and Gary Bernstein. Detection of weak gravitational lensing distortions of distant galaxies by cosmic dark matter at large scales. *Nature*, 405:143–148, May 2000.

[17] Tim M.P. Tait. Dark matter: Theoretical overview, 2016.

[18] Gerard Jungman, Marc Kamionkowski, and Kim Griest. Supersymmetric dark matter. *Phys. Rept.*, 267:195–373, 1996.

[19] M. Kamionkowski. WIMP and axion dark matter. In *High-energy physics and cosmology. Proceedings, Summer School, Trieste, Italy, June 2-July 4, 1997*, pages 394–411, 1997.

[20] Kim Griest. The Search for dark matter: WIMPs and MACHOs. 1993. [,413(1993)].

[21] Edward W. Kolb, Daniel J. H. Chung, and Antonio Riotto. WIMPzillas! *AIP Conf. Proc.*, 484(1):91–105, 1999. [,592(1999)].

[22] Frank Daniel Steffen. Dark Matter Candidates - Axions, Neutralinos, Gravitinos, and Axinos. *Eur. Phys. J.*, C59:557–588, 2009.

[23] Matthew Low and Lian-Tao Wang. Neutralino dark matter at 14 TeV and 100 TeV. *JHEP*, 08:161, 2014.

[24] R. D. Peccei and Helen R. Quinn. CP Conservation in the Presence of Instantons. *Phys. Rev. Lett.*, 38:1440–1443, 1977. [,328(1977)].

[25] R. D. Peccei. The Strong CP problem and axions. *Lect. Notes Phys.*, 741:3–17, 2008. [,3(2006)].

[26] John Preskill, Mark B. Wise, and Frank Wilczek. Cosmology of the invisible axion. *Physics Letters B*, 120(1):127 – 132, 1983.

[27] Wayne Hu, Rennan Barkana, and Andrei Gruzinov. Cold and fuzzy dark matter. *Phys. Rev. Lett.*, 85:1158–1161, 2000.

[28] Hsi-Yu Schive, Tzihong Chiueh, Tom Broadhurst, and Kuan-Wei Huang. Contrasting Galaxy Formation from Quantum Wave Dark Matter, ψDM, with ΛCDM, using Planck and Hubble Data. *Astrophys. J.*, 818(1):89, 2016.

[29] Alexander Kusenko. Solitons in the supersymmetric extensions of the standard model. *Phys. Lett.*, B405:108, 1997.

[30] Sidney Coleman. Q-balls. *Nuclear Physics B*, 262(2):263 – 283, 1985.

[31] Alexander Kusenko and Mikhail E. Shaposhnikov. Supersymmetric Q balls as dark matter. *Phys. Lett.*, B418:46–54, 1998.

[32] Joshua Eby, Chris Kouvaris, Niklas Grønlund Nielsen, and L. C. R. Wijewardhana. Boson Stars from Self-Interacting Dark Matter. *JHEP*, 02:028, 2016.

[33] Jae-weon Lee and In-gyu Koh. Galactic halos as boson stars. *Phys. Rev.*, D53:2236–2239, 1996.

[34] R. Sharma, S. Karmakar, and S. Mukherjee. Boson star and dark matter. *Submitted to: Gen. Rel. Grav.*, 2008.

[35] C.J. Hogan and M.J. Rees. Axion miniclusters. *Physics Letters B*, 205(2):228 – 230, 1988.

[36] Edward W. Kolb and Igor I. Tkachev. Axion miniclusters and Bose stars. *Phys. Rev. Lett.*, 71:3051–3054, 1993.

[37] Malcolm Fairbairn, David J. E. Marsh, Jérémie Quevillon, and Simon Rozier. Structure formation and microlensing with axion miniclusters. *Phys. Rev.*, D97(8):083502, 2018.

[38] Y. B. Zel'dovich and I. D. Novikov. The Hypothesis of Cores Retarded during Expansion and the Hot Cosmological Model. *Astronomicheskii Zhurnal*, 43:758, 1966.

[39] I. D. Novikov, A. G. Polnarev, A. A. Starobinskii, and I. B. Zeldovich. Primordial black holes. *Astronomy and Astrophysics*, 80:104–109, November 1979.

[40] B. J. Carr and S. W. Hawking. Black holes in the early universe. *Monthly Notices of the Royal Astronomical Society*, 168(2):399–415, 1974.

[41] Maxim Yu. Khlopov. Primordial black holes. *Research in Astronomy and Astrophysics*, 10(6):495, 2010.

[42] J. H. MacGibbon. Can planck-mass relics of evaporating black holes close the universe? *Nature*, 329:308–309, September 1987.

[43] Pisin Chen and Ronald J. Adler. Black hole remnants and dark matter. *Nuclear Physics B - Proceedings Supplements*, 124:103 – 106, 2003. Proceedings of the 5th International UCLA Symposium on Sources and Detection of Dark Matter and Dark Energy in the Universe.

[44] Scott Dodelson and Lawrence M. Widrow. Sterile neutrinos as dark matter. *Phys. Rev. Lett.*, 72:17–20, Jan 1994.

[45] Xiangdong Shi and George M. Fuller. New dark matter candidate: Nonthermal sterile neutrinos. *Phys. Rev. Lett.*, 82:2832–2835, Apr 1999.

[46] Lotty Ackerman, Matthew R. Buckley, Sean M. Carroll, and Marc Kamionkowski. Dark Matter and Dark Radiation. *Phys. Rev.*, D79:023519, 2009. [,277(2008)].

[47] Daniele S.M. Alves, Siavosh R. Behbahani, Philip Schuster, and Jay G. Wacker. Composite inelastic dark matter. *Physics Letters B*, 692(5):323 – 326, 2010.

[48] Nodoka Yamanaka, Sho Fujibayashi, Shinya Gongyo, and Hideaki Iida. Dark matter in the hidden gauge theory. 2014.

[49] Kimberly K. Boddy, Jonathan L. Feng, Manoj Kaplinghat, and Tim M. P. Tait. Self-interacting dark matter from a non-abelian hidden sector. *Phys. Rev. D*, 89:115017, Jun 2014.

[50] Amarjit Soni and Yue Zhang. Hidden SU(N) Glueball Dark Matter. *Phys. Rev.*, D93(11):115025, 2016.

[51] David E. Kaplan, Markus A. Luty, and Kathryn M. Zurek. Asymmetric dark matter. *Phys. Rev. D*, 79:115016, Jun 2009.

[52] Kalliopi Petraki and Raymond R. Volkas. Review of asymmetric dark matter. *Int. J. Mod. Phys.*, A28:1330028, 2013.

[53] F. Englert and R. Brout. Broken symmetry and the mass of gauge vector mesons. *Phys. Rev. Lett.*, 13:321–323, Aug 1964.

[54] Peter W. Higgs. Broken symmetries and the masses of gauge bosons. *Phys. Rev. Lett.*, 13:508–509, Oct 1964.

[55] G. S. Guralnik, C. R. Hagen, and T. W. B. Kibble. Global conservation laws and massless particles. *Phys. Rev. Lett.*, 13:585–587, Nov 1964.

[56] Steven Weinberg. A model of leptons. *Phys. Rev. Lett.*, 19:1264–1266, Nov 1967.

[57] Abdus Salam and J. C. Ward. Weak and electromagnetic interactions. *Il Nuovo Cimento (1955-1965)*, 11(4):568–577, Feb 1959.

[58] Sheldon L. Glashow. The renormalizability of vector meson interactions. *Nucl. Phys.*, 10:107–117, 1959.

[59] J. Bardeen, L. N. Cooper, and J. R. Schrieffer. Microscopic theory of superconductivity. *Phys. Rev.*, 106:162–164, Apr 1957.

[60] J. Bardeen, L. N. Cooper, and J. R. Schrieffer. Theory of superconductivity. *Phys. Rev.*, 108:1175–1204, Dec 1957.

[61] P. W. Anderson. Plasmons, gauge invariance, and mass. *Phys. Rev.*, 130:439–442, Apr 1963.

[62] Ian Affleck and Michael Dine. A new mechanism for baryogenesis. *Nuclear Physics B*, 249(2):361 – 380, 1985.

[63] Michael Dine, Lisa Randall, and Scott D. Thomas. Baryogenesis from flat directions of the supersymmetric standard model. *Nucl. Phys.*, B458:291–326, 1996.

[64] Sidney R. Coleman. Q Balls. *Nucl. Phys.*, B262:263, 1985. [Erratum: Nucl. Phys.B269,744(1986)].

[65] Kimyeong Lee, Jaime A. Stein-Schabes, Richard Watkins, and Lawrence M. Widrow. Gauged q balls. *Phys. Rev. D*, 39:1665–1673, Mar 1989.

[66] K. N. Anagnostopoulos, M. Axenides, E. G. Floratos, and N. Tetradis. Large gauged q balls. *Phys. Rev. D*, 64:125006, Nov 2001.

[67] Mikhail S. Volkov and Erik Wohnert. Spinning Q balls. *Phys. Rev.*, D66:085003, 2002.

[68] L. Campanelli and M. Ruggieri. Spinning Supersymmetric Q-balls. *Phys. Rev.*, D80:036006, 2009.

[69] REMO RUFFINI and SILVANO BONAZZOLA. Systems of self-gravitating particles in general relativity and the concept of an equation of state. *Phys. Rev.*, 187:1767–1783, Nov 1969.

[70] P. Jetzer. Boson stars. *Phys. Rep.*, 220:163–227, November 1992.

[71] P. Jetzer and J. J. van der Bij. Charged boson stars. *Physics Letters B*, 227:341–346, August 1989.

[72] J. Barranco and A. Bernal. Constraining scalar field properties with boson stars as black hole mimickers. *AIP Conf. Proc.*, 1396:171–175, 2011.

[73] Edward Seidel and Wai-Mo Suen. Oscillating soliton stars. *Phys. Rev. Lett.*, 66:1659–1662, Apr 1991.

[74] Philippe Jetzer and David Scialom. On the stability of real scalar boson stars. In *Recent developments in theoretical and experimental general relativity, gravitation, and relativistic field theories. Proceedings, 8th Marcel Grossmann meeting, MG8, Jerusalem, Israel, June 22-27, 1997. Pts. A, B*, pages 1630–1632, 1997.

[75] L. Arturo Urena-Lopez. Oscillatons revisited. *Class. Quant. Grav.*, 19:2617–2632, 2002.

[76] Scott H. Hawley and Matthew W. Choptuik. Numerical evidence for 'multi - scalar stars'. *Phys. Rev.*, D67:024010, 2003.

[77] Edward W. Kolb and Igor I. Tkachev. Nonlinear axion dynamics and formation of cosmological pseudosolitons. *Phys. Rev.*, D49:5040–5051, 1994.

[78] Eric Braaten, Abhishek Mohapatra, and Hong Zhang. Dense Axion Stars. *Phys. Rev. Lett.*, 117(12):121801, 2016.

[79] I. I. Tkachev. Fast Radio Bursts and Axion Miniclusters. *JETP Lett.*, 101(1):1–6, 2015. [Pisma Zh. Eksp. Teor. Fiz.101,no.1,3(2015)].

[80] Aiichi Iwazaki. Axion stars and fast radio bursts. *Phys. Rev. D*, 91:023008, Jan 2015.

[81] Stuart Raby. Axion star collisions with Neutron stars and Fast Radio Bursts. *Phys. Rev.*, D94(10):103004, 2016.

[82] Stephen Hawking. Gravitationally collapsed objects of very low mass. *Mon. Not. Roy. Astron. Soc.*, 152:75, 1971.

[83] Bernard J. Carr and S. W. Hawking. Black holes in the early Universe. *Mon. Not. Roy. Astron. Soc.*, 168:399–415, 1974.

[84] Volodymyr Takhistov. Positrons from Primordial Black Hole Microquasars and Gamma-ray Bursts. 2017.

[85] D. B. Cline. Do Very Short Gamma Ray Bursts Originate from Primordial Black Holes? Review. *International Journal of Astronomy and Astrophysics*, 1:164–172, 2011.

[86] Daniel Baumann, Paul J. Steinhardt, and Neil Turok. Primordial Black Hole Baryogenesis. 2007.

[87] George M. Fuller, Alexander Kusenko, and Volodymyr Takhistov. Primordial Black Holes and r-Process Nucleosynthesis. *Phys. Rev. Lett.*, 119(6):061101, 2017.

[88] Masahiro Takada. talk presented at Focus Week on Primordial Black Holes, Kavli IPMU, Chiba, Japan, 13-17 November 2017.

[89] Andrey Katz, Joachim Kopp, Sergey Sibiryakov, and Wei Xue. Femtolensing by Dark Matter Revisited. *Submitted to: JCAP*, 2018.

[90] Hiroko Niikura et al. Microlensing constraints on $10^{-10}M_{\odot}$-scale primordial black holes from high-cadence observation of M31 with Hyper Suprime-Cam. 2017.

[91] Eric Cotner. Collisional interactions between self-interacting nonrelativistic boson stars: Effective potential analysis and numerical simulations. *Phys. Rev.*, D94(6):063503, 2016.

[92] Rosemary F. G. Wyse and Gerard Gilmore. Observed Properties of Dark Matter on Small Spatial Scales. *IAU Symp.*, 244:44–52, 2008.

[93] J. S. Bullock. Notes on the Missing Satellites Problem. *ArXiv e-prints*, September 2010.

[94] Andrew Pontzen and Fabio Governato. Cold dark matter heats up. *Nature*, 506:171–178, 2014.

[95] Oliver D. Elbert, James S. Bullock, Shea Garrison-Kimmel, Miguel Rocha, Jose Oñorbe, and Annika H. G. Peter. Core formation in dwarf haloes with self-interacting dark matter: no fine-tuning necessary. *Mon. Not. Roy. Astron. Soc.*, 453(1):29–37, 2015.

[96] Scott W. Randall, Maxim Markevitch, Douglas Clowe, Anthony H. Gonzalez, and Marusa Bradac. Constraints on the Self-Interaction Cross-Section of Dark Matter from Numerical Simulations of the Merging Galaxy Cluster 1E 0657-56. *Astrophys. J.*, 679:1173–1180, 2008.

[97] Ivone F. M. Albuquerque, Carlos Pérez de Los Heros, and Denis S. Robertson. Constraints on self interacting dark matter from IceCube results. *JCAP*, 1402:047, 2014.

[98] Joseph F. Hennawi and Jeremiah P. Ostriker. Observational constraints on the self interacting dark matter scenario and the growth of supermassive black holes. *Astrophys. J.*, 572:41, 2002.

[99] Jae-Weon Lee, Sooil Lim, and Dale Choi. BEC dark matter can explain collisions of galaxy clusters. 2008.

[100] Alan H. Guth, Mark P. Hertzberg, and C. Prescod-Weinstein. Do Dark Matter Axions Form a Condensate with Long-Range Correlation? *Phys. Rev.*, D92(10):103513, 2015.

[101] Peter Svrcek and Edward Witten. Axions In String Theory. *JHEP*, 06:051, 2006.

[102] Alexander Kusenko, Lee Loveridge, and Mikhail Shaposhnikov. Supersymmetric dark matter Q-balls and their interactions in matter. *Phys. Rev.*, D72:025015, 2005.

[103] Alexander Kusenko and Paul J. Steinhardt. Q ball candidates for selfinteracting dark matter. *Phys. Rev. Lett.*, 87:141301, 2001.

[104] C. Alcock et al. The MACHO project: Microlensing results from 5.7 years of LMC observations. *Astrophys. J.*, 542:281–307, 2000.

[105] C. Afonso et al. Limits on galactic dark matter with 5 years of EROS SMC data. *Astron. Astrophys.*, 400:951–956, 2003.

[106] Ł. Wyrzykowski, S. Kozłowski, J. Skowron, V. Belokurov, M. C. Smith, A. Udalski, M. K. Szymański, M. Kubiak, G. Pietrzyński, I. Soszyński, and O. Szewczyk. The OGLE view of microlensing towards the Magellanic Clouds - II. OGLE-II Small Magellanic Cloud data. *Mon. Not. Roy. Astron. Soc.*, 407:189–200, September 2010.

[107] T. D. Lee and Y. Pang. Nontopological solitons. *Phys. Rep.*, 221:251–350, November 1992.

[108] R.K. Pathria and P.D. Beale. *Statistical Mechanics*. Elsevier Science, 1996.

[109] P.-H. Chavanis. Mass-radius relation of Newtonian self-gravitating Bose-Einstein condensates with short-range interactions. I. Analytical results. *Phys. Rev.* ***D***, 84(4):043531, August 2011.

[110] David J. Kaup. Klein-gordon geon. *Phys. Rev.*, 172:1331–1342, Aug 1968.

[111] Monica Colpi, Stuart L. Shapiro, and Ira Wasserman. Boson stars: Gravitational equilibria of self-interacting scalar fields. *Phys. Rev. Lett.*, 57:2485–2488, Nov 1986.

[112] M. Membrado, A. F. Pacheco, and J. Sañudo. Hartree solutions for the self-yukawian boson sphere. *Phys. Rev. A*, 39:4207–4211, Apr 1989.

[113] George B Arfken and Hans J Weber. *Mathematical methods for physicists; 3rd ed.* Academic Press, Orlando, FL, 1985.

[114] David J. E. Marsh and Ana-Roxana Pop. Axion dark matter, solitons and the cusp–core problem. *Mon. Not. Roy. Astron. Soc.*, 451(3):2479–2492, 2015.

[115] Irene M Moroz, Roger Penrose, and Paul Tod. Spherically-symmetric solutions of the schrödinger-newton equations. *Classical and Quantum Gravity*, 15(9):2733, 1998.

[116] Argelia Bernal and F. Siddhartha Guzmán. Scalar field dark matter: Head-on interaction between two structures. *Phys. Rev. D*, 74:103002, Nov 2006.

[117] C. Palenzuela, I. Olabarrieta, L. Lehner, and Steven L. Liebling. Head-on collisions of boson stars. *Phys. Rev.*, D75:064005, 2007.

[118] C. Palenzuela, L. Lehner, and Steven L. Liebling. Orbital Dynamics of Binary Boson Star Systems. *Phys. Rev.*, D77:044036, 2008.

[119] Eniko J. M. Madarassy and Viktor T. Toth. Evolution and dynamical properties of Bose-Einstein condensate dark matter stars. *Phys. Rev.*, D91(4):044041, 2015.

[120] Hsi-Yu Schive, Ming-Hsuan Liao, Tak-Pong Woo, Shing-Kwong Wong, Tzihong Chiueh, Tom Broadhurst, and W-Y. Pauchy Hwang. Understanding the core-halo relation of quantum wave dark matter from 3d simulations. *Phys. Rev. Lett.*, 113:261302, Dec 2014.

[121] Eric Cotner and Alexander Kusenko. Astrophysical constraints on dark-matter Q-balls in the presence of baryon-violating operators. *Phys. Rev. D*, 94, Dec 2016.

[122] Tony Gherghetta, Christopher F. Kolda, and Stephen P. Martin. Flat directions in the scalar potential of the supersymmetric standard model. *Nucl. Phys.*, B468:37–58, 1996.

[123] G. R. Dvali, Alexander Kusenko, and Mikhail E. Shaposhnikov. New physics in a nutshell, or Q ball as a power plant. *Phys. Lett.*, B417:99–106, 1998.

[124] Michael Dine and Alexander Kusenko. The Origin of the matter - antimatter asymmetry. *Rev. Mod. Phys.*, 76:1, 2003.

[125] Alexander Kusenko, Vadim Kuzmin, Mikhail Shaposhnikov, and P. G. Tinyakov. Experimental signatures of supersymmetric dark-matter Q-balls. *Phys. Rev. Lett.*, 80:3185–3188, Apr 1998.

[126] Kari Enqvist and John McDonald. Q balls and baryogenesis in the MSSM. *Phys. Lett.*, B425:309–321, 1998.

[127] S. Kasuya and M. Kawasaki. Q ball formation through Affleck-Dine mechanism. *Phys. Rev.*, D61:041301, 2000.

[128] Kari Enqvist and Anupam Mazumdar. Cosmological consequences of MSSM flat directions. *Phys. Rept.*, 380:99–234, 2003.

[129] Jeong-Pyong Hong, Masahiro Kawasaki, and Masaki Yamada. Charged q-ball dark matter from b and l direction. *Journal of Cosmology and Astroparticle Physics*, 2016(08):053, 2016.

[130] Shinta Kasuya, Masahiro Kawasaki, and Tsutomu T. Yanagida. IceCube potential for detecting Q-ball dark matter in gauge mediation. *PTEP*, 2015(5):053B02, 2015.

[131] A. D. Sakharov. Violation of CP Invariance, C Asymmetry, and Baryon Asymmetry of the Universe. *Soviet Journal of Experimental and Theoretical Physics Letters*, 5:24, January 1967.

[132] Masahiro Kawasaki, Kenichiro Konya, and Fuminobu Takahashi. Q-ball instability due to U(1) breaking. *Phys. Lett.*, B619:233–239, 2005.

[133] Alexander Kusenko, Lee C. Loveridge, and Mikhail Shaposhnikov. Astrophysical bounds on supersymmetric dark-matter Q-balls. *JCAP*, 0508:011, 2005.

[134] Alexander Kusenko, Mikhail E. Shaposhnikov, P. G. Tinyakov, and Igor I. Tkachev. Star wreck. *Phys. Lett.*, B423:104–108, 1998.

[135] Shinta Kasuya and Masahiro Kawasaki. Baryogenesis from the gauge-mediation type Q-ball and the new type of Q-ball as the dark matter. *Phys. Rev.*, D89(10):103534, 2014.

[136] Kari Enqvist and John McDonald. B - ball baryogenesis and the baryon to dark matter ratio. *Nucl. Phys.*, B538:321–350, 1999.

[137] A. Cohen, S. Coleman, H. Georgi, and A. Manohar. The evaporation of Q-balls. *Nuclear Physics B*, 272:301–321, July 1986.

[138] S. S. Clark. Particle creation from Q-balls. *Nuclear Physics B*, 756:38–70, November 2006.

[139] Masahiro Kawasaki and Masaki Yamada. Q ball Decay Rates into Gravitinos and Quarks. *Phys. Rev.*, D87(2):023517, 2013.

[140] J. Arafune, T. Yoshida, S. Nakamura, and K. Ogure. Experimental bounds on masses and fluxes of nontopological solitons. *Phys. Rev.*, D62:105013, 2000.

[141] Ian M. Shoemaker and Alexander Kusenko. The Ground states of baryoleptonic Q-balls in supersymmetric models. *Phys. Rev.*, D78:075014, 2008.

[142] Eric Cotner and Alexander Kusenko. Primordial black holes from scalar field evolution in the early universe. *Phys. Rev.*, D96(10):103002, 2017.

[143] Y. B. Zel'dovich and I. D. Novikov. The Hypothesis of Cores Retarded during Expansion and the Hot Cosmological Model. *Sov. Astron.*, 10:602, February 1967.

[144] Juan Garcia-Bellido, Andrei D. Linde, and David Wands. Density perturbations and black hole formation in hybrid inflation. *Phys. Rev.*, D54:6040–6058, 1996.

[145] M. Yu. Khlopov. Primordial Black Holes. *Res. Astron. Astrophys.*, 10:495–528, 2010.

[146] Paul H. Frampton, Masahiro Kawasaki, Fuminobu Takahashi, and Tsutomu T. Yanagida. Primordial Black Holes as All Dark Matter. *JCAP*, 1004:023, 2010.

[147] Masahiro Kawasaki, Alexander Kusenko, and Tsutomu T. Yanagida. Primordial seeds of supermassive black holes. *Phys. Lett.*, B711:1–5, 2012.

[148] Masahiro Kawasaki, Alexander Kusenko, Yuichiro Tada, and Tsutomu T. Yanagida. Primordial black holes as dark matter in supergravity inflation models. *Phys. Rev.*, D94(8):083523, 2016.

[149] Bernard Carr, Florian Kuhnel, and Marit Sandstad. Primordial Black Holes as Dark Matter. *Phys. Rev.*, D94(8):083504, 2016.

[150] Keisuke Inomata, Masahiro Kawasaki, Kyohei Mukaida, Yuichiro Tada, and Tsutomu T. Yanagida. Inflationary primordial black holes for the LIGO gravitational wave events and pulsar timing array experiments. 2016.

[151] Keisuke Inomata, Masahiro Kawasaki, Kyohei Mukaida, Yuichiro Tada, and Tsutomu T. Yanagida. Inflationary Primordial Black Holes as All Dark Matter. 2017.

[152] Julian Georg and Scott Watson. A Preferred Mass Range for Primordial Black Hole Formation and Black Holes as Dark Matter Revisited. 2017.

[153] Bernard Carr, Tommi Tenkanen, and Ville Vaskonen. Primordial black holes from inflaton and spectator field perturbations in a matter-dominated era. 2017.

[154] Valerie Domcke, Francesco Muia, Mauro Pieroni, and Lukas T. Witkowski. PBH dark matter from axion inflation. 2017.

[155] Simeon Bird et al. Did LIGO detect dark matter? *Phys. Rev. Lett.*, 116(20):201301, 2016.

[156] Sebastien Clesse and Juan García-Bellido. The clustering of massive Primordial Black Holes as Dark Matter: measuring their mass distribution with Advanced LIGO. *Phys. Dark Univ.*, 15:142–147, 2017.

[157] Misao Sasaki, Teruaki Suyama, Takahiro Tanaka, and Shuichiro Yokoyama. Primordial Black Hole Scenario for the Gravitational-Wave Event GW150914. *Phys. Rev. Lett.*, 117(6):061101, 2016.

[158] Eric Cotner and Alexander Kusenko. Primordial black holes from supersymmetry in the early universe. *Phys. Rev. Lett.*, 119(3):031103, 2017.

[159] T. S. Bunch and P. C. W. Davies. Quantum Field Theory in de Sitter Space: Renormalization by Point Splitting. *Proc. Roy. Soc. Lond.*, A360:117–134, 1978.

[160] Andrei D. Linde. Scalar Field Fluctuations in Expanding Universe and the New Inflationary Universe Scenario. *Phys. Lett.*, B116:335–339, 1982.

[161] Ian Affleck and Michael Dine. A New Mechanism for Baryogenesis. *Nucl. Phys.*, B249:361–380, 1985.

[162] Alexei A. Starobinsky and Junichi Yokoyama. Equilibrium state of a selfinteracting scalar field in the De Sitter background. *Phys. Rev.*, D50:6357–6368, 1994.

[163] Alexander Kusenko. Small Q balls. *Phys. Lett.*, B404:285, 1997.

[164] S. Kasuya and M. Kawasaki. Q Ball formation in the gravity mediated SUSY breaking scenario. *Phys. Rev.*, D62:023512, 2000.

[165] Tuomas Multamaki and Iiro Vilja. Simulations of Q ball formation. *Phys. Lett.*, B535:170–176, 2002.

[166] Andrew G. Cohen, Sidney R. Coleman, Howard Georgi, and Aneesh Manohar. The Evaporation of Q Balls. *Nucl. Phys.*, B272:301–321, 1986.

[167] Masahiro Kawasaki and Masaki Yamada. q-ball decay rates into gravitinos and quarks. *Phys. Rev. D*, 87:023517, Jan 2013.

[168] Kari Enqvist and John McDonald. MSSM dark matter constraints and decaying B balls. *Phys. Lett.*, B440:59–65, 1998.

[169] A. G. Polnarev and M. Yu. Khlopov. COSMOLOGY, PRIMORDIAL BLACK HOLES, AND SUPERMASSIVE PARTICLES. *Sov. Phys. Usp.*, 28:213–232, 1985. [Usp. Fiz. Nauk145,369(1985)].

[170] Julian Georg, Gizem Şengör, and Scott Watson. Nonthermal WIMPs and primordial black holes. *Phys. Rev.*, D93(12):123523, 2016.

[171] Robert J. Scherrer and Michael S. Turner. Decaying Particles Do Not Heat Up the Universe. *Phys. Rev.*, D31:681, 1985.

[172] C. Johnson, D. Malyshev, S. Funk, S. Ritz, and Fermi LAT Collaboration. Fermi LAT Limits on Primordial Black Hole Evaporation. In *APS April Meeting Abstracts*, January 2017.

[173] B. J. Carr, Kazunori Kohri, Yuuiti Sendouda, and Jun'ichi Yokoyama. Constraints on primordial black holes from the galactic gamma-ray background. *Phys. Rev. D*, 94:044029, Aug 2016.

[174] A. Barnacka, J. F. Glicenstein, and R. Moderski. New constraints on primordial black holes abundance from femtolensing of gamma-ray bursts. *Phys. Rev.*, D86:043001, 2012.

[175] Peter W. Graham, Surjeet Rajendran, and Jaime Varela. Dark matter triggers of supernovae. *Phys. Rev. D*, 92:063007, Sep 2015.

[176] Kim Griest, Agnieszka M. Cieplak, and Matthew J. Lehner. New Limits on Primordial Black Hole Dark Matter from an Analysis of Kepler Source Microlensing Data. *Phys. Rev. Lett.*, 111(18):181302, 2013.

[177] Kim Griest, Agnieszka M. Cieplak, and Matthew J. Lehner. Experimental Limits on Primordial Black Hole Dark Matter from the First 2 yr of Kepler Data. *Astrophys. J.*, 786(2):158, 2014.

[178] P. Tisserand et al. Limits on the Macho Content of the Galactic Halo from the EROS-2 Survey of the Magellanic Clouds. *Astron. Astrophys.*, 469:387–404, 2007.

[179] Hiroyuki Tashiro and Naoshi Sugiyama. Constraints on primordial black holes by distortions of the cosmic microwave background. *Phys. Rev. D*, 78:023004, Jul 2008.

[180] Massimo Ricotti, Jeremiah P. Ostriker, and Katherine J. Mack. Effect of Primordial Black Holes on the Cosmic Microwave Background and Cosmological Parameter Estimates. *Astrophys. J.*, 680:829, 2008.

[181] Yoshiyuki Inoue and Alexander Kusenko. New X-ray bound on density of primordial black holes. *JCAP*, 1710(10):034, 2017.

[182] B. J. Carr, Kazunori Kohri, Yuuiti Sendouda, and Jun'ichi Yokoyama. New cosmological constraints on primordial black holes. *Phys. Rev.*, D81:104019, 2010.

[183] Florian Kuehnel and Katherine Freese. Constraints on Primordial Black Holes with Extended Mass Functions. 2017.

[184] Norihito Matsunaga and Kazuhiro Yamamoto. The finite source size effect and the wave optics in gravitational lensing. *JCAP*, 0601:023, 2006.

[185] Ryuichi Takahashi and Takashi Nakamura. Wave effects in gravitational lensing of gravitational waves from chirping binaries. *Astrophys. J.*, 595:1039–1051, 2003.

[186] B. P. Abbott. Observation of gravitational waves from a binary black hole merger. *Phys. Rev. Lett.*, 116:061102, Feb 2016.

[187] T W B Kibble. Topology of cosmic domains and strings. *Journal of Physics A: Mathematical and General*, 9(8):1387, 1976.

[188] Tammay Vachaspati and Alexander Vilenkin. Formation and evolution of cosmic strings. *Phys. Rev. D*, 30:2036–2045, Nov 1984.

[189] Neil Turok. The production of string loops in an expanding universe. *Physics Letters B*, 123(6):387 – 390, 1983.

[190] David P. Bennett. Evolution of cosmic strings. *Phys. Rev. D*, 33:872–888, Feb 1986.

[191] T.W.B. Kibble and Neil Turok. Self-intersection of cosmic strings. *Physics Letters B*, 116(2):141 – 143, 1982.

[192] Masaaki Fujii, K Hamaguchi, and T. Yanagida. Affleck-dine baryogenesis and leptogenesis with a gauged $U(1)_{B-L}$. *Phys. Rev. D*, 64:123526, Nov 2001.

[193] Tomohiro Nakama, Joseph Silk, and Marc Kamionkowski. Stochastic gravitational waves associated with the formation of primordial black holes. *Phys. Rev. D*, 95:043511, Feb 2017.

[194] Juan García-Bellido. Massive Primordial Black Holes as Dark Matter and their detection with Gravitational Waves. In *11th International LISA Symposium Zurich, Switzerland, September 5-9, 2016*, 2017.

[195] E Bettwieser and W Glatzel. On the growth of primordial black holes. *Astron. Astrophys.*, 94:306–312, 1981.

[196] P. S. Custodio and J. E. Horvath. Evolution of a primordial black hole population. *Phys. Rev.*, D58:023504, 1998.

[197] Eric Cotner, Alexander Kusenko, and Volodymyr Takhistov. Primordial Black Holes from Inflaton Fragmentation into Oscillons. 2018.

[198] Juan Garcia-Bellido, Marco Peloso, and Caner Unal. Gravitational Wave signatures of inflationary models from Primordial Black Hole Dark Matter. *JCAP*, 1709(09):013, 2017.

[199] Keisuke Inomata, Masahiro Kawasaki, Kyohei Mukaida, and Tsutomu T. Yanagida. Double Inflation as a single origin of PBHs for all dark matter and LIGO. 2017.

[200] Bence Kocsis, Teruaki Suyama, Takahiro Tanaka, and Shuichiro Yokoyama. Hidden universality in the merger rate distribution in the primordial black hole scenario. 2017.

[201] Kenta Ando, Keisuke Inomata, Masahiro Kawasaki, Kyohei Mukaida, and Tsutomu T. Yanagida. Primordial Black Holes for the LIGO Events in the Axion-like Curvaton Model. 2017.

[202] B. P. Abbott et al. Observation of Gravitational Waves from a Binary Black Hole Merger. *Phys. Rev. Lett.*, 116(6):061102, 2016.

[203] B. P. Abbott et al. GW151226: Observation of Gravitational Waves from a 22-Solar-Mass Binary Black Hole Coalescence. *Phys. Rev. Lett.*, 116(24):241103, 2016.

[204] Benjamin P. Abbott et al. GW170104: Observation of a 50-Solar-Mass Binary Black Hole Coalescence at Redshift 0.2. *Phys. Rev. Lett.*, 118(22):221101, 2017.

[205] Takashi Nakamura, Misao Sasaki, Takahiro Tanaka, and Kip S. Thorne. Gravitational waves from coalescing black hole MACHO binaries. *Astrophys. J.*, 487:L139–L142, 1997.

[206] Sebastien Clesse and Juan Garcia-Bellido. Massive Primordial Black Holes from Hybrid Inflation as Dark Matter and the seeds of Galaxies. *Phys. Rev.*, D92(2):023524, 2015.

[207] Martti Raidal, Ville Vaskonen, and Hardi Veermae. Gravitational Waves from Primordial Black Hole Mergers. 2017.

[208] Yu. N. Eroshenko. Formation of PBHs binaries and gravitational waves from their merge. 2016.

[209] Sebastien Clesse and Juan Garcia-Bellido. Detecting the gravitational wave background from primordial black hole dark matter. 2016.

[210] Volodymyr Takhistov. Transmuted Gravity Wave Signals from Primordial Black Holes. 2017.

[211] Rachel Bean and Joao Magueijo. Could supermassive black holes be quintessential primordial black holes? *Phys. Rev.*, D66:063505, 2002.

[212] I. L. Bogolyubsky and V. G. Makhankov. On the Pulsed Soliton Lifetime in Two Classical Relativistic Theory Models. *JETP Lett.*, 24:12, 1976.

[213] Marcelo Gleiser. Pseudostable bubbles. *Phys. Rev.*, D49:2978–2981, 1994.

[214] Edmund J. Copeland, M. Gleiser, and H. R. Muller. Oscillons: Resonant configurations during bubble collapse. *Phys. Rev.*, D52:1920–1933, 1995.

[215] Gyula Fodor, Peter Forgacs, Philippe Grandclement, and Istvan Racz. Oscillons and Quasi-breathers in the phi**4 Klein-Gordon model. *Phys. Rev.*, D74:124003, 2006.

[216] S. Kasuya, M. Kawasaki, and Fuminobu Takahashi. I-balls. *Phys. Lett.*, B559:99–106, 2003.

[217] Ethan P. Honda and Matthew W. Choptuik. Fine structure of oscillons in the spherically symmetric phi**4 Klein-Gordon model. *Phys. Rev.*, D65:084037, 2002.

[218] Mustafa A. Amin, Richard Easther, Hal Finkel, Raphael Flauger, and Mark P. Hertzberg. Oscillons After Inflation. *Phys. Rev. Lett.*, 108:241302, 2012.

[219] Stefan Antusch, Francesco Cefala, Sven Krippendorf, Francesco Muia, Stefano Orani, and Fernando Quevedo. Oscillons from String Moduli. 2017.

[220] Masahiro Kawasaki, Fuminobu Takahashi, and Naoyuki Takeda. Adiabatic Invariance of Oscillons/I-balls. *Phys. Rev.*, D92(10):105024, 2015.

[221] Stefan Antusch, Francesco Cefala, and Stefano Orani. Gravitational waves from oscillons after inflation. *Phys. Rev. Lett.*, 118(1):011303, 2017.

[222] Kaloian D. Lozanov and Mustafa A. Amin. End of inflation, oscillons, and matter-antimatter asymmetry. *Phys. Rev.*, D90(8):083528, 2014.

[223] Mustafa A. Amin. Inflaton fragmentation: Emergence of pseudo-stable inflaton lumps (oscillons) after inflation. 2010.

[224] Mustafa A. Amin, Richard Easther, and Hal Finkel. Inflaton Fragmentation and Oscillon Formation in Three Dimensions. *JCAP*, 1012:001, 2010.

[225] Mustafa A. Amin and David Shirokoff. Flat-top oscillons in an expanding universe. *Phys. Rev.*, D81:085045, 2010.

[226] Liam McAllister, Eva Silverstein, and Alexander Westphal. Gravity Waves and Linear Inflation from Axion Monodromy. *Phys. Rev.*, D82:046003, 2010.

[227] Eva Silverstein and Alexander Westphal. Monodromy in the CMB: Gravity Waves and String Inflation. *Phys. Rev.*, D78:106003, 2008.

[228] Peter W. Graham, Surjeet Rajendran, and Jaime Varela. Dark Matter Triggers of Supernovae. *Phys. Rev.*, D92(6):063007, 2015.

[229] Bernard J. Carr. The Primordial black hole mass spectrum. *Astrophys. J.*, 201:1–19, 1975.

[230] Y. B. Zel'dovich. Gravitational instability: An approximate theory for large density perturbations. *Astron. Astrophys.*, 5:84–89, March 1970.

[231] A. G. Doroshkevich. The space structure of perturbations and the origin of rotation of galaxies in the theory of fluctuation. *Astrofizika*, 6:581–600, 1970.

[232] K. S. Thorne. NONSPHERICAL GRAVITATIONAL COLLAPSE: A SHORT REVIEW. 1972.

[233] Tomohiro Harada, Chul-Moon Yoo, Kazunori Kohri, Ken-ichi Nakao, and Sanjay Jhingan. Primordial black hole formation in the matter-dominated phase of the Universe. *Astrophys. J.*, 833(1):61, 2016.

[234] Tomohiro Harada, Chul-Moon Yoo, Kazunori Kohri, and Ken-Ichi Nakao. Spins of primordial black holes formed in the matter-dominated phase of the Universe. *Phys. Rev.*, D96(8):083517, 2017.

[235] P. F. de Salas, M. Lattanzi, G. Mangano, G. Miele, S. Pastor, and O. Pisanti. Bounds on very low reheating scenarios after Planck. *Phys. Rev.*, D92(12):123534, 2015.

[236] Carlos E. Yaguna. Sterile neutrino production in models with low reheating temperatures. *JHEP*, 06:002, 2007.

[237] Graciela Gelmini, Efunwande Osoba, Sergio Palomares-Ruiz, and Silvia Pascoli. MeV sterile neutrinos in low reheating temperature cosmological scenarios. *JCAP*, 0810:029, 2008.

[238] Mark P. Hertzberg. Quantum Radiation of Oscillons. *Phys. Rev.*, D82:045022, 2010.

[239] J. Jaeckel, P. C. Malta, and J. Redondo. Decay photons from the ALP burst of type-II supernovae. 2017.

[240] C. Patrignani et al. Review of Particle Physics. *Chin. Phys.*, C40(10):100001, 2016.

[241] Tommi Tenkanen and Ville Vaskonen. Reheating the Standard Model from a hidden sector. *Phys. Rev.*, D94(8):083516, 2016.

[242] Peter Adshead, Yanou Cui, and Jessie Shelton. Chilly Dark Sectors and Asymmetric Reheating. *JHEP*, 06:016, 2016.